EXPERIMENTAL MODELLING OF VASCULAR HAEMODYNAMICS

Matthew W Dalton

A report submitted in partial fulfilment of the requirements of the Nottingham Trent University for the Degree of Doctor of Philosophy.

This research programme was carried out in the
Division of Mechanical and Manufacturing Engineering,
School of Engineering,
Faculty of Computing and Technology,
The Nottingham Trent University,
Burton Street, Nottingham. NG1 4BU, UK.

December 2002

CONTENTS

ABSTRACT

Cardiovascular disease is known to be one of the greatest causes of natural mortality in Western society. At this time there is a worldwide drive to reduce the effect of heart disease upon the population and its impact upon health centers and resources.
A common and lethal form of heart disease is manifest in the human body through a weakening and subsequent bulging of arterial vessels. This is known as an aneurysm. Often found, but more so in the older/male demographic, abdominal aortic aneurysms are known to develop and rupture due to material failure in the integrity of the vessel wall due to excessive load applied by mechanical forces. Development of aneurysms as been linked to factors such as smoking, poor diet and hypertension.
However, physical haemodynamic forces acting upon the vessel wall also have an integral part to play in the further growth and eventual rupture of these afflicted vessels. Specifically wall shear forces and areas of stagnation and low fluid shear have been linked to the growth of atherosclerotic lesions and atheroma. Through scientific study of the physical forces involved and the flow regimes observed in aneurysms[1] understanding of these mechanical forces is gained.

Haemodynamic study into aneurysms is conducted through clinical, numerical and experimental work. Due to the delicate nature of aneurysms and that of the human body clinical studies are limited in live patients. Numerical studies are commonplace and gain much knowledge of the fluid flow involved. However, research carried out through computational means requires validation to ensure confidence in the findings. As such experimental work has a part to play in these investigations, most especially in with regard to three-dimensional flows and those exhibiting turbulence. It is the pursuit of any *in vitro* haemodynamic research to construct increasingly more complex and physiologically appropriate models in which to study these forces. As yet, torsion in the aortic flow has been neglected with regard to its distal effects.

A haemodynamic flow rig has been designed to carry out studies into abdominal aortic aneurysms. Both steady and pulsatile flow regimes were implemented and inlet torsion induced by the presence of the aortic arch was studied. Detailed flow measurements were taken using laser Doppler velocimetry techniques to study the effect of torsion upon the flow field through a grid-based analysis. Also near wall measurements were taken in the distal sector of the aneurysm to measure wall shear stress gradients experienced by the aneurysm. Comparisons were made between the flow regimes and forces measured in order to assess the requirement of including torsional inlet parameters in further experimental and numerical studies of aneurysmal geometries in the aorta.

It was concluded from data analysis that inlet torsion is maintained in this model of aneurysmal flow. Steady flows are particularly prone to expressing torsion and as such distal flows and forces are greatly affected. In pulsatile flows the distal hill field flow remained almost symmetrical as the effects of torsion were diminished. However, broadening of the core velocity jet was seen which altered regions of recirculation and implied jet impingement. Furthermore, wall shear stress gradients were particularly susceptible to variations in inlet boundary conditions and patterns of bias were seen in their distribution. As such torsion should not be discounted in any detail flow analysis of the abdominal aortic aneurysms at high flow rates.

ACKNOWLEDGEMENTS

Firstly I would like to thank and acknowledge the efforts and expertise of my Director of Studies, Dr. Shirley Ashforth-Frost as well as others of my supervisory team: Prof. Richard Gentle and Dr. Rob Goodson, both of whom have lent their experience to me in matters of haemodynamics modelling.

I would also like to mention the technicians within the department without whom experimental work would constantly stumble. In no particular order, Mr Rob Potter, Miss Judith Kipling, Mr Ralph James, Mr Kerry Truman, Mr Alan Chambers, Mr Mike Haber, Mr Jez Keeling, Mr John Grimes, Dr Phil Breedon, Mr Gary Griffiths, Mr John Grimes, Mr Alan Tye, Mr Tim Randell and Mr Chris Fox.

I would also like to thank my colleagues Dr Uwe Rudel and Dr Brian Cheung with whom I have shared laboratory space, equipment and many discussions about our work as they interlinked in one way or another.

I would also like to thank my friends, too numerous to mention here, for their support, encouragement and sometimes just simply for listening and nodding occasionally when I talk about my work or my problems.

Last but by no means least I would like to thank my family. My sister, Carol, for her support, kind words and badgering when things were slow and finally my parents, Bill and Lesley, without whom non of this would be possible. Their continued encouragement, unwavering faith and boundless financial support have made my being able to complete this PhD possible.

NOMENCLATURE

Mathematical symbols

Symbol	*Description*	*Units*
υ	Viscosity	m^2s^{-1}
ω	Angular frequency	$rads.s^{-1}$
ν	Kinematic viscosity	m^2s^{-1}
ρ	Density	kgm^{-3}
α	Womersley parameter	-
λ	Wavelength	m
μ	Kinematic viscosity	Nms^{-2}
d	Diameter of the inlet	mm
D	Diameter of the aneurysmal bulge	mm
f	Frequency	ms^{-1}
L	Length of the aneurysmal bulge	mm
n	Refractive index	-
Q	Mass flow rate	m^3s^{-1}
r	Radius of the vessel	mm
Re	Reynolds number	-
U	Mean flow rate	

Acronyms

AAA	-	Abdominal aortic aneurysm
LDA/V	-	Laser Doppler anemometry/velocimetry
MRI	-	Magnetic resonance imaging
U/S	-	Ultrasound
PIV	-	Particle image velocimetry
CCD	-	Charge coupled device (camera)
PMT	-	Photo multiplier tube
BSA	-	Burst spectrum analyser
WSR(s)	-	Wall shear stress gradient (pl.)

General Derivations

Angular frequency	$\omega = 2.\pi.f$
Womersley Parameter	$\alpha = r\sqrt{\frac{\omega}{\nu}}$
Reynolds number	$\mathrm{Re} = \frac{d.U}{\nu}$
Dynamic viscosity	$\nu = \frac{\mu}{\rho}$

LIST OF FIGURES

LIST OF TABLES

INTRODUCTION

1.1 Vascular Haemodynamics in the world today

The field of vascular haemodynamics is both varied and broad covering myriad aspects of physical fluid flows and every major region of the vascular system in the human body. These include blood flows in the cranium, thorax, abdomen and in extremities such as the legs.

Vascular disease is extensively studied worldwide in its many forms because it is the leading cause of natural illness and mortality in the western world. Even above medical conditions such as cancer, vascular disorders are accountable for nearly half of all deaths in the U.S for adults over 25 years.

In the UK coronary heart disease, stroke and other circulatory diseases are responsible for 200,000 of the half a million deaths that occur in the UK each year (Government White Paper, 1999). This equates to one third of all deaths in men and one fifth of all deaths in women of those less than 65 years of age. In males over 65 years of age vascular related disorders are the leading cause of mortality in the UK. Consequently the costs of related health care and treatment are a major drain on the budgets of health-centres. The non-terminal consequences of vascular disease are also responsible for a large number of working days lost in industry every year and for also forcing lifestyle restrictions upon many sufferers.

There are distinct differences in susceptibility to vascular disease between different demographic groups. These variations are attributed, amongst others, to gender, age, ethnicity and social class. For example men in lower social groups are more prone to heart disease than the average for the whole population. Men are also more likely to suffer from vascular disease than women and the probability of this occurring increases for older age groups until heart disease is considered the primary cause of death in males over 65. Due to these alarming statistics there is a worldwide drive to decrease the prevalence of heart disease, both its causes and its effects upon the population. In the UK this has been quantified as a declared intention by the government to reduce the death rate from vascular related disease in under 75's by two-fifths by 2010. At present coronary heart disease and related illnesses account for more than 40% of the half a million deaths occurring in the UK each year (Government White Paper, 1999).

Through the study of vascular disorder and illness, understanding of these conditions can be increased and hence their prevention and successful treatment can be made more commonplace.

1.2 Abdominal Aortic Aneurysms

Aneurysms are one such example of vascular disease and are a significant cause of illness and mortality. They are manifest in the body through a ballooning of the vascular wall. This is likely to cause pressure changes within the local flow system and stresses upon the constituents of the blood itself. Furthermore the flow conditions nurtured by the aneurysm are likely to be active in its pathogenesis. Left untreated, aneurysms are prone to rupture.

Lanne et al (1998) described an aneurysm as a permanent localised dilatation of an artery exceeding 50% of the expected normal. Abdominal aortic aneurysms (AAA) are a specific example of this disease. In the human descending aorta, which has an expected diameter of 16-20 mm, aneurysms of less than 40mm diameter are considered not dangerous, whereas aneurysms exceeding 50mm in diameter are most likely considered for clinical intervention.

Aneurysmal growth is a progressive disease that is most commonly associated with atherosclerosis in medium to large arteries. From a screening carried out of aneurysmal cases, Grimshaw (1994) estimated that 95% of aneurysms are of atherosclerotic origin and are most commonly of the fusiform type (Figure 1-1).

Initially aneurysmal disease is characterised by the deposition of lipids upon the arterial wall, know as ‘fatty streaks’. The innermost layer of the arterial wall (the intima) then undergoes a thickening known as intimal hyperplasia. Subsequently atherosclerotic plaques (or atheroma) form on the vessel wall as lesions composed of fibrous material shrouding a core of necrotic tissue. This atheroma can both obstruct normal blood flow and weaken the arterial wall leading to local dilation of the lumen that further contributes to the adverse haemodynamic conditions in the artery. Blood coagulation and thrombosis can also occur. The partial breakdown of large atherosclerotic plaques or the shearing off of small sections of a thrombus can lead to large particles or embolisms flowing downstream into smaller peripheral arterioles or capillaries, possibly causing a reduction of bloody supply to tissues or organs. In cardiac tissue this leads to angina and myocardial infarction as the cardiac muscle is deprived of oxygen and quickly assumes anaerobic respiration causing acute pain and eventual failure of the muscle tissue. When deprived of circulation, an organ or tissue will suffer from a lack of oxygen and nutrients. Also the recirculation of metabolic waste products away from the location will potentially cause poisoning or even necrosis of the local tissue.

There are predominantly three types of aneurysm (illustrated in Figure 1.1): the fusiform, saccular and dissecting types. Off these, the fusiform is by far the most commonly seen in the abdominal aorta.

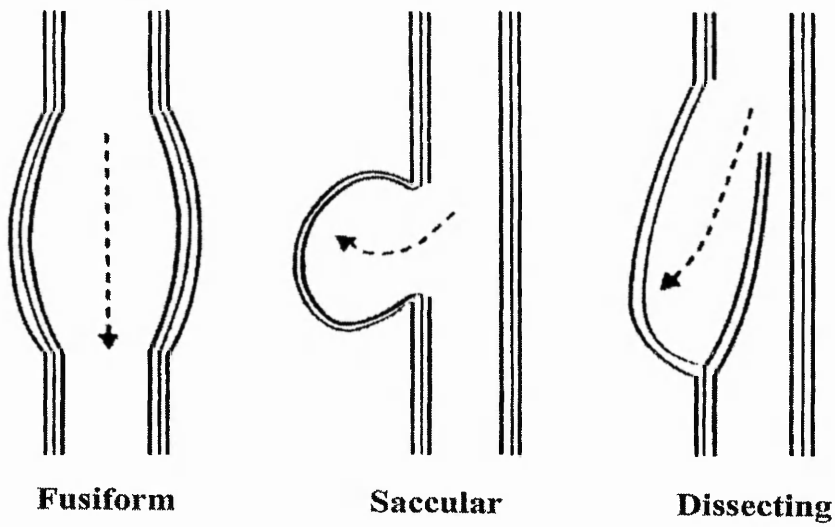

Figure 1-1 Diagram illustrating various types of aneurysm (Goodson, 2001)

The specific causes and genesis of aneurysms are not yet known. However, they are linked to a multitude of environmental variables, congenital factors and age. Chemical factors such as diet and smoking are greatly linked to heart disease.

In engineering terms an aneurysm is linked to physiological changes in the elastic nature of the vascular wall. It can be described as a classic case of material failure and excessive load applied to a material of inadequate strength (MacSweeney et al, 1994). This leads to the growth and eventual rupture of an aneurysm. Aneurysmal growth is non-reversible and catastrophic failure of the wall is inevitable after extended periods of time (Goodson 2001). However, the exact circumstances leading to aneurysmal rupture are impossible to predict at this time.

Where rupture occurs, the survival rate is extremely poor and the consequences are often fatal due to internal haemorrhaging. Mortality rates in such instances are above 90%. AAA's manifest themselves as a developing dilatation of the main artery of the vascular system in the abdomen distal to the aortic-iliac bifurcation located a little above the waistline. The physical causes of AAA's are many and diverse but are linked closely with arterial wall damage and atherosclerotic plaque development. Both these factors have been linked to the physical action of the flow and stresses upon the arterial wall, which can be investigated using engineering methodologies.

The growth of atherosclerotic plaque and lesions has been linked to shear stresses upon the interior of the arterial wall. This has been attributed to a detrimental effect upon the endothelial layer of cells that actively protect the vessel. Oscillating and low shear stresses have been known to break down communication between these cells and hence reduce their ability to prevent these plaques from developing. Due to these oscillating shear stresses the cells have been demonstrated to migrate from close mutual proximity, which has been associated with their decreased ability to actively prevent atherogenesis (Davies, P.F. (1998), Phelps, J.E. (2000), Knight, J. (1999)).

1.3 Engineering in Haemodynamics

The first scientist to apply the logic and mathematics of fluid dynamics to the human body was Young at the turn of the 19th Century. He theorised that the body could be simplified and considered as a network of tubes through which a viscous fluid is pumped. Previous considerations of the human body's vascular system were, for the majority, baffling. Even though there are many variables to be taken into consideration, compromises can be made in the detail of the vascular model considered, enough to make a working model from which practical knowledge of the flow system can be gained. Examples of variables simplified in an aortic flow model could be:

- the tapering of the lumen
- the elasticity of the vascular wall
- the pulsatility of the flow
- the non-Newtonian viscosity exhibited in the blood
- the unique variability of each geometry *in vivo*
- blood/wall chemical interactions

Utilising such compromises and generalisations it has been possible to study the infinite variety encountered within the human demographic and arrive at conclusions worthy of clinical relevance.

These studies are of importance as at present there are few viable treatments. It is speculated that the prevention of aneurysmal development is possible by long-term lifestyle changes in diet, exercise and health related habits (e.g. smoking, excessive alcohol consumption). The only cure practised at this time is major surgical intervention, excising the aneurysm. The damaged vessel is replaced with a tissue graft. This is either an artificial vessel or vascular tissue transplanted from elsewhere in the body. This however, produces two minor occlusions in the suturing process; restrictions in the aortic lumen that are prone to growth and eventual detriment to the local vascular system. These problems related to end-to-end anastomoses include a pressure drop that would increase the resistant load upon the heart and cause jet formation, leading to fluid shear within the bulk flow. This could cause stresses to erythrocytes with the possibility of haemolysis, which has obvious implications for the patient.

Alternative surgical treatments are limited due to the proximity of the abdominal aorta to the delicate neural tissue of the spinal column and its related blood vessels.

Endovascular procedures are presently being investigated and the deployment of different types of stent are possible in the human body. A stent is an internally deployed tubular prosthesis that is locked in place within the human vascular system. Mimicking the shape of the vessel in which it is situated it is able to provide a modicum of repair and longevity to a diseased and distended artery. The additional advantage of such devices is that they can be employed in so called 'key-hole' endovascular surgery reducing the cost and time involved in during invasive procedures. Furthermore the risk of mortality during such an operation is massively reduced.

The long-term effects of these are still being clinically investigated as artificial materials present within the lumen of the artery are subject to physical and chemical ordeals. Three basic deployments are possible. One is a linear cylindrical stent that bridges the bulge of the AAA, protecting the wall from destructive stresses. Others include a bifurcating stent that sits in one of two positions. Bifurcating from a single inlet through the bulk of the aneurysm the first of these divides the aortic flow prematurely, or a similar bifurcating stent that divides flush against the iliac bifurcatio; recreating the original geometry of the abdominal aorta.

Using engineering methodologies and appropriate study it is possible to increase the understanding of the mechanics and pathogenesis of vascular disease in humans, the results of which can be used to better inform clinicians as to the cause and development of the disease. Furthermore the outcome of surgical interventions can be studied and the most beneficial geometry or materials can be used in invasive surgery. This increases the long-term lifespan of the patient whilst similarly decreasing the cost of post-operative care.

Parallel fields of research relating to AAA's are conducted using computational methodologies. These analyse the predicted outcomes of pressure and fluid flow upon a virtual construct of the geometry. The fluid flow equations are applied to a mesh and calculations carried out upon each element. As computers become more powerful and the software more complex more detailed analysis can be carried out.

However, the limitations of these techniques are all too apparent. Each generation of computational fluid dynamics (CFD) introduces more complex attributes to the system. Preliminary research into AAA's was considered using steady flow parameters and simple models. Now more complex geometries and flow conditions are being considered and the detail of each consecutive study increases. However, confidence in these numerically derived results is not absolute and experimental validation is actively sought.

Recent studies have taking into account the swirl associated with aortic arch haemodynamics. However, to this author's knowledge, although torsion has been demonstrated in the thoracic and descending aorta by numerical, experimental and clinical means, there is a paucity of work carried out to qualify the effects of this torsion in the abdominal aorta.

Aims and Objectives

1.3.1 General Aims

a) To provide new experimental data for velocity, distal wall shear rate and flow regions in abdominal aortic aneurysms and the effects of upstream torsion upon these factors

b) To seek a better understanding of aneurysmal fluid dynamics and the changes occurring in the flow regimes in an aneurysmal model due to upstream torsion brought upon by the three-dimensionality of the aortic arch

c) To provide novel and timely data to aid in the validation of numerical investigations into abdominal aortic aneurysms, specifically with regards to turbulent flow and torsional inlet boundary conditions

1.3.2 Specific Objectives

The research was guided by the pursuit of the following objectives:

1) To compile a review of relevant literature pertaining to the study of haemodynamics specifically:

   - Experimental methodologies used in the model studies of haemodynamics
   - The variety of analogous fluids used in the mimicking of vascular flow conditions with regard to density, dynamic viscosity, refractive index and
   - The flow conditions studied to simulate abdominal haemodynamics: velocities, Reynolds numbers, Womersley parameters and Newtonian behaviour.
   - The use of inlet boundary conditions employed in both experimental and numerical studies of abdominal aortic flow.

- To catalogue the data obtained in the study of both steady and pulsatile flow through abdominal aortic aneurysms

2) To commission a flow apparatus to provide reliable steady flow conditions
3) To commission a second pump to provide a repeatable pulsatile waveform analogous to those found *in vivo* simulating moderate exercise conditions
4) To design and create a model geometry that provides a stylised representation of an abdominal aortic aneurysm in which flow fluid properties can be measured. The model must be designed with the following criteria in mind:
    - To provide optical access throughout the entirety of the model suitable for full field flow visualisation and laser Doppler velocimetry
    - To possess a plane face so as to facilitate the use of optical techniques and reduce complications due to refraction
5) To design and mix an experimental fluid possessing properties analogous to that of whole blow. Following criteria were sought:
    - To possess physical properties of viscosity and density comparable to those of whole blood
    - To possess optical properties to facilitate the use of experimental procedures employed in this investigation, specifically their fluid was:
        - *Colourless*
        - *Transparent*
        - *Refractively matched to the material used in the casting of the aneurysmal geometry*
    - To be experimentally viable in its shelf-life, possess no corrosive properties and be of low toxicity

6) To perform laser Doppler velocimetry measurements in the flow throughout defined planes in order to visualise the flow regimes and recirculation in the flow field through three dimensions
7) To carry out near wall velocity measurements within the fluid boundary layer of the distal region and to measure and assess the distribution of forces acting upon the interior wall of the aneurysm
8) To carry out the above under conditions of both steady and pulsatile flow. The latter specified to six time bins distributed throughout the pertinent phases in the cycle to facilitate understanding of the data
9) To obtain design parameters and create a stylised likeness of the human aortic arch in order to introduce appropriate torsion in to the inlet boundary conditions proximal to the aneurysmal model
10) To include the aortic arch to introduce out of plane torsion in the inlet flow field and to take further measurements detailed in the above points
11) To analyse and compare the data collected in order to represent the changes brought about by upstream torsion and assess both their qualitative and quantitative changes upon the flow field, specifically:
    - The redistribution of the inlet jet and any impingement upon the distal wall
    - The effects upon the core velocity experienced in the geometry
    - The consequences to vortices and areas of recirculation in the flow
    - The effect upon the occurrence and distribution of flow stagnation in the aneurysmal model
    - The quantitative changes and the redistribution of wall shear stresses observed distally in the aneurysm model

12) To present this data so that clinicians may better understand flow dynamics in abdominal aortic aneurysms and appreciate the effects of torsion in comparison to the conventional non-torsional inlet model

13) To provide experimental data so that those carrying out parallel investigations using numerical methods may validate their models employing turbulence and upstream torsion

LITERATURE REVIEW

2.1 Introduction

Cardiovascular diseases, such as stroke and heart disease, are known to be amongst the most common causes of adult death in the western world. Since the nineteen-sixties, it has been ascertained that the haemodynamics of, for instance, a stenosed artery or aneurysm, is a critical factor in the disease's development. Therefore, blood shear stresses and recirculation areas can have serious consequences for the patient's health. Thomas Young carried out the first haemodynamics-related experiments in 1808. He theorised that the physical studies of fluid dynamics, wave propagation and elastic materials could be applied in full to the subject of the human body in order to extend the biological research of the day. These ideas are still applied today by fluid engineers working on biological and related haemodynamic research projects.

Through fluid dynamics research, scientists have been able to advise clinicians upon the most effective use of surgery. Haemodynamic studies have also been used to help understand the consequences and after-effects of specific procedures. For example, in a femoral artery bypass the graft is attached to the recipient vessel by use of a Miller Cuff. This is a piece of excised vascular tissue, looped and made into a collar, to either side of which the two vessels, the bypass and femoral artery, are sutured. The collar changes the conditions of the bypass blood flow in such a way as to increase the potency of a large vortex in the geometry. This has the effect of decreasing platelet deposition and therefore increases the post-operative 'lifetime' of the graft. Research is endeavouring to indicate whether this increased longevity of the bypass is due to the material or the geometry of the Miller Cuff (How et al. 1997). The latter of the two options is more likely. If this is the case, the shape of the cuff can be optimised so that the need for a repeat bypass, due to reatherogenesis, is less likely.

This type of research has also been seen in the work of Kim et al. (1995) where the haemodynamics of the Fontan connection has been studied. During this procedure the right heart of an infant is bypassed in order to overcome postnatal circulatory difficulties. The paper concluded that an improved geometry and thus streamlining within the Fontan connection would decrease the pressure drop and therefore make the connection more energy efficient and put less strain on the cardiac muscle.

In many fields the simulation of haemodynamics has become prevalent over experimental modelling. Techniques such as computational fluid dynamics (CFD) are able to study the flow patterns and shear stresses in a complex geometry by the use of a computer and commercial software. Variables in such a simulation can be changed with relative ease compared with similar changes made in an experimental rig. However, CFD work has its limitations and is commonly, for completeness, validated by experimental data in order to aid credibility. CFD results depend on the choice of governing equations utilised in the study and and accuracy is dependant upon the discretisation level, numerical precision and.choice of boundary conditions. Therefore, in the study of vascular haemodynamics, experimental flow studies are still an important tool.

A recent example of one such work of this type was a combined experimental and numerical examination of the bypass graft in end-to-side anastomoses of the femoral artery and the inclusion of out of plane inlet parameters (Rowe, 1999). Work such as this highlight the value of experimental research to lend credence to computational data that might not otherwise be verifiable, specifically in torsional and out-of-plane inlet flows which until recently, have rarely had the benefit of detailed research in haemodynamics.

Experiments are carried out *in vitro* in most cases. This is due to the inability of many essential methods of observation such as laser Doppler velocimetry (LDV) or flow visualisation to be used in the arterial system. These methods may even preclude the use of organic materials, for example blood or vascular tissue, in such experiments. The exception to this occurs with Doppler ultrasound scanning (U/S) and also magnetic resonance imaging (MRI) that can be used *in vivo*. There is a company however that is developing a material to seed the blood for more accurate U/S scanning (previously known as 'Andaris Group Ltd'). Other methodologies have been applied to *in vivo* experimentation but the application of certain procedures limits their use commonly to non-human subjects. Therefore, it is important to simulate *in vivo* conditions by the use of analogous substitutes when investigating human haemodynamics. The main items to consider with regard to *in vitro* experimentation are *the motion of the fluid, the geometry, the model, the fluid and its motion.*

Often varying one characteristic of a substance may change another characteristic, therefore properties of this nature must be balanced out against each other and compromises made. For example, Baldwin et al. (1993) used a blood analogue fluid that had a density 165% that of the accepted value for human blood. However, the working fluid used was designed to exactly match the refractive index of the Plexiglas used in the manufacture of the rig. This enabled laser Doppler velocimetry (LDV) measurements to be taken with much greater ease and accuracy.

2.2 Methods of Observation

LDV, U/S and various flow-visualisation techniques are all viable methods of velocimetry. The operation of these methods must be considered when designing the experimental rig.

LDV is a proven technique using the Doppler effect of light waves to measure the velocity of particles suspended in the fluid and thus the dynamics of the fluid itself. It does, however, require accurate placement of the measurement area and, therefore, to avoid misalignment of the intersecting laser beams, it is necessary to make a displacement correction due to any refraction. In the use of elastic rigs that have uneven and dynamic wall surfaces it is critical that the refractive indices be matched to minimise this displacement. Ordinarily LDV cannot be used *in vivo* but recent achievements in technology mean that a far-red laser is readily available for commercial use. This low frequency laser beam can penetrate the skin and sub-dermal tissue to a depth of a few millimetres, enough to measure micro vascular blood perfusion or carry out velocimetry measurements of the blood within the knuckle joints (Obied et al, 1990; Biophotonics, 1998). The low penetrating ability on the laser is due to its necessarily low power. The higher powers required to make deeper measurements would undoubtedly damage intervening tissue.

Flow visualisation is a broad category that enables the observer to record the progress of substances in the fluid by means of a charge coupled device (CCD) camera or similar visual recording equipment. The substance could take the form of particles illuminated by a laser light sheet as employed in particle image velocimetry (PIV). There are many types of particle commercially available. Ideal qualities in such particles are a high reflectivity and neutral buoyancy relative to the working fluid. An example of such a particle would be silver-coated, hollow glass spheres in water. Under an adequate length of exposure the illuminated particles can be seen to produce streaks, which upon examination, reveal the path of the particles. Velocity data can also be extracted by the use of suitable computer software and hardware.

Dye velocimetry can produce similar results with the added bonus that the dye particles are sub-micron in size and in a liquid state so as to better follow the working fluid. Photochromic dyes can also be employed in flow visualisation techniques as above but such dyes are truly in solution and therefore are said to match the dynamics of the flow more accurately than either suspended particles or mixed fluids. Opaquely activated by incident ultra-violet light, the photochromic dye streaks can be observed. A method such as this also precludes the need for an invasive injection apparatus in the rig that could possibly affect the flow field.

Ultrasound Doppler techniques are also able to measure the velocity of fluid flow. This technique is versatile in that is can be used either *in* or *ex vivo*. However, it does have its drawbacks. The relatively large width (1-2 mm) of the ultrasound beam makes the sample volume greater than can be achieved with LDV. Normal scanning is achieved by observation of the reflected wave amplitudes. Frequency shift data is used to gain localised and full flow velocity information. This can either be visualised across the full beam width or localised to a point measurement volume for graphical output. Another concern is that the angle between the beam and the flow direction must be known. When used *in vivo* the operator must make a manual angle correction using the machine cursor. This correction assumes that the blood flow vector is parallel to the vessel wall. This is an incorrect assumption in the case of stenoses, aneurysms and other curved geometries. In such stenosed cases the error in measuring the beam-velocity vector angle has been as much as 25° (Hoskins, 1997). This also means that U/S techniques are inadequate at present for measuring turbulent flow. Ultrasound techniques are used in a variety of forms including pulsed Doppler velocimetry (PDV) and acoustic Doppler velocimetry (ADV). The governing principle behind each of these is the same.

New technologies and methods of velocimetry are, as always, of paramount importance. Developments in ultrasound scanning may soon allow clinicians to take multiple component readings *in vivo* with far greater accuracy than is presently possible. Recently conceived three-dimensional particle image velocimetry and flow visualisation techniques will also increase our understanding of the dynamics of blood flow. Kurada et al. (1997)

wrote substantially with regard to a PIV technique for three-dimensional flows. The system utilised a single camera and a tri-splitting lens along with 'photogrammetric imaging' which combined the advantages of stereo and orthogonal views. An algorithm was used to follow the particles from frame to frame. An automated three-dimensional tracking technique for haemodynamic studies was also devised by Tsao et al. (1995). This technique used two cameras and was successful in determining seventy-nine percent of the paths of suspended particles.

With new laser technology it is also possible to bypass the need for blood analogue fluids. A recently developed laser diode[1] has a wavelength of 805nm placing it in the infrared part of the spectrum. To this wavelength, it is claimed, blood is effectively transparent and laser Doppler velocimetry seems feasible. With a suitably designed rig, of correct refractive index, measurements could be taken more accurately quantifying the blood flow dynamics. Presumably the components of the blood would not render such a technique unsuitable due to the use of *in vivo* LDV. The components of the blood would adequately seed the flow. However, if it is so the recirculation zones within a desired geometry could be examined and the thrombus forming nature of blood examined more readily *in vitro*.

[1] Oxford lasers Ltd., Oxfordshire, UK.

2.3 Geometry and model

The shape of the vessel to be observed must be faithfully reproduced or a stylised approximation made with reasoning. Surface roughness, model porosity and scaling are also considered. The model is often made from a rigid plastic, but experiments that are more realistic use a viscoelastic material.

The shape of the model can either be a stylised representation of the geometry to be observed or an accurate replication depending upon the experimental brief. For instance, a tube containing two smooth obstructions can be employed to represent a stenosed situation. This may be adequate for some observations. Otherwise, an exact model of the geometry can be fashioned. To map the geometry of the vessel for CFD simulations tools such as MRI and ultrasound scanning are often used. When a flexible geometry is required for an experimental rig, distorted elastic tubing can be used. This tubing can be modelled into a stenosed or aneurysmal geometry. An accurate model can be made from polyurethane by the dipping of a mould cast from an excised vessel. This process was described in a paper by Hayashi et al. (1996). The required cadaver tissue was perfusion fixed under physiological pressure whilst *in vivo*, and then excised. A process was undertaken by the combined use of different materials to create a replica of the vessel geometry. Made from polyurethane, it had an elastic resistance proportional to its wall thickness. Thus, a model was manufactured that matched the *in situ* vessel in geometry, wall irregularities and elasticity as closely as possible. However, the elasticity of the vascular wall is estimated from experimentation, as it is viscoelastic. The elasticity of cardiovascular tissue is also dependent upon environmental factors such as age, disease, gender, size and other numerous variables. There are, however, other interactive factors. The rate of flow along the vessel, due to the biochemical components of the blood, is known to affect the active wall components. The smooth muscle component, controlled by the autonomic nervous system, is also a factor in determining wall stiffness. Such interactive factors are unpredictable. An approximation of such variables must be taken, as there is no single Young's modulus value for vascular tissue although a value of $12.2*10^5$ Pa has been estimated (Siebes et al., 1996). Greater detail can be found in the referenced literature.

For the use of LDV and other velocimetry techniques there are two major rig designs; those that have a rigid wall and those that account for the wall's elasticity.

Extended from the above ideas, the more basic design may consist solely of an acrylic rig with planar external face and a stylised internal geometry. The planar external face is important in the application of LDV and certain flow visualisation methods, as an uneven surface would refract light passing through the rig in an unnecessarily complicated manner (Figure 2-1). Rigid rigs can be made from a number of materials as long as the material has a very low porosity and facilitates the use of flow visualisation techniques. This could include using acrylic or similar as it is relatively easy to machine and can be highly polished for optical access. However, the cost of machining such materials, where complex geometries are required, can be prohibitive. A silicone elastomer has been used (Chong et al., 1999) to create vascular geometries for flow visualisation experiments. Creation of a wax cast, or low temperature alloy, can allow the creation of solid models with relatively low cost of materials and equipment.

For the experiments mimicking the elastic nature of the vascular wall a more complicated rig must be used (Figure 2-1). The elastic vessel will have to maintain a static primary surface regardless of deformities to the vessel model induced by pressure changes within the rig. This is a surface through which the laser beams can pass at a known angle regardless of deformations within the vessel or the uneven aspect of the interior wall of the vessel. To facilitate this the whole vessel would be suspended in an acrylic unit that would provide the uniform exterior surface. The intermediate spacing would be filled with a viscous fluid, matched, if possible, to replicate the cushioning nature of surrounding tissues found *in vivo*. Approximate position would also be maintained. The acrylic unit, the interstitial fluid, the vessel and the working fluid would all be required to have the same optical properties so that incoming light would not be refracted, displacing the measurement volume.

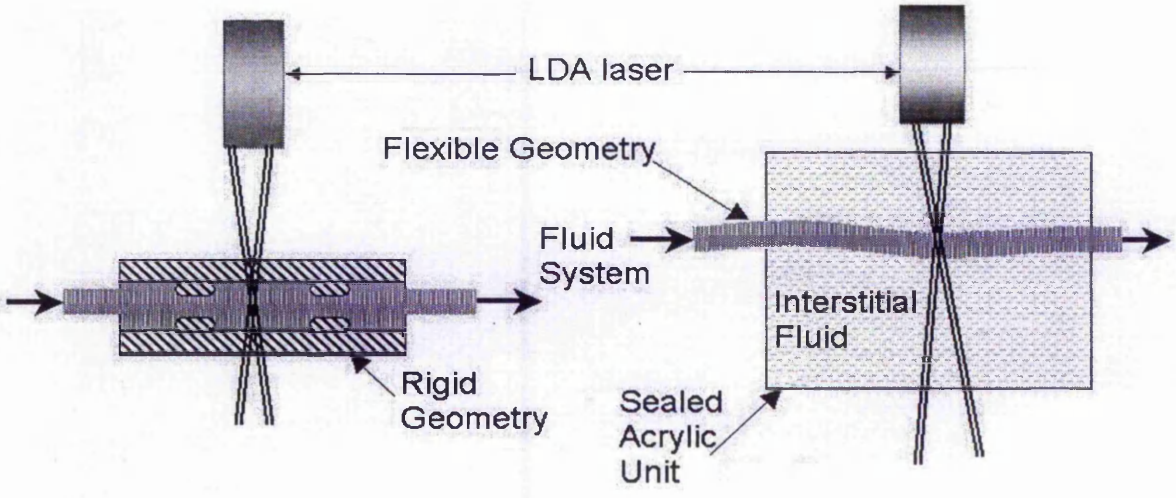

Figure 2-1 diagram showing possible methods of experimental vascular modelling

A simpler option in the modelling of vascular geometries is the employment of a one-piece silicone based elastomer (Asbury et al, 1995 and Rowe, 2000). Such a material can be cast about a manufactured core, which is then removed using the lost-wax process. The model can be cast inside a box of plane outer face to facilitate the use of optical techniques. Such a model can be linked to any flow rig by the use of suitable connectors and is almost unlimited in its variety. Even an aortic arch could be cast including its three-dimensional character and every point of the geometry accessible for LDA study. However, the flexibility of such a model would be in question. Silicone elastomer used in this manner has a modulus of flexibility highly dependent upon the thickness of the model wall. Therefore a complex geometry may well have a varying modulus of elasticity along its length. This would be less important in steady flow experimentation, but in a pulsatile analysis the flexibility of the wall would have to be considered.

The working fluid in the rig is of utmost importance in haemodynamic studies. This is because of the specific fluid properties of blood. Blood is comprised of a water-based solvent called plasma in which suspended particles and dissolved molecules are present. The particles, however, are considered responsible for the non-linear properties of the fluid. The erythrocytes, or red blood cells (RBC's), are hollow biconcave discs, the walls of which are made from a lipid bilayer. They contain the protein haemoglobin that is responsible, in the main, for the mass transport of oxygen around the body. The non-Newtonian nature is attributed to the elastic nature of the plasma membrane from which the erythrocytes are composed. They are suspended in a Newtonian fluid (plasma) and encase the haemoglobin (also Newtonian). A simple mixture of the two fluids would not manifest this non-Newtonian behaviour. This is normally considered to be a major factor in haemodynamics where the shear factors become dominant, for instance in the small capillaries and perhaps in areas of secondary flow. This has been estimated as a shear rate $<100s^{-1}$. In the major arteries the flow is normally considered Newtonian. However, such assumptions can be misleading as discussed in section 2.4.1.

2.4 The blood analogue fluid

There are several factors that must be considered when designing a blood analogue for haemodynamic experiments.

2.4.1 NON-NEWTONIAN/NEWTONIAN NATURE OF BLOOD

As described, human blood is non-Newtonian. However, many experimenters simplify matters by showing that under high shear stress, such as those found in large arteries, the blood may be approximated by considering it Newtonian in nature (Tu et al., 1996 and Back et al., 1992). Perktold et al. (1989) carried out finite element simulations of both Newtonian and non-Newtonian pulsatile blood flows in an aneurysmal geometry. Only minor differences were found in results for the large arteries considered. Such data may, however, be misleading as a more recent publication (Yeleswarapu et al, 1998) disputes this. The peak velocity of porcine blood was measured by PDV and compared against two computer models. The non-Newtonian computer model matched the measured velocities to 1-7% accuracy and the Newtonian predicted velocities were erroneous by an average of 40%. This Newtonian simplification is also seen in CFD simulations considering large arteries. The non-Newtonian nature of blood is considered to be manifest in arterioles and veins which have a smaller diameter and where low shear stresses are dominant (Tu et al., 1996). Hayashi et al. (1997) carried out a series of experiments using both Newtonian and non-Newtonian fluids. Contradictory data also comes from Ishikawa et al (1998) whose numerical research shows that, in stenosed arterial models, non-Newtonian behaviour reduces the intensity of the vortices seen distal to of the occlusion and hence the downstream wall shear stresses. Also influence on the flow was observed at high Stokes and Reynolds numbers when the pulsatile waveform has a stagnant period and low shear stresses are present. It was also claimed that flow characteristics exhibited by non-Newtonian transient flow were more stable, than seen in the simpler, Newtonian model.

Many inorganic fluids used in experimental work consist of a mixture of water, glycerol and sodium thiocyanate (NaSCN) (Table 2-1). To obtain non-Newtonian characteristics in the fluid, Xanthan gum can be added. However, the appropriate nature of this non-Newtonian additive has not been quantified. Alternative chemicals included in the mixing of blood analogue are saturated aqueous sodium iodide (sat. aq. NaI), (Baldwin, 1993) and potassium iodide (KI). The use of blood analogues varies between research projects and a balance is often made between properties and necessary compromise.

2.4.2 VISCOSITY, υ

The haemodynamics of blood are greatly affected by its viscosity. Therefore, experimenters attempt to closely match the kinematic viscosity of their analogue fluid with that of blood. The viscosity of water-based fluids are often increased by the addition of glycerol (Naiki et al., 1995) or dextrin. It has also been shown that the viscosity of blood varies within the body with respect to its location (Liepsch, 1986). Peripheral circulation is subject to counter-current heat exchange along the length of the limb and therefore will be maintained at a lower temperature than core body temperature. However, in the torso (abdominal arterial flow), the temperature will be matched to core body temperature.

2.4.3 DENSITY, ρ

The density, like the above properties, is important in ensuring that the dynamic behaviour of the test fluid matches that of *in vivo* haemodynamics. If the fluid is to be employed in an experiment using flow visualisation or LDV, the seeding particles must be neutrally buoyant so that they are not subject to additional forces, which would deviate them from their natural flow patterns. For this purpose sodium chloride (NaCl) can be added to effectively increase the relative buoyancy of particles within the fluid without greatly affecting other fluid properties. However, some small compromise in the fluid properties may be unavoidable and NaCl is known to have influence upon the refractive index of the liquid in which it is in solution. However, this change is normally no more than a 1% increase.

2.4.4 Optical Properties, (n)

Several optical properties must also be considered in the design of a blood analogue. Firstly the fluid must be colourless and transparent. This is necessary in order to use such techniques as flow visualisation and LDV with the greatest effect. Any absorption of light, at any wavelength, would decrease the experimental value of the fluid. The refractive index of the fluid must also be known for some experimental methods. In order to use LDV techniques the position of the sampling volume, at the intersection of the beams, must be precisely located. As the laser beams pass through the rig material and into the fluid, the position of the sample volume will be refracted. As long as the refractive indices of the materials and the angles of incidence are known, the displacement of the measurement volume can be calculated. By matching the refractive index of the fluid to that of the rig material it is possible to simplify the experimental procedure. In the case of a flexible rig, the whole tubing assembly can be submerged in a fluid. In this case the refractive indices of the fluids (blood analogue and interstitial, Figure 2-1) are matched to that of the rig and it is possible to use LDV techniques. The position of the sample volume will not be refracted by the vessel/fluid interface and therefore will be independent of the angle between incident beams and vessel wall. This also allows for an undulating or uneven internal surface as might be seen in an *in situ* casting or within the region of a modelled stenosis. To increase the refractive index of aqueous based fluids, sodium thiocyanate (NaSCN) can be used (Hayashi et al. 1996, Naiki et al., 1996 and Matsumoto et al., 1994). It is worthy of note here that NaSCN, and one alternative chemical ISCN, are both toxic chemicals. They contain the cyanide ion and are toxic (by respiratory inhibition) through inhalation, dermal absorption and ingestion (NaSCN has a LD50 of 764 mg/kg (orl-rat)). Less toxic alternatives are also available yet less common. Sodium chloride (NaCl) has been used to tailor the refractive index of analogue fluids (Chong et al, 1999) and is relatively non-toxic in the quantities used.

As LDV is a common method of velocimetry there is an additional concern when designing a blood analogue for such experiments. The majority of experimental papers describe the use of glycerol for their working fluid due to its viscous nature. However, glycerol is a carbohydrate that is optically active in this form. This means that light passing through the fluid will under go a 90-degree rotation in the plane of polarisation. Due to the polarised nature of an LDV laser system, this is a problem that requires consideration when implementing and has been known to cause some problems. Examples of fluids used as *in vitro* analogues over recent years are shown in Table 1. The notes on each are included where possible showing fluid properties, and methods by which those properties are manipulated.

Table 2-1 A summary of blood analogues utilised in haemodynamic modelling

Reference:	Components.	Mixture.	Nr.	ρ.	μ.	υ.	Notes.
Liepsch, D. W. (1996)	Glycerol	25%			2 cP		
	H_20	75%					
Cavalcanti, S. et al. (1992)	"Water-glycol ethylenic mixture"			1068 kg/m^3			At 28°C.
Back et al. (1992)	sugar	33%				$3.5*10^{-6}$ m^2/s	Q=180 ml/min, Re_i = 353
	H_20	66%					
Baldwin, J. T. (1993)	Sat. aq. NaI	79%	1.49	1750 kg/m^3	6.6cP	$3.75*10^{-4}$ m^2/s	Used at 25°C. Refractive index matched to that of Plexiglas. (S aq. NaI- saturated aqueous sodium iodide) υ≈blood at shear rat of 500s^{-1}.
	glycerin	20%					
	H_20	1%					
van Dreumel and Kuiken (1989)	Shellflex Shellsol E		1.50	902.13 kg/m^3		$8.5*10^{-6}$ m^2/s	At 40°C, refraction index equals that of Perspex. Used at 30°C decrease evaporation. Values given at 30°C.
Fatemi and Rittgers (1994)	Dextran		1.41-1.415			Varies	Kinematic viscosity, υ = 0.034 for steady flow and comm carotid waveform and 0.08 cm^2/s for iliac waveform
	H_20						
Hayashi et al. (1996)	H_20	42%	1.46	1240 kg/m^3	6.04 cP		At 24°C. When Xanthan gum is added the fluid exhibits no Newtonian properties. Viscosity was 14.9cP and 10.2cP at t shear rates of 10/s and 100/s respectively. This viscoelastici was considered close to that of blood.
	Glycerol	26%					
	NaSCN	32%					
	+Xanthan gum	0.13%	1.48		See notes		
Kim et al (1995)	Glycerin Sat. aqueous iodide Distilled water		1.478		3.7 cP		Complex solution used for LDV at 25°C.
	Water/glycerine				3.5 cP		Used for flow visualisation. nD not required.
Lee and Tarbell (1997)	Polyalkylene glycol ether	100%	1.43	971 kg/m^3		$6.8*10^{-6}$ m^2/s	UCON 50-HB-55, Union Carbide. Properties at 45° Newtonian.

Matsumoto, T. et al, (1994)		Glycerol	5	1.46	1240 kg/m^3	6.04 cP	4.9*10^{-6} m^2/s	NaSCN added to increase refractive index (Sodium thiocyanate). Mixture: ratio of parts by weight.
		NaSCN	6					
		H_20	8					
Naiki, T. (1995) [Review of different analogue materials].		Polyacrylamide		NaSCN added to increase refractive index.		Glycerol added to increase viscosity		All were aqueous solutions. AP, CMC were Newtonian. Viscous and viscoelastic of XG solution close to that of blood; non-Newtonian.
		Carboxymethyl cellulose						
		Xanthum gum						
Naruse and Tanishita (1996)		Glycerol and water	50%	1.36		5.95 cP		Density at 23°C.
Siebes, M. (1996)		Glycerin	36%		1240 kg/m^3	3.55 cP		Fluid operating at 28°C.
		Potassium iodide	15%					
		H_20	49%					
Smedby et al (1991)		Shell Vitrea® 9	100%				13.9*10^{-6} m^2/s	At 25°C.
Rowe, C (1999)	flow vis	Glycerol	40%		1160 kg/m^3	3.65cP		@20°C , tracer particles were added for seeding, mean diameter 75 to 150 μm.
		NaCl	7%					
	LDA	Glycerol	46%	1.414	1109 kg/m^3	3.65cP		@37°C, hollow glass spheres used in seeding, 8um, diameter.
		NaCl	14%					
Yearwood et al(1989)		Physiological saline	100%					Used in LDV measurements.

Dynamic viscosity, μ ($kgm^{-1}s^{-1} = Nsm^{-2} = 10P$); Kinematic viscosity, $\upsilon \sim 1\ m^2/s = 10^4\ st = 10.764\ ft^2/s$.; Density, $\rho \sim 1000 kg/m^3 = 1\ g/cm^3 = 62.4\ lbm/ft^3 = 1.94\ slug/ft^3$. (Fluid Mechanics, Pnueli, D. and Gutfinger, C, Cambridge University Press, 992).($\mu = \upsilon\rho$). Density of blood, $\rho = 1060\ kg/m^3$ at 25°C, and viscosity, $\mu = 3.6$ cP (Siebes et al., 1996))

2.4.5 Motion of the Fluid

The blood has varying motile characteristics depending on where it is located within the body. Different experiments either use a simple steady flow or simulate any pulsatory motion as accurately as possible.

In situ the heart pumps blood around the systemic arteries by regular contractions of the left ventricle. This makes the blood flow close to the aortic valve highly pulsatile with large pressure surges and even reversed flow. This is not the case in the veins, which utilise skeletal-muscle contraction to maintain the flow of blood. A valve system, also present in the veins, prevents any significant reverse flow. As the blood moves away from the heart, via the aorta, the dynamic properties change until the flow can be considered quasi-steady by the time it reaches the Vena Cava. Therefore, the characteristics of flow will change with regard to the position within the body that the rig is meant to represent. As has been stated earlier, the blood manifests non-Newtonian properties mainly in the smaller vessels. The temperature of blood will also change as it flows around the body. Close to the heart this is not such a problem as in the aortic arch or the abdominal aorta the blood will be at approximately that of core body temperature. This may also be true for the carotid artery. However, the blood in the femoral artery, as it flows to the extremities, is subject to a counter current heat exchange across its length, which may or may not alter the temperature of the blood significantly enough to vary its properties from those at 37°C. Fortunately haemodynamics studies are generally concerned with flow local to a particular area of the anatomy and therefore changes throughout the model are of minimal concern.

Although time dependency is a major feature of cardiac flow, some experiments simplify matters by using a steady flow. However, the characteristics of secondary flow and reversed flow are only manifest when the pulsatile nature of blood flow is simulated. Quantitatively measured shear stresses have been shown to have different maximum values between pulsatile and non-pulsatile models. Also areas of recirculation are greatly affected by non-steady flows. Often such vortices are transient, something that would not be witnessed in the simpler flow scenario.

There have been many different types of pump used for these purposes and they must possess the following characteristics to be of the most value:

- Computer or mechanically controlled flow so that the physiological waveform can be simulated with a high degree of repeatability
- Non-violent mode of pressure increase, due to delicate nature of flow visualisation/LDV seeding particles. For instance an impellor driven pump may mechanically damage delicate seeding materials.

There are several types of pump that have been used for such experiments.

Segesser et al. (1984) designed a pump of unusual design that drove the fluid by peristaltic effect induced by an air pressure increase. The flow section had no moving parts and did not damage any suspended particles in the working fluid. It was also capable of producing various user-defined outlet pressures so that a physiological waveform could be simulated and faithfully reproduced.

Shi et al. (1997) used a piston arrangement driven by a cam arm which had constant rotating input translated into the vertical motion of the piston. However, various cam channels that redirected the motion laterally offset the vertical motion. In some cases the forward and reverse motions were varied by the use of different paths for each action. This allowed an output waveform somewhat similar to the desired physiological pressure wave.

Siebes et al. (1996) used a different method. The pressure was maintained by the use of a steady header tank. This was a tank placed above the experimental rig that maintained a steady head of pressure by the constant difference in height between the water level in the tank and the rig. The only pump employed by the experiment was used to move the working fluid from the lower reservoir back up to the steady header tank. An overflow from the level of the tank leading back to the reservoir maintained the pressure. Within the test section the opening and closing of two computer-controlled valves controlled the flow of the fluid, one placed fore and the other aft of the test section.

There are simpler ways to simulate a pulsatile flow. One method is to create a sinusoidal pressure change with a non-zero mean. It is possible to do this by the combination of two pumps. A steady roller pump can be employed for the basic fluid motion and the output of a piston pump is superimposed over the first, as performed by Lee and Tarbell (1997), that creates the pulsatile output. This arrangement could even be carefully modified to produce a reverse flow if the piston was allowed to refill in such a way as to affect the flow. This, however, is not usually desired. Another similar way in which this simple pulsatile motion can be produced is by the use of two unequal syringes the action of which is provided by a rotating scotch yoke (Naruse and Tanishita, 1996). The syringes are placed up and down stream of the test section and the pulsatile motion is superimposed over the steady flow provided by the steady pressure head tank.

Naiki et al. (1997) have developed a prototype valveless, pulsatile pump that has potential usage in clinical practice. Experimental results showed an output waveform similar to that seen *in vivo* from the heart. It is clear that such a pump could be applied to experimental work.

The atheropump designed by Segesser et al. (1984) has a highly versatile pumping mode. It meets the criteria mentioned earlier in this section and resembles the design of the human heart. In this manner the exact output of the heart could potentially be simulated by modification of the compression chamber to that of the left ventricle. However, this author has no knowledge of the atheropump being used in any published experimental paper measuring haemodynamics. A similar design to this is that of a ventricle, compressed by a hydraulic fluid, which is pressurised by a piston. The positive flow from the ventricle is maintained through the use of a valve arrangement. With a suitable ball valve the reverse flow of the cardiac system can be also simulated. A ball valve is not specifically required but its interference with the through flow is approximately symmetrical, unlike mechanical single-leaflet valves. This pumping method although not an accurate model of the cardiac output can maintain a high degree of repeatability and accommodate the needs of most projects.

Such a method has been seen in a potentially versatile pump (Sabbah and Stein, 1982) that employed the use of a ventricle sack periodically compressed directly by a piston. The sack is modelled on human ventricular geometries and could be replaced easily if fouled by the working fluid or for the purposes of accurate simulation of different individuals.

A modification of such a device would be the same ventricle, modelled in dimensions of the human left ventricle, but compressed hydraulically (by a non-compressible fluid) so that the mode of compression was more even and from the sides of the ventricle sack instead of purely from the leading face of the piston as found physiologically.

Although the use of steady flow does have its applications in this field, the most useful data seems to be clearly linked to that of pulsatile flow. This is due to several characteristics of pulsatile flow not manifest in the simpler flow case. These include: time dependent pressure variations, higher peak shear stresses and reverse flow that is seen close to the aorta due to the time taken for the left ventricle to empty and the aortic valve to close. Steiger et al. (1987), however, carried out experiments that showed no significant alterations in the flow patterns between pulsatile and steady flows in their aneurysm model. Peak measurement values, however, were affected. Another example of such relevancy would be high shearing noted in a bifurcation model (Sung et al, 1998) that was seen in decelerating flows. The manifestations of secondary flows are highly relevant in geometries such as the aortic arch where pulsatile flow close to the heart is known to give rise to reversed flow characteristics. Even though much research is undertaken with steady flow rigs that produce valuable experimental data, it is prudent that researchers utilise the best pump available to generate a physiologically and realistic pulsatile fluid flow where possible.

2.5 Investigations into Abdominal Aortic Aneurysms (AAA)

Work carried out to increase the understanding of fluid dynamics within AAA's has been ongoing since the 1970's. Darling (1970) conducted a clinical review detailing post-mortem evidence hoping to ascertain the variables surrounding aneurysmal rupture. It was highlighted that surgical intervention was the only clear method of treatment once aneurysmal development was underway, and that although the likelihood of rupture increased with aneurysm size, there was little evidence of a critical value at which they could be said to be 100% prone to rupture.

An AAA less than 5cm in diameter is generally considered a 'small' example and not worthy of immediate surgical consideration. However, 18% of the cadavers studied had suffered rupture of an aneurysm smaller than this value. It was also noted that postoperative success was limited and that once rupture had occurred, mortality rates were extremely high.

In an endeavour to increase clinical understanding of AAA's both numerical and experimental investigations have been carried out. Both fields of research are becoming progressively more advanced at every turn. Preliminary numerical studies into AAA flows involving pulsatile conditions were conducted by Wille (1981) showing a vortex that varied throughout the cardiac cycle. Perktold (1984 and 1987) further developed this theme. However, not until Fukushima et al (1989) was a numerical investigation combined with experimental observation.

Egelhoff et al (1999) also carried out experimental work on AAA's using LDA and full field flow visualisation in order to validate their own numerical studies. Interested in both exercise and resting conditions they investigated a range of Reynolds numbers and studied the flow regimes seen in varying sizes of AAA. Particular interest was paid to disturbed flow regimes due to their correlation with atherogenesis and thrombogenesis. As such the peak Reynolds numbers were $3308 < Re_{peak} < 5696$ indicating turbulence. Asbury et al (1995) also suggest that turbulence may be a contributing factor to aneurysmal rupture.

In a continuing investigation into the factors contributing to aneurysmal rupture researchers have expanded the understanding of aneurysmal flow. Moore and

Ku (1994) carried out an investigation into the variation in flow effects encountered due to exercise and postprandial conditions. These included considerations into the negative velocities stages of AAA flow and different flow regimes seen during higher flow rates, which occur to due to both an increased cardiac output and constriction of the branching arteries of the abdominal aorta.

Elger et al. (1996) considered the implications of AAA shape upon the stresses found in AAA's. This numerical investigation proposed that the curve of the aneurysmal wall was more directly linked to the stresses encountered by the vessel wall than bulge diameter and presented this alternative method of prognosis with regards to predicting aneurysmal rupture.

Non-planar arch flow was investigated by Fujioka and Tanishita (2001) revealing varied distributions of wall shear stress and also that the direction of wall shear stress was seen to change in select areas due to flow reversal near the wall under pulsatile conditions. This study concluded with effects found upon endothelial cell morphology. However, it can plainly be seen that proximal areas will also be affected by such flows.

The conclusions drawn from many of these publications are that wall shear rate (WSR) and turbulence have a decisive roll to play in atherogenesis and the eventual rupture of aneurysmal locations.

2.6 Swirling in the aorta and non-planar flow

The swirling in the aortic arch has been comprehensively investigated in past literature to the conclusions that helically induced flow torsion is not to be discounted in detailed flow studies of the descending aorta.

Preliminary work carried out clinically by Kilner et al (1993) observed the secondary flow characteristics and investigated their origins using magnetic resonance scanning. Further work carried out by Black et al (1995) numerically considered the effect of an out of plane inlet to the ascending aorta. In this latter study the effects of inlet plane were studied to ascertain how aortic flow is developed.

Conventional fixed pipe dynamics through a curve in one plane produces not a single uniform flow, but two symmetrical counter-rotating vortices that propagate through the curve beyond its exit. This feature of conventional arch flow was reiterated by experimentation carried out by Black et al (1995) for purposes of a control. Both papers concluded that this is not seen in the aortic arch. The primary reason for this is the out of plane inlet, which produces impingement on the wall during fluid entrance. As such the vortices produced during peak flow are not evenly distributed and the symmetry is skewed until one vortex dominates the other to the point of eradication of the smaller at the apex of the arch for a grossly out of plane inlet. More realistic helical aortic models show this characteristic further down the arch. However, a single swirling flow was documented by Kilner et al (1993) for both *in vivo* and *in vitro* observations lending credence to the theory of swirling flow as a component of aortic haemodynamics.

Caro et al (1996) also considered the non-planarity of the aortic arch to be critical when considering aortic flows. Zabielski and Mestel (1998) studied fully developed steady flow in a varyingly helical pipe altering the pipe's torsion and curvature. They concluded that the secondary flow transmuted from a single vortex to a pair of symmetrical vortices as the Dean number increased (See Dean (1927) where a pair of symmetrical vortices is described as 'Dean flow'). In their further studies they showed that during pulsatile flow variations in wall shear stresses were reduced by increasing the non-planarity of the helical tube. This factor, they concluded, supported a theory put forward by Kaiya and Toagawa (1980) that arterial shape is adapted to reduce excessive shear stresses.

The presence of mainstream swirl in steady flow case studies of aortic arch haemodynamics is evident from the simplest of *in vitro* experiments, However, pulsatility has an effect upon the nature and expression of this flow torsion due to it's time dependant nature. Close to the heart flow is highly pulsatile and during diastole velocities decrease to zero or, in part, reverse flow can be observed. As such there is little 'memory' of the flow carried over from cycle to cycle.

2.7 Conclusions

It can be clearly seen that the way to advance in this field is to construct increasingly more realistic rigs that simulate *in vivo* conditions without flaw and to apply more accurate measurement techniques and methodologies to these apparatus. This, it seems, is near to impossible, as the variables that arise when simulating the human body are innumerable. However, the rigs built by researchers today increase our understanding of haemodynamics in many varied geometries as the differences between the experimental and genuine situations becomes less apparent. However, modern experimental researchers, regardless of the complexity of their apparatus, have to date rarely considered the inlet boundary conditions of the blood in their experiments. A Poiseuille flow profile would not have the required length of geometry in the human body to fully develop and many experiments compromise with a blunted inlet profile. MRI or U/S data could provide this information but is rare and such profiles change continuously throughout the body. For example in the aortic arch the blood is highly pulsatile and torsional in motion. It is pulsed through a three-dimensional turn as it enters the abdominal aorta, which is also a location of interest. Therefore, the velocity profile through an abdominal aortic aneurysm (AAA) would be skewed on entrance. Ideally a rig should be made simulating the cardiac operation. A ventricle sack, compressed correctly, could simulate the motion whilst the aortic arch would be present to create further influence. The velocity profile entering the abdominal aorta would hypothetically be more accurate to that seen *in vivo*. Similarly other major arteries could be simulated in this mock circulation loop. There is a trend at present to investigate out of plane flow in arteries (Kilner, 1993. Black, 1995. Caro, 1996. Rowe, 1999).

With regards to aortic geometries, aortic arch flow especially contributes a torsional flow component. Branching of arteries in the aortic arch and thoracic aorta also have relevant effects upon the distal flow field (Mori and Yamaguchi, 2001).

Numerical work specifically interested in branching arteries has been carried out for abdominal aortic aneurysms by Khraishi et al (1997). The effects of distal arterial branching upon AAA flow dynamics were investigated (specifically the renal arteries) and their relation to wall shear stress and pressure. It was concluded that there was little effect upon WSR, but a drop in the pressure seen in the AAA. However, once again this study was limited to fully developed laminar inlet boundary conditions and low Reynolds numbers representing the mean velocity of resting physiologic flow.

Shahcheraghi et al (2001) demonstrated a shift in the skewness of the aortic flow to the outside of the aortic arch and drew conclusions with regards to the localisation of atherosclerotic lesions. They suggested a link between atherogenesis and regions of extreme maxima or minima of wall shear stress or pressure. Their conclusions indicated a relevance of the aortic arch and torsion to the determination of location and development of diseased lesions.

The numerical work of Zabielski and Mestel (2000) concluded that helical flow could affect both flow separation and perhaps wall shear and summarised their paper with the statement that helical flow due to non-planar wall curvature should not be neglected in detailed flow studies.

Chandran (1993) also detailed the aortic swirl in experimental flows and remarked upon its effects upon distal flow regimes. The author comments upon the uniform or parabolic entry flow used in previous investigations. The presence of torsional flow in the descending aorta and its potential effects upon geometries as far into the systemic circulation as the aortic bifurcation is also documented with reference to *in vivo* investigations.

The literature survey has highlighted the complexity of flows occurring in vascular geometries, which makes accurate modelling of abdominal haemodynamics extremely challenging through both experimental and numerical means. Only in the last few years have researchers endeavoured to include out-of-plane and non-conventional inlet boundary conditions in their work however, this has been to the exclusion of haemodynamic studies of the abdominal aorta. To the author's knowledge there is a severe paucity of work carried out using anything but conventional and two-dimensional inlet boundary conditions (for either steady or pulsatile flow cases) into the investigation of aortic abdominal aneurysmal geometries and their associated flow regimes.

The work presented in this thesis cannot address all of the issues discussed but will introduce appropriate inlet boundary conditions to the study of abdominal aortic aneurysms to provide new and timely data on haemodynamics appropriate to this flow geometry. An improved physical understanding of the flow will be achieved. In particular this will include effects upon the flow field, areas of recirculation or stagnation and distal wall shear stresses.

APPARATUS AND METHODOLOGIES

Presented here is the information required in the construction and commissioning of equipment used in the experimental investigation. Included are details of the pump workings, creation and design of the AAA model and also practical details of the workings of LDA and settings used in its operation (full reference on the LDA can be found in the equipment manual (Dantec, 2000)

3.1 Pulsatile Waveform Generation

3.1.1 PUMP MECHANISM

The pulsatile waveform generated by the apparatus was designed to simulate the cardiac output of the average human heart.

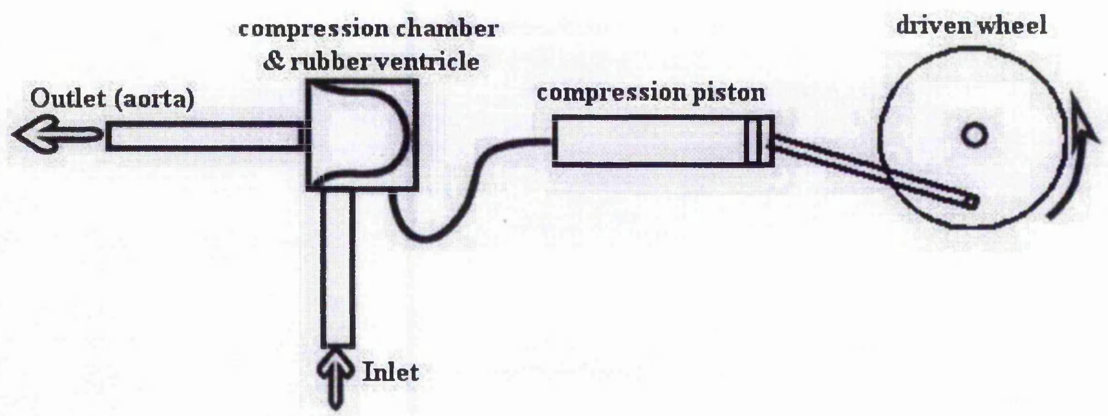

Figure 3-1 Basic Set-up of pulsatile flow apparatus

This was achieved by the use of a large electrical rotary motor, which in turn drove a piston moving a fluid cyclically under pressure. This fluid was driven into a pressiure chamber where it compressed a latex sack used as an analogue of the left ventricle of the human heart.

3.1.2 ARTIFICIAL VENTRICLE CHAMBER

The chamber itself was manufactured out of aluminium for ease of manufacture, cost and durability against stresses and corrosion. The chambers maximum external diameter was 100mm and its length was 200m in total. Internally the chamber allowed a maximum expansion of the ventricle to 80mm and 100mm laterally and length-ways respectively. This allowed for the potential to accommodate many different modes of compression, although complete compression of the ventricle was never required in the simulation of human physiology.

A 1mm width mesh was set in place over the inlets/outlets and the hydraulic inlet. Secured to a small ridge manufactured within the housing, this prevented the latex from being drawn into the inlet pipes during the stages of hydraulic pulsatility.

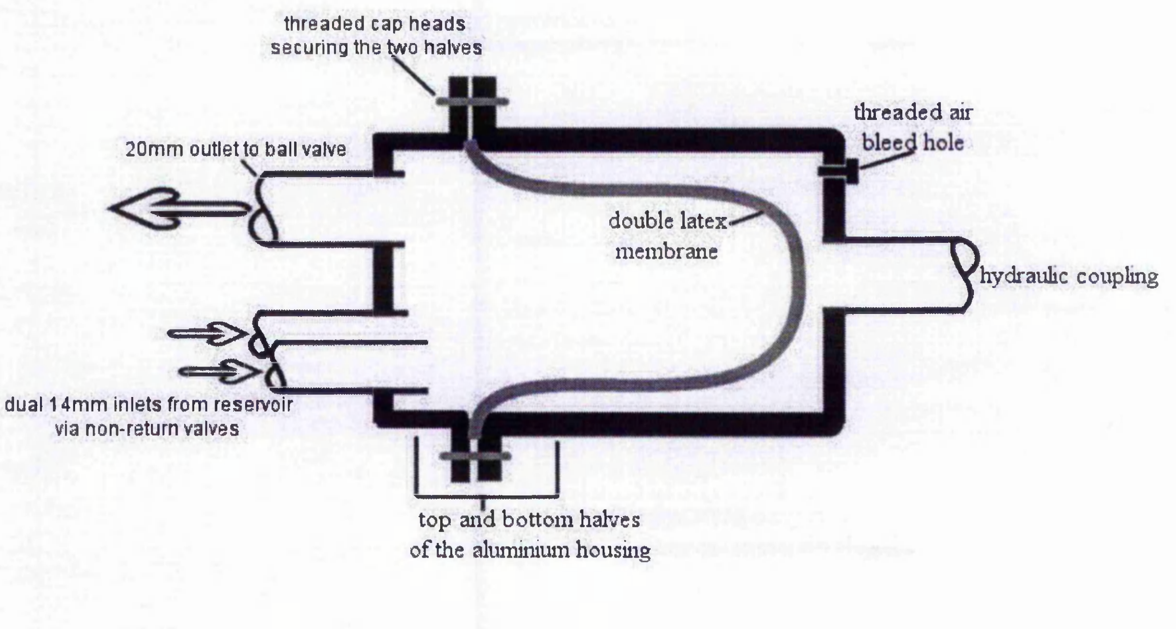

Figure 3-2 Detail of aortic compression chamber

A series of flow control valves were used to maintain refilling of the ventricle and the subsequent expulsion of the analogue fluid into the outlet conduit. This continuous cycling produced a highly repeatable pulsatile output with properties mimicking that of the human heart (peak output varied by no more than 8%). Ethylene glycol was used as the hydraulic fluid as it was considered to be non-corrosive or oxidising to the metal parts of the piston and compression apparatus. The ethylene glycol was also tested with regard to its interaction with the latex of the ventricle contained within the compression chamber. No adverse effects were seen to occur to the latex in 3 weeks of direct and concentrated exposure.

3.1.3 PUMP OUTPUT

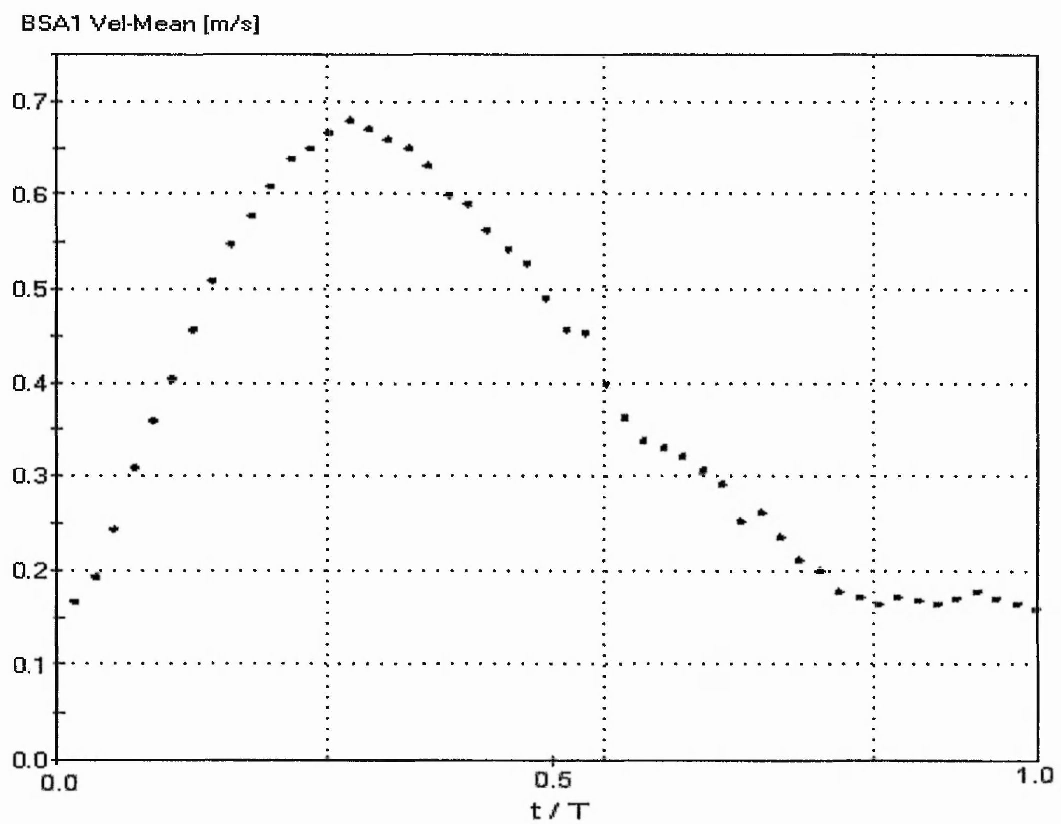

Figure 3-3 Plot showing unsteady fluid velocity exiting from the pulsatile pump

The output form of the pulsatile wave, represented in Figure 3-3 above was measured at the centre of the inlet to the AAA. It shows a broad systolic peak, appropriate for the simulation of a waveform associated with moderated exercise (Egelhoff et al, 1999). This was chosen to simulate not resting conditions, when any haemodynamic stresses would be at a minimum, but at moderate exercise levels found commonly in the population during a working day either walking or when the body has greater than basal requirements. Extreme exercise conditions would not be appropriate for the demographic studied (males over the ages of 50) nor would they represent haemodynamic conditions maintained for any length of time.

The Womersley parameter for this artificial flow is discussed in section 3.1.4 and was calculated to be 15. The peak Reynolds number for the flow at systole was calculated to be 4200.

It was also of interest to model disturbed flow regimes. Non-turbulent flow is more easily and reliably modelled numerically. The modelling of turbulent or transitional flow within the human body is both haemodynamically relevant and of more substantial use to those interested in modelling abdominal aortic aneurysms under strain. Also as noted in Chapter 2 the oscillating wall shear attributed to disturbed flow has been linked with the development of atherosclerotic lesions.

The stroke volume of the pump was set at 50ml for the duration of this investigation. Physiologically, 70ml of blood is expelled from the left ventricle via the aortic valve. However, not all of this volume passes through the abdominal aorta. Mass flow is lost in the branching of the arteries distal to the abdominal aorta. These arteries include the small coronary arteries, the innominate, left common carotid, and the left subclavian arteries of the aortic arch and the celiac artery and renal arteries of the abdominal aorta. The volume lost to these arteries varies greatly, dependant upon the body's requirement. For example, during exercise the volume of blood escaping the abdominal aorta via the renal arteries has been seen to decrease by 25% of the normal and that leaving via the celiac artery by 50%. These conditions see the total blood flow rate from the human heart to more than double to 240% of its original output (Moore and Ku, 1994). Furthermore, *in vivo*, there is considerable tapering in the aorta as it descends through the thorax and abdomen. This occurs in order to maintain the pressure of the flow as the blood volume decreases and the effects of pulsatility are subdued due to the elastic action of the vessel walls. In the model presented here an average of the aortic diameter was maintained throughout and as such a compromise on the stroke volume passing through the model AAA was made.

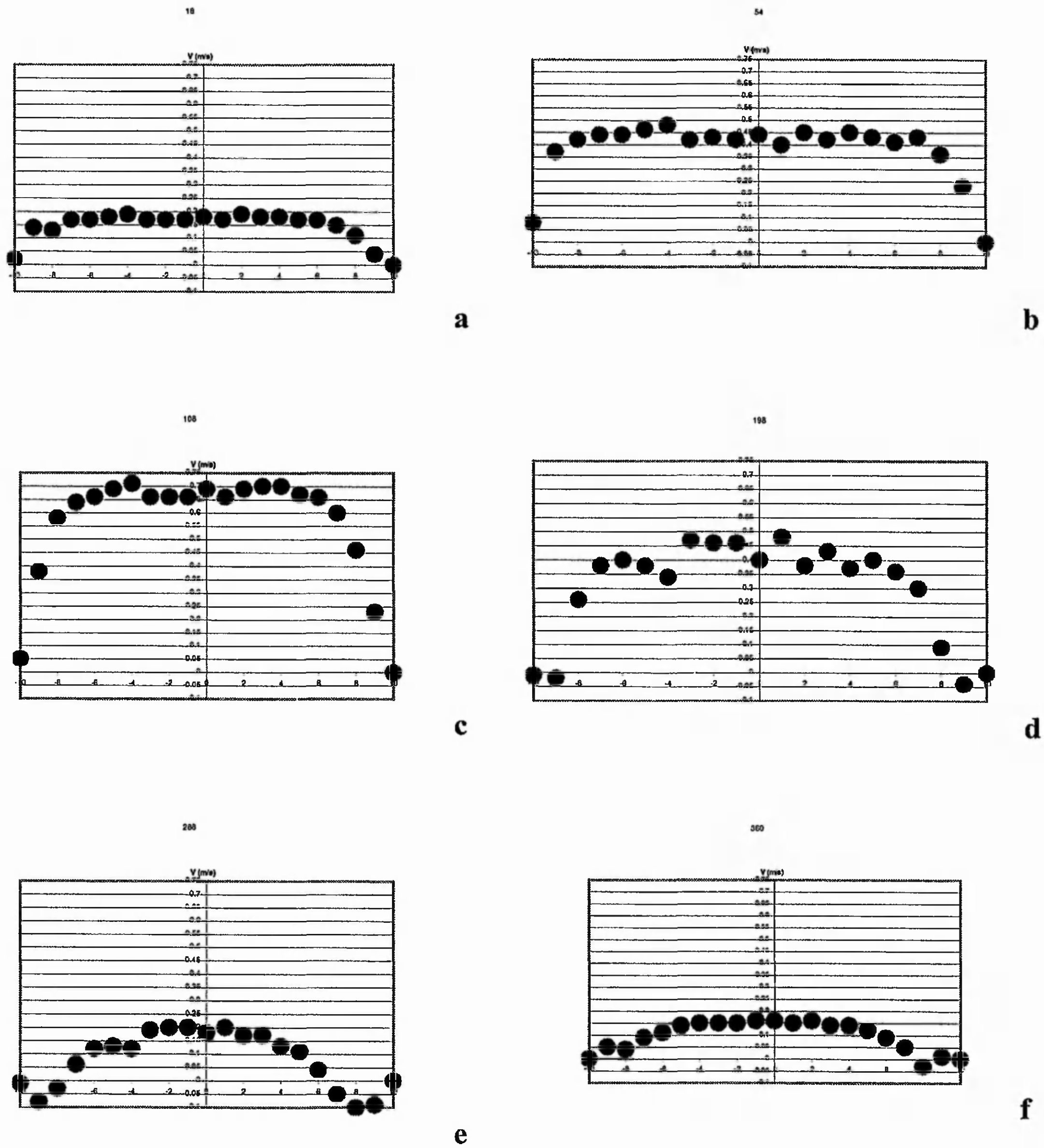

Figure 3-4 Cross-sectional plots showing waveform development through the pulsatile cycle

Figure 3-4 shows the development of the wave front in the simulated abdominal aorta. Each represents a 1/20th of the wave forum from the preceding angle bin shown in the graph title. Figure 3-4a is the commencement of systole and b shows the accelerating waveform before peak systole. This is the most developed the inlet profile becomes. This complete acceleration occurs in the first 1/3 of the wave cycle. The deceleration phase of the flow consumes 3/5th of the total cycle time and can be seen in Figure 3-4d and e. During this time negative velocities are seen adjacent to the walls causing a reverse of the near wall velocity gradients. Figure 3-4f shows the recovery or resting phase of the flow where the velocity gradients near the wall are relatively neutral and the basal centreline velocity is prevalent. This state continues until the cycle repeats and the flow accelerates once again as in Figure 3-4a.

3.1.4 WOMERSLEY PARAMETER, α

The Womersley number is a dimensionless scalar describing an aspect of a time-dependant flow. It is defined by the equation:

$$\alpha = r\sqrt{\frac{\omega}{\nu}}$$

where: r is the radius of the vessel

ω is the angular frequency 2πf

ν is the kinematic viscosity

For flows with a large α, the velocity profile is seem to be flat, whilst a smaller α shows a pulsatile flow showing large velocity peaks.

For the pulsatile flow system used in this experimentation, α was calculated to be 15. Studies of this nature generally exhibit a Womersley parameter of 6-22 (Taylor (1994), Egelhoff et al. (1997), Yu (2000), Fujioka and Tanishita (2001))

However, this parameter does not comment upon the duration of driven pressure in each flow cycle as the pressure wave is no sinusoidal. However, the frequency of the cycle is taken into account.

3.2 Timing Interface for Pulse Synchronisation

It was important to interface the pump mechanism with the Burst Spectrum Analysers (BSA) so that a reset pulse could be sent to the apparatus at the beginning of each cycle. For this purpose a simple circuit was incorporated to interface with the pump. An optoelectronic switch (FESTO SOEG-RT) was used to activate the signal voltage that was switched by the rotation of the wheel driving the piston pump. Half the wheel was blacked out to be non-reflective for this purpose. The signal was then transmitted to the relay (HRS2(H) Relay) via which a 5V square wave was produced (TTL levels required by the BSA). A BNC connector was used to input the signal to SYNC1 on the BSA rear panel. It is worth noting that the negative slope of the square wave signalled the reset pulse.

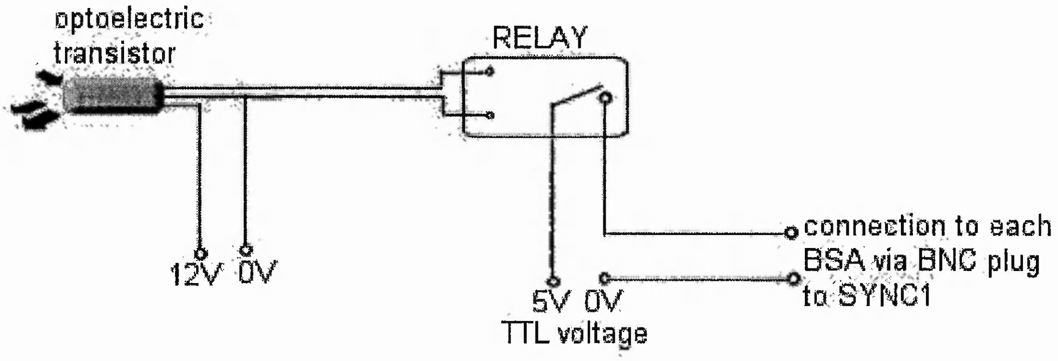

Figure 3-5 Circuit used to create RESET pulse for the cyclical flow interface

The sensor had a frequency response of 800Hz and the relay operate and release maximum times of 6ms and 4ms respectively. The cycle time was~0.7s. The repetitive error in this circuit had a potential maximum of ~11ms or 1.5% of the total pulse time. This was non cumulative over many cycles as the triggering mechanism was independent of the electronics.

3.3 Flow Control/ Air Release

Further additions to the flow rig were made in the form of a pressure chamber. This allowed a more mediated pulsatile wave to be produced. The additional benefit of this was to filter out air bubbles that had been introduced into the flow. This occurred due to either simply through air trapped in the setting up of the apparatus or due to air coming out of solution due to the pressure changes experienced by the fluid.

Excess air was released immediately via a mechanical valve (*Minical* manufactured by Caleffi (RSS 313-7032)), which maintained the pressure lock required in driving the flow. A cylinder of wire mesh was also inserted to limit the presence of large air bubbles in the resulting outlet flow. This system was utilised in both the steady and pulsatile flow measurements.

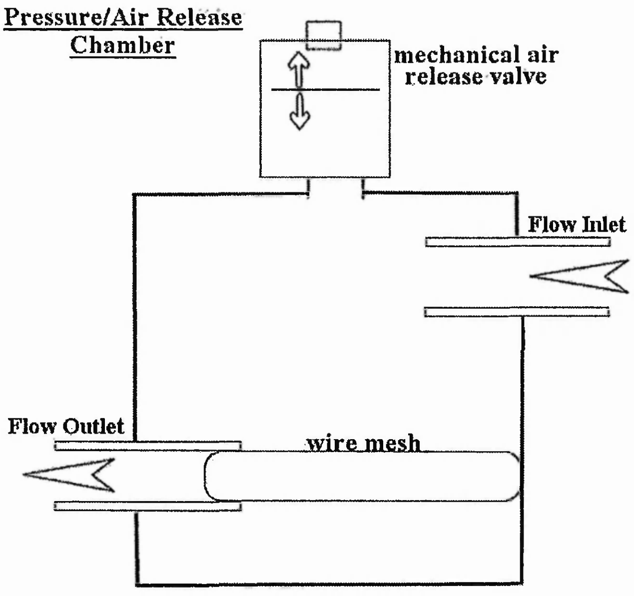

Figure 3-6 Detail of pressure control/air release chamber

3.4 Aortic Arch

The geometry of the aortic arch was simulated by recreating the required curve through three-dimensions with PVC tubing. This could be easily straightened for comparison with more conventional inlet boundary conditions. Inlet boundaries such as this are often ignored in other studies. Including any relevant torsional motion in the inlet boundary conditions could better simulate aneurysmal flow conditions close to the heart.

The geometry was decided upon by examination of many aortic cadaver castings in resin and the examination of magnetic resonance images (Hose, R., 2002). The geometry was simplified from the *in vivo* measurement so that it was representative of the demographic studied, but also so that it could be replicated in both computational and in engineering terms.

The main curvature of the arch takes place in one plane, whilst the ascending and descending aortic vessel angle off from the inlet and outlet datum of the main arch respectively. For simplification, the aorta was modelled as having a constant diameter of 20mm. This represents the average diameter of the aorta in the demographic studied. Tapering was discounted due to limitations in the rig and also in a desire to not introduce more than one modification of the geometry at a time. Compromises were also made in that the brachial arteries and renal arteries were not present in the aortic model. Although these outlets would affect the state of the aortic flow they were omitted from the model for two reasons.

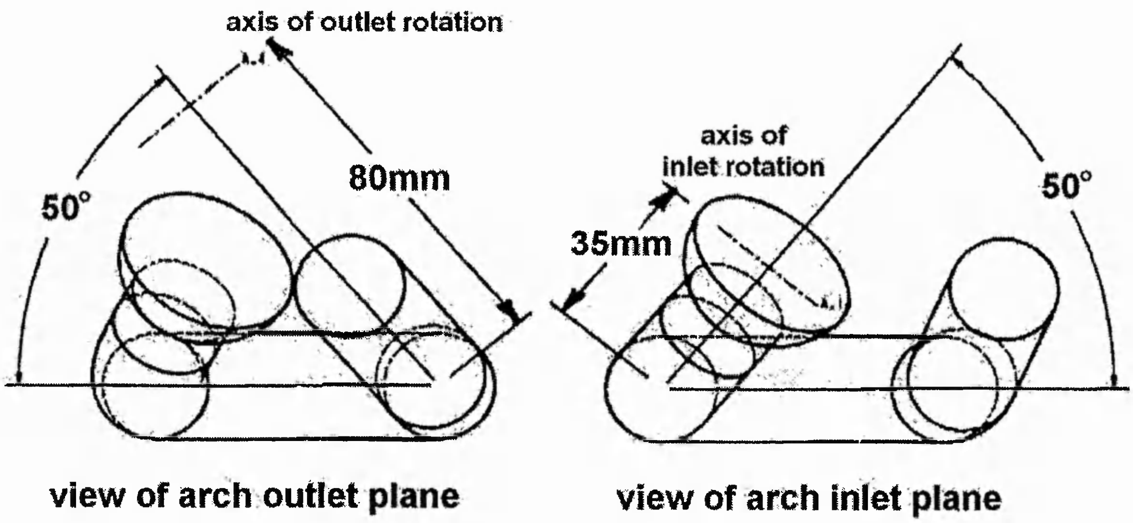

Figure 3-7 engineering diagram showing inlet/outlet geometries of the aortic arch

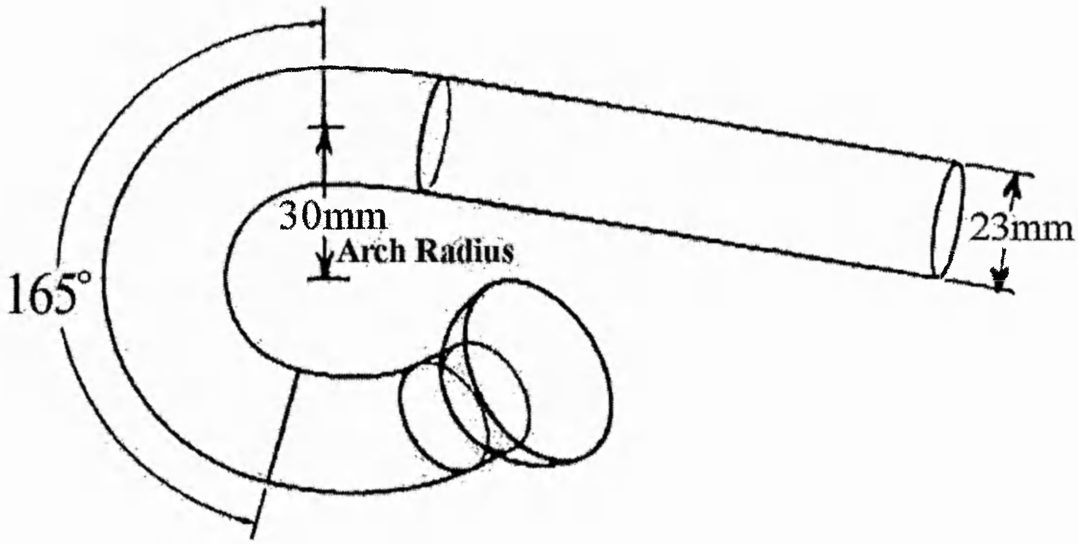

Figure 3-8 engineering diagram showing overall curvature of the aortic arch

Firstly, it is the aim of this project to introduce more physiological characteristics to the study of abdominal aortic aneurysms. This is best facilitated by the addition of one novel modification of the rig at a time that better mimics the *in vivo* geometry. Therefore it would not be suitable to introduce such multiple features, as the true effect of each new modification must be studied in turn. Secondly it was not possible, in the scope of this project, to accurately determine the *in vivo* flow rates and bulk fluid losses to these multiple branching arteries. To misrepresent the effects incurred upon the aortic flow would be highly detrimental to the quality of the data produced. As such the possibility of including brachial and renal arteries in this investigation was excluded. With this in mind, the diameter of the aortic arch was fixed at 20mm. Even though the aortic arch tapers within the human body and varies between ~18-23mm in its extremes, it would be unwise to taper a model that does not include the fluid mass lost to extraneous arterial branches. As such, any tapering would increase the pressure in the vessel, a pressure increase that is used to maintain the flow *in vivo* but would not be here required as the fluid mass entering the aortic arch is equal to that entering the abdominal aorta in the experimental representation.

3.5 Aneurysmal Model Casting

3.5.1 SPECIFICATIONS OF THE AAA MODEL

The AAA modelled in this series of experiments was designed as to represent extreme aneurysmal conditions. The aneurysmal bulge expanded rapidly to its full diameter smoothly and was axisymmetric in both rotations. The inlet was set at 20mm as the outlets from the AAA were of identical diameter of 14mm angled at 35° from one another. The ratio of aneurysm diameter to inlet diameter (D/d) was 3.3, representative of extreme conditions found clinically. The bulge length was designed to be 4.4d, allowing a smooth gradient along the wall comparatively similar to work carried by other researchers (Asbury et al, 1995).

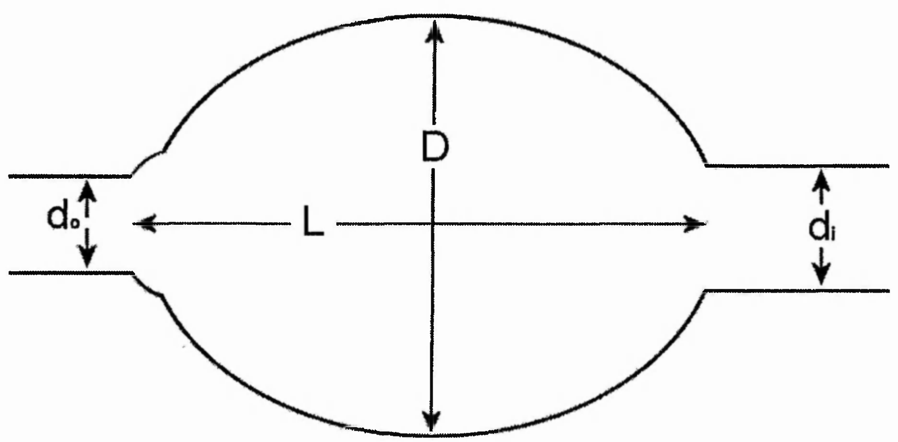

Figure 3-9 Diagram of AAA ZY profile view

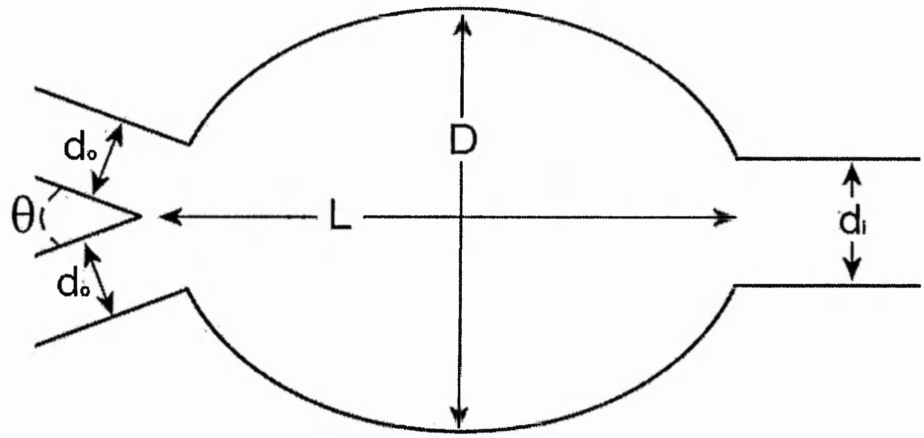

Figure 3-10 Diagram of AAA XY plan view

Table 3-1 Featured dimensions of aneurysmal model

feature	*nomenclature*	*value*
Diameter of inlet	$\mathbf{d_i}$ **or d**	20mm
Bulge length	**L**	88mm
Bulge max. diameter	**D**	66mm
Diameter of outlets	$\mathbf{d_o}$	14mm
Angle of bifurcation	$\boldsymbol{\theta}$	35^{o}

Detailed engineering diagrams of this geometry can be found in the appendix D.

3.5.2 HAND CASTING OF THE MODEL

A variety of casting procedures were investigated. The large aneurysm was cast using suitable plastic vessels in to which was poured molten MCP-58 (a low melting-point alloy, melting point 58 °C, Mining and Chemical Products Ltd). Having filled the mould, the MCP-58 was allowed to cool naturally to its solid state before further stages. Each component part was then machined so that an assembly could be constructed. The aortic inlet and outlet iliac arteries were cast separately and subsequently machined so that they could be inserted into predrilled holes in the cast aneurysm. The aneurysm itself was cast in two parts, which were drilled and then sealed together using molten MCP-58. The resultant whole was then hand finished to remove any burrs or damage done during the handling of the cast. The surfaces were also lightly sanded and polished to produce a smooth, near-mirror finish that would be replicated in the next step of the process.

The core was then suspended in an acrylic box of plain surface and the artery outlet/inlets attached to allow connection to the flow apparatus. Any gaps were sealed where they exited the acrylic box by using silicon sealant to prevent loss of the silicone elastomer from the moulding process. The casting cores were also sprayed lightly with black spray paint. This was to aid the released of the core material from the wall under melting conditions. After drying, the paint was also sanded with fine wet and dry paper to enhance the wall finish.

De-aerated silicone elastomer (Sylgard-184, Dow Corning, UK supplier R.W Grief) was then poured slowly into the completed casting box. At this stage it was important to prevent the mixing of air into the compound. This was previously mixed from its bulk and curing components and then immediately placed in a vacuum oven. This was left in the oven at room temperature and 0.5 Atm for one or two hours or until all air pockets were seen to have bubbled off and the remaining elastomer was clear and readily transparent to the naked eye.

This material has been used successfully in previous research by those such as Rowe (2000) and Asbury et al (1995).

After carefully pouring the Sylgard-184 into the prepared casting box the completed item was transferred to a vacuum oven set at 25-30 °C and left for 16 hours to allow the elastomer to completely cure into a resilient rubber-like material. Low pressure was maintained during the curing stage of the process to allow any unwanted air bubbles to be removed if any were introduced in the pouring of the silicone elastomer. The heating of the Sylgard-184 during the casting procedure also facilitated the removal of any remaining air bubbles in the cast due to their change in density. Surface air pockets also were lifted from the cast in this fashion. Due to this requirement it was decided to cure the silicone elastomer over a prolonged period of time. A faster curing time may have hindered this air bubble removal.

Once the Slygard-184 was fully hardened the model was tilted and the oven temperature increased to 60 °C so as to melt the alloy and allow it to run freely from the model into a drip tray; for collection and recycling for the next casting procedure. In the use of the wax core, the oven temperature was substantially increased to that of 100°C to allow the wax to melt. Sylgard184 is not affected at this temperature.

When the model was free of the core material the oven was allowed to cool to prevent unnecessary handling of the molten material. The model was then cleaned using a small brush, water and a non-abrasive detergent. The aluminium inlet and outlet pipes were then removed and reattached, using a high modulus silicone sealant which doubly acted as an adhesive, to the model so as to facilitate the attachment of the rubber tubing and connection to the pump apparatus.

Thus a versatile cast was produced of an aneurysm through which a refractively matched fluid could be pumped and optical access provided. The refractive index of the cured Sylgard-184 was tested to be 1.43.

Alternate casting methodologies were investigated in the design of the apparatus. Each one suffered from flaws or was unfeasible in the scope of this project, details of which can be found in the following sections.

3.5.3 3D PRINTING

The casting of a smaller aneurysm was carried out via a simpler method. The equipment used was not available to the author during the earlier stages of the research.

The geometries of the model, used somewhat in the design of the previous model were described in a parametric computer-based design package (Pro-Engineer) which was then exported as a solid geometry of polygons (STL based format). This data was used to create a representation of the aorta and its aneurysmal geometry in a solid form of wax. This was carried out in a 3D printing apparatus (3D Systems, ThermoJet). The core created was then used in the same manner as that of the MCP58 in the fashion described above. The cast was finished by hand to produce a smoother wall.

However, flaws in this technique became apparent in the final processes of the casting. The penultimate stages of the casting were carried out as above for the metal (MCP-58) core, however, the printing wax was seen to melt unreliably until an oven temperature of >90 °C was attained. At this point dye colouration from the wax was seen to bleed into the elastomer surrounding the model, even through a layer of black paint used to prime the wax model. This additional colour in the mould created a halo around the geometry that rendered the unit unusable for reliable optical access.

Furthermore, in the printing and cooling of these geometries some deformation and shrinkage was seen in the linear planes involved in the model. It was proven impossible to predict or compensate for these changes. An additional problem occurred when it became apparent that the finish on the wax model was inferior to that obtained from the metal core, as it was less susceptible to hand polishing. The resultant model exhibited a wall less useful in the application of flow visualisation techniques.

3.5.4 C&C MACHINING

Another avenue of casting was pursued in the form of C&C lathe machining. Hypothetically a metal or acrylic outer cast can be machined from data inputs taken from a parametric design package. The subsequent mould, made in two parts, could then be polished to a suitable standard and assembled. Molten MCP-58 could then be poured in to set as a solid core and after cooling and polishing, the rest of the procedure followed. This route of casting was abandoned though in its early stages due a lack of facilities available capable of creating moulds of a suitable size. Also the finish on the moulds would be of low quality depending upon the machinery available. External manufacture of these items, when investigated, was seen to be financially prohibitive.

3.6 Blood Analogue Fluid

The analogue fluid was composed of a mixture of glycerol, water and sodium chloride (NaCl). This enabled both the viscous properties and the density of the blood to be approximated. The non-Newtonian nature of the flow was not considered during this investigation as large arteries were exclusively investigated. The non-Newtonian properties of blood are mainly manifest in the smaller capillaries. The fluid was then seeded for LDA experimentation with glass micro balloons (Dantec Technology Ltd, Bristol, UK). A mild particulate-based disinfectant was also added the analogue mix (subsequently filtered to <5μm in size) in order to increase the shelf life of the blood mimic. The composition of the analogue fluid was an aqueous mixture of 42% glycerol (by mass) to which was added 25% (by mass) NaCl to saturation. This resulted in a clear fluid of refractive index 1.413 @20°C. Dynamic viscosity was calculated to be 4.0cP and density ~1.1kg/m^3. A sample of analogue fluids used in comparative investigations can be found in Chapter 2.4, (Table 2-1).

Grigioni et al (2002) recently discussed the role of shear-thinning viscoelastic properties of blood. Nonlinearity and the influence of erythrocytes upon the viscosity of blood become more relevant at low shear rates (<100s^{-1}) as well as in smaller vessels such as capillaries. Therefore the use of Newtonian fluids as a blood mimic is only appropriate at shear rates of >100s^{-1} due to the viscoelastic properties of whole blood. After which assumptions regarding the properties of blood or an appropriate analogue become innacturate.

3.7 Flow Visualisation

Flow visualisation was carried out using a laser component of the argon-ion laser array and cylindrical lens array to illuminate a longitudinal section of the flow field. Seeding was used to visualise the flow phenomenon. Pryolite was used as the particles were considered to be large enough for the desired effect and neutrally buoyant. A digital video camera was then used to record the full field of flow to magnetic tape. The results from such experiments were not included here, although observations were made which corroborate qualitatively the findings from the LDV experimentation.

3.8 Laser Doppler Velocimetry (LDV)

3.8.1 ADVANTAGES OF LDV

Laser Doppler velocimetry (LDV) is an optical technique used in the quantitative gathering of point velocity and statistical data.

This experimental technique has four advantageous features that recommend it to fluids research.

LDV is non-intrusive and can be used in contained flows where optical access is available. The measurement volume does not affect the flow regime and as such is able to collect more valid data than techniques requiring physical interaction with the flow

LDA requires little calibration once the optics have been accounted for, and there is no drift in the data collected. The measurement technique is based upon the principles of electromagnetic wave propagation and which for most laboratory situations are unaffected by ambient variables such as temperature and pressure.

The temporal and spatial resolution of the LDV measurement technique can be tailored for the situation monitored. Using appropriate optics it is possible to create a small measurement volume that can be used to measure at several points within 0.5mm of a surface. The fast processing capabilities of specialised hardware also make it possible to measure in small time bins allowing fluctuating velocities to be measured accurately as there is no response delay as might be found for example in hot-wire anemometry techniques. The frequency response to a change in the flow field is limited only by the inertial or momentum induced 'lag' of the seeding particles if they fail to be true to the flow. In liquid LDV techniques the seeding particles are of sufficiently small mass and size (~5 μm) that this latency of response is extremely low. The data rates required for high temporal resolutions are limited by the rate of flow and the concentration of seeding within the medium. This would only be a limiting factor where the flow was of extremely low velocity and the seeding passing through the measurement volume was not of sufficient quantity to provide adequate data rates.

LDV systems of different wavelengths can also be employed in unison to measure two or even three directional components simultaneously within the prescribed area of measurement. Due to the different wavelengths there would be a negligible difference in the number of interference fringes within each of the measurement volumes and also the measurement volumes would vary minutely in dimensions. However, data can be collected showing all three velocity vectors simultaneously.

LDV is not without its shortcomings but these properties of the techniques make it particularly suited to *in vitro* studies of vascular haemodynamics.

3.8.2 PRINCIPLES AND THEORY

When two coherent light sources cross, interference patterns are created by the constructive and destructive interaction between different wave fronts. Where two wave fronts cross that are out of phase, mutual annihilation occurs, where the two wave fronts are in phase an interference fringe is produced. In LDV this is manifest by the intersection of two coherent laser beams at which point a three-dimensional volume is produced. It is in this volume that interference fringes occur. The alignment of these fringes is parallel to a line that bisects the angle at which the laser beams converge.

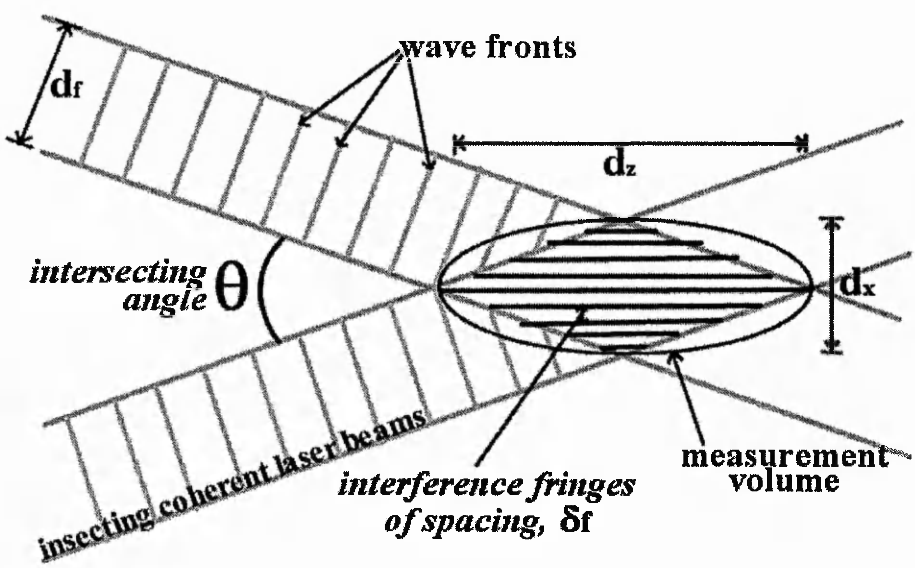

Figure 3-11 A model of interference fringe generation due to intersecting laser sources

When the measurement volume is projected into a fluid medium, particles within the flow pass through the measurement volume and through each of the interference fringes. Light is scattered by these particles but a shift in the frequency of the scattered light occurs that is directly proportional to the particle's velocity. This light is then detected by a photo multiplier tube and after amplification the frequency of the light is derived by specialised hardware. Where a fluid medium does not contain light scattering particles, such as pure water or air, artificial seeding must be added to facilitate matters. It is important though to select seeding appropriate so that the seeding faithfully follows occurrences within the flow field.

3.8.3 Experimental Configuration

The LDV system used in this investigation was a DANTEC four-beam two-colour fibre-optic based laser Doppler velocimeter. It was comprised of a 300mW argon-ion laser system (Ion Laser Technology), which passed into a transmitter unit (itself consisting of a beam splitter, a Bragg cell for 40Hz frequency shift, and a colour splitter). The four beams, two of each component colour (488nm, 514.5nm) travelled down a fibre optic connection to the probe housing. The probe head employed was a 38mm Dantec unit coupled with a 1.98x beam expander. The beams were focused through a lens of 310mm focal length. This was used so that the intersection angle was larger than conventionally utilised and the measurement volume in the axis of the laser beams was relatively small (1mm length, 250 μm diameter). In contrast a probe set-up without the use of a beam expander and with the default front-end lens (focal length of 600mm) would produce a measurement volume that was ~5mm in length.

The light received by the back scatter optics was collected and transmitted back down the fibre optic cable and via the transmitter again to a pair of lambda filter protected photo multiplier tubes (PMT). Data from each PMT was then fed to one of two burst spectrum analysers (BSA) that handled the data before being passed onto a data collection computer (via IEEE4888 interface and GPIB board). Waveform data was also output from the BSAs to a 2-channel oscilloscope in order that the Doppler waveform could be dynamically monitored. The computer was also linked via a serial interface to a 3D traverse mechanism on which the probe was mounted. The traverse and data collection was handled by specialised software provided by Dantec Dynamics. The traverse was able to operate to a spatial resolution of 12.5μm in the horizontal planes (X and Y) and 6.25μm in the vertical (Z) plane.

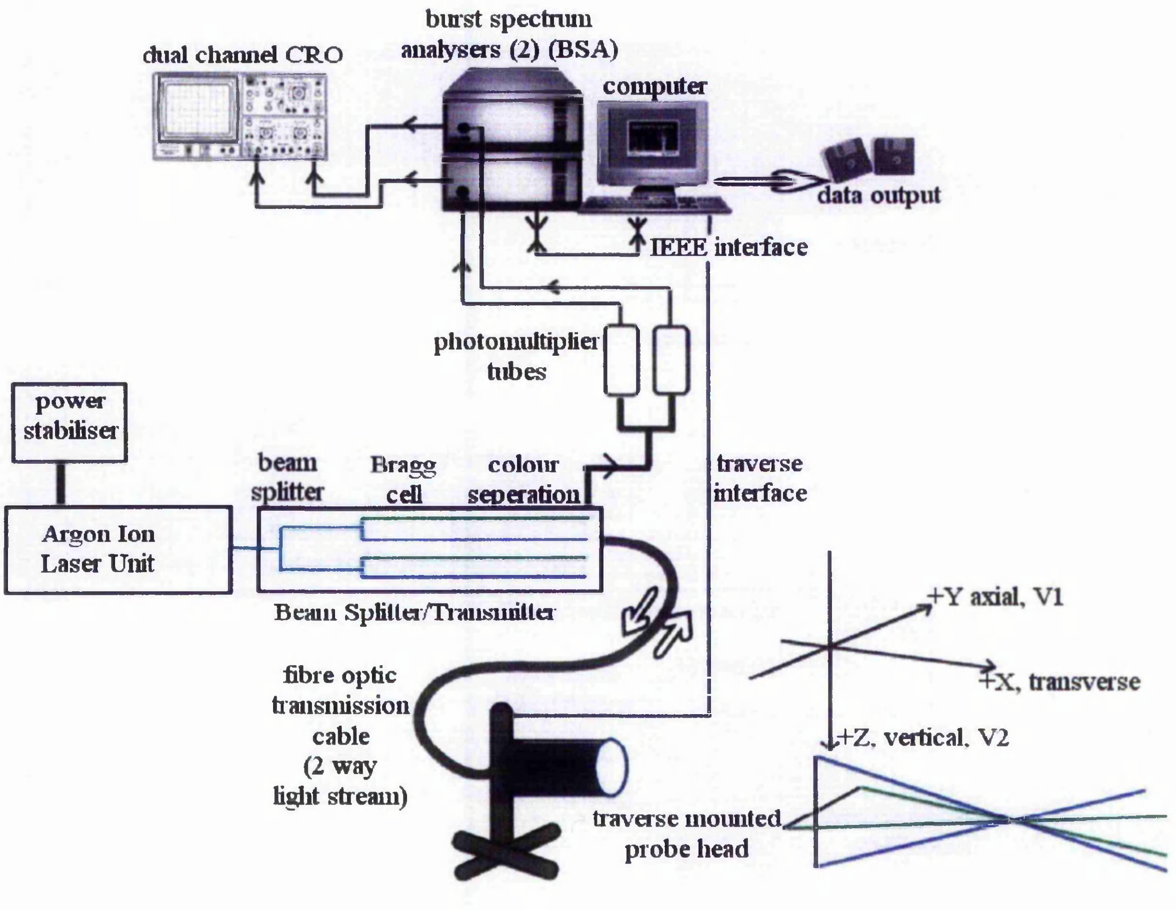

Figure 3-12 diagram of LDA equipment setup

3.8.4 ORIENTATION OF AAA GEOMETRY

For a better understanding of the data presented here this section will document the manner and geometric planes in which the data was collected. Figure 3-13 shows a representation of the aneurysmal geometry as studied.

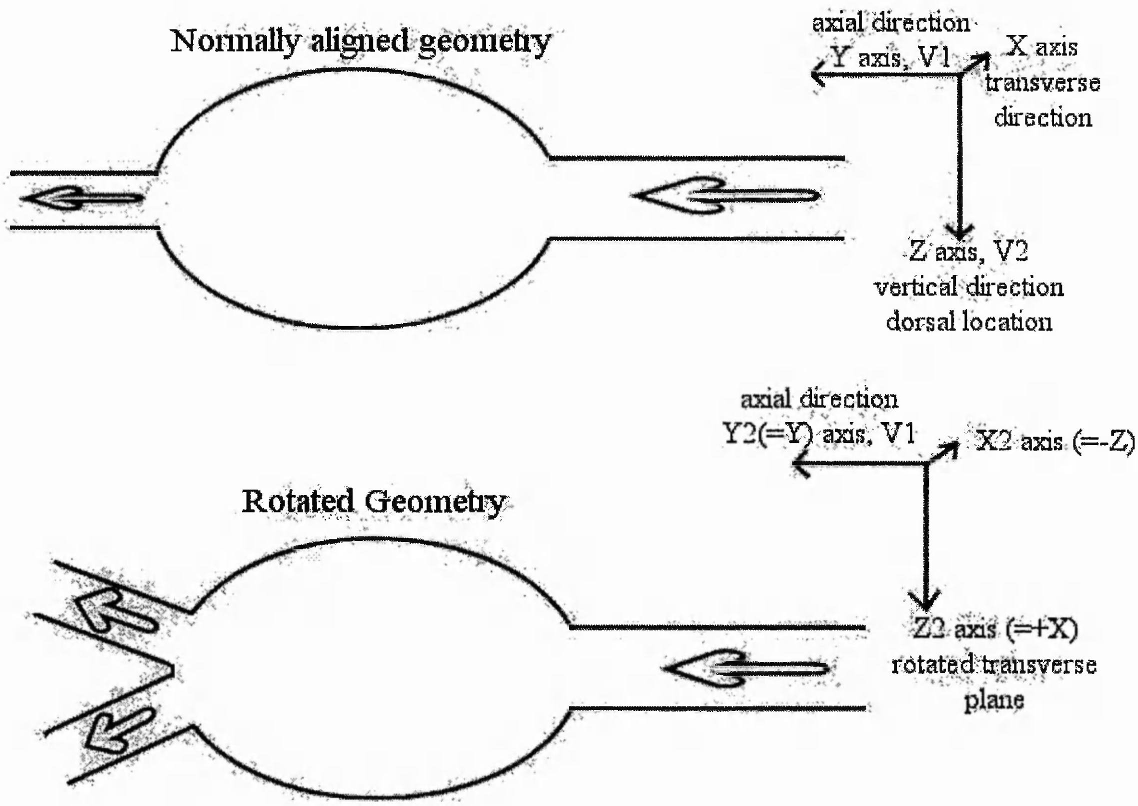

Figure 3-13 Geometry of AAA with respect to axis of measurement

The axes represent those used by the traverse mechanism where the positive movement in the y-axis displaced the measurement volume further downstream, distally with respect to the flow. The Z-axis moved the measurement volume vertically downwards, towards what would be the dorsal area of the body. The X-axis was in the same plane as those of the laser beams and was linked to a transverse movement across the AAA. Using the LDV system only two components of velocity could be measured at any one time.

BSA1 and hence, V1 was bound to the Y-axis in both rotations. However, only one non-axial velocity component could be measured at any one time. In this instance data from BSA2 V2 was linked to the positive Z-axis. A positive V2 velocity corresponded to a movement of particles through the measurement volume towards the dorsal side of the geometry. However, this leaves velocities in the X (transverse) direction un-measurable.

To this end measurements were also taken with a rotated geometry. The AAA model was rotated through 90° so that transverse velocities could be measured. In this manner the Z1 axis (dorsal direction) became the new X-axis, labelled here as X_2.

Positive movement on the Z2 axis would correspond to movement on the X-axis pre-rotation. In this new rotation transverse velocities could then be measured as V2 so that the full three-dimensionality of the flow could then be quantitatively surveyed.

Normal Alignment	Rotated Alignment
Y measuring axial V1	Y2 measuring axial V1
X not measuring	Z2 measuring transverse V2
Z measuring dorsal V2	X2 not measuring

Table 3-2 showing normal and rotated axes and their measurement capabilities

Of course it was necessary to compensate for any traverse motion on the X-axes (laterally) on the transverse axis when moving into the model. A correction was applied for the true displacement of the measurement volume.

It is also worth noting that X2 axis (horizontal displacement when the geometry was rotated) corresponded to an axis previously occupied by the Z (vertical axis). However, where positive Z1 moved the probe towards the dorsal side of the model, a negative X2 had the same affect in the rotated geometry.

3.8.5 LASER DISPLACEMENT CORRECTION DUE TO REFRACTIVE CHANGES

Due to the refractive matching of the silicone elastomer model to that of the blood analogue, small errors in the intersection of the two laser beams have been discounted. It was considered that the refractive difference between the two mediums was sufficiently low. The rig material was seen to have a refractive index of 1.413. The fluid was tailored to match this and was exhibited a refractive index within 1% of this value. Furthermore the beams always entered the rig via a plane, smooth surface to reduce such errors.

However, the gross change in the location of the beam intersection between the air and the rig/fluid could not be ignored and calculations to ascertain the new location of the measurement volume were carried out.

As light passes between one medium and another of differing refractive index the path of the laser beams will change. In terms of LDV this means that laser intersection is displaced from the desired location. It also means that traversing 10mm further into the model did not correspond to a 10mm displacement of the measurement volume. This was most clearly manifested when ascertaining the wall location of a vessel. Where the vessel had an internal diameter of 20mm the traverse took approximately 15mm of movement (normal to the exterior wall of the model) to cross the vessel.

This is shown in Figure 3-14.

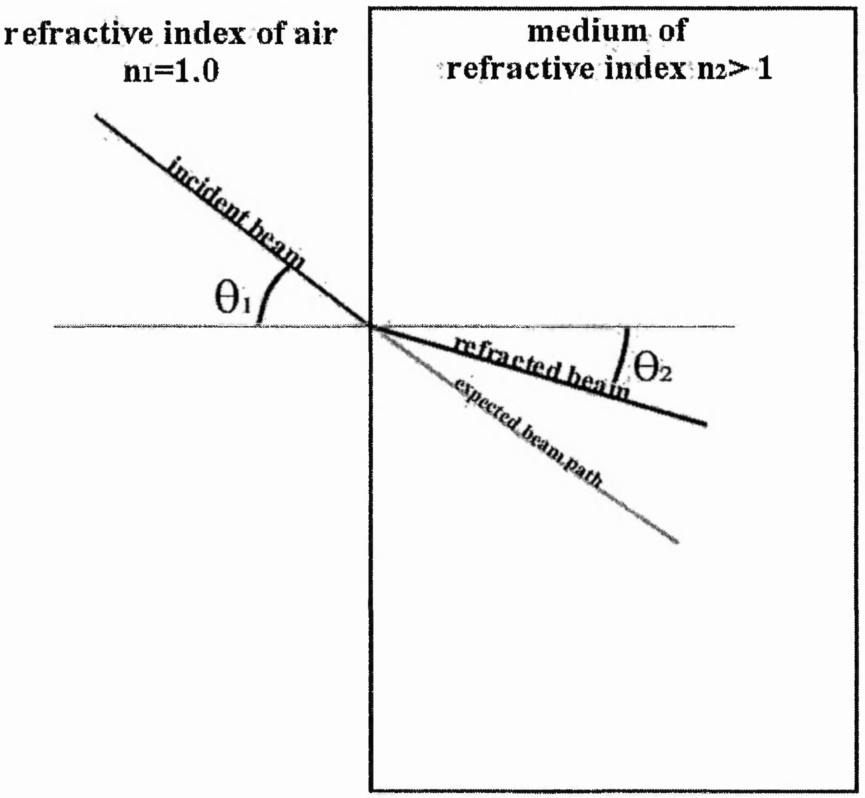

Figure 3-14 Diagram showing the effect of refractive index change as a beam passes through different media

Where a beam enters a medium of greater refractive index than the one it left, the angle of refraction (θ_2) is less than the angle of incidence (θ_1) to the ratio of,

$$n_1.\text{Sin}\ \theta_1 = n_2.\text{Sin}\ \theta_2$$

When considering air (nr = 1) this simplifies to;

$$\text{Sin}\ \theta_2 = \frac{\text{Sin}\ \theta_1}{n_2}$$

Where the medium of beam origin is air.

Continuing this logic to two laser beams entering and converging within a solid, the refracted angle is less than that of the angle of incidence and hence the convergence of the beams will take place further into the solid than anticipated.

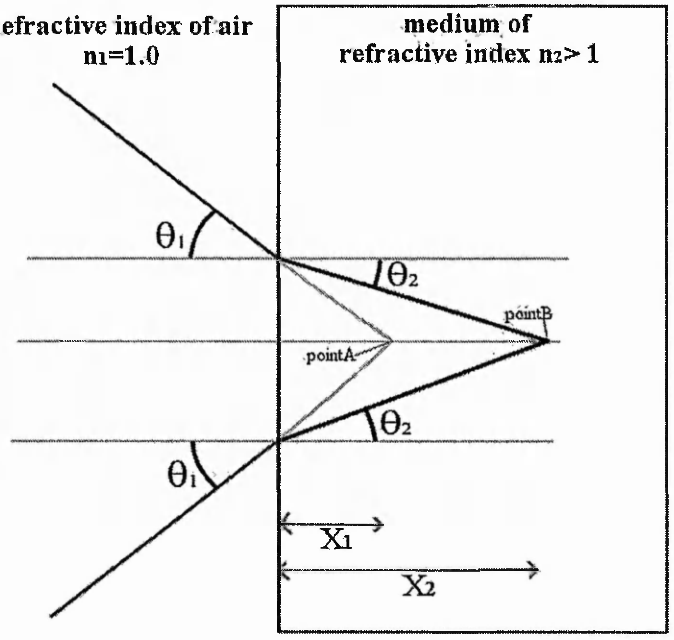

Figure 3-15 Diagram showing displacement of LDV measurement volume in a medium due to a change of refractive index

The displacement of the beams from their unrefracted position (Figure 3-15-point A) to the location where they would actually cross ((Figure 3-15-point B) is described by the displacement X_2-X_1 further into the solid.

Calculations were made to show the displacement from the norm when the lasers enter a region of gross refractive index change.

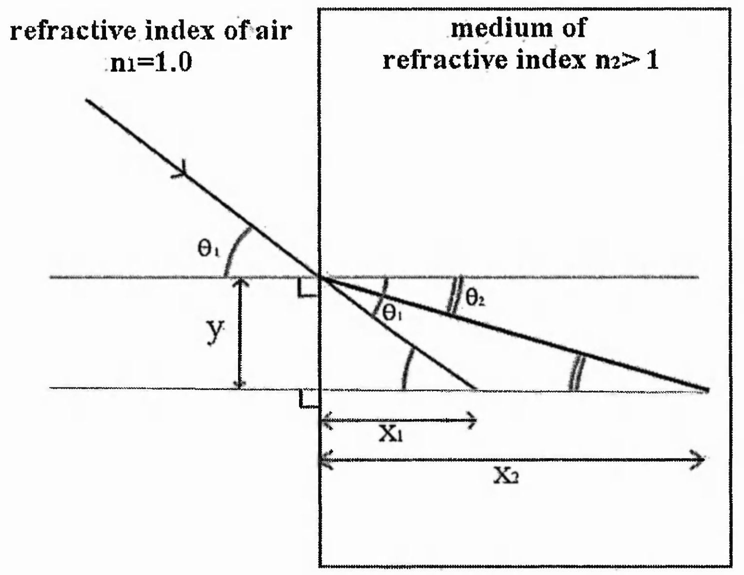

Where:

y is the half the beam separation

X_1 is the distance into the medium the beam is expected take to intersect the centre line without any change in medium or refraction.

X_2 is the displacement into the medium the beam will take before intersection with the centreline.

θ_1 and θ_2 are the angles of incidence and refractive respectively and $x_3 = x_2 - x_1$

Through trigonometry tan θ = y/x

$$\tan\theta = \frac{y}{x}$$

$$\therefore x_1 \tan\theta_1 = y = x_2 \tan\theta_2$$

and

$$x_2 = \frac{x_1 \tan\theta_1}{\tan\theta_2}$$

The refractive index of the medium, n_r=1.413

Plotting x_1 against x_2, the calculations conclude that there is a linear difference in the movement of the traverse and the movement of the beam intersection and hence the measurement volume. This difference is described in a proportional relationship with the ratio approximately equal to that of the refractive index of the rig medium that in this case was 1.413. This assumes that the source medium is air with an n_r of 1.00. The ratio does change with such parameters as beam width, intersection angle and focal length; however, these variables have a negligible effect on the displacement of the measurement volume in comparison with the refractive index.

The consequences of this are evident when traversing the beams through such a medium. Each 1mm movement into the solid translates as a 1.43mm movement in the direction of traverse. As such compensations were made with regards to the grid created in taking measurements within the rig.

The apparatus utilised in this experimental procedure provided excellent signal properties received and interpreted by the equipment. Both channels showed a high signal to noise ratio where short Doppler bursts were clearly distinguishable from the ambient signal. This was only possible if the PMT were receiving data from the measurement volume. Furthermore in the testing of the apparatus it was determined that coincidence measurements could be made. Such measurements protocols require that seeding particles pass through both measurement volumes in a limited time envelope. Coincidence measurements are used in the calculation of turbulence intensity data. That such data could be received showed intersection of measurement volumes from each set of beams.

3.9 Validation of Steady Flow Data Collection

Data was collected under varying conditions to access the validity of the measurement technique. Entrance and distal near-wall data was collected to ascertain the dependence of sample time and number of collected data samples upon the ensemble average results.

Time Dependence of Entrance Data

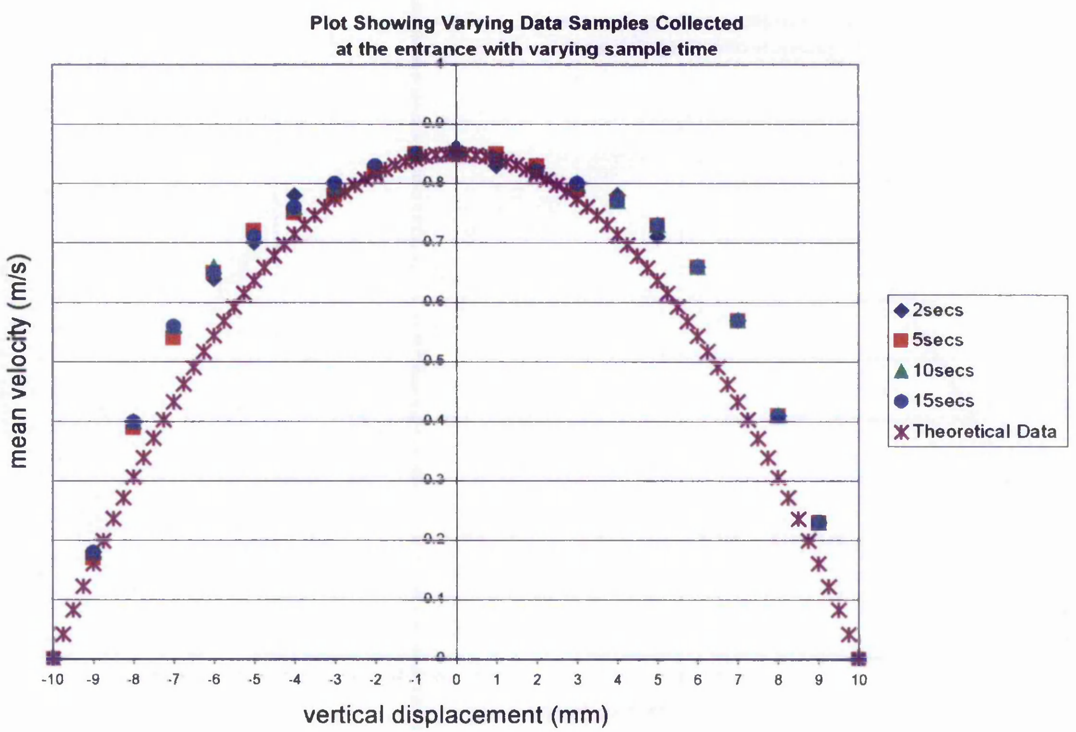

Figure 3-16 Scatter plot showing data taken from the inlet to the aneurysm model during steady flow

The data above shows the coincidence of all data points collected within the boundaries of reasonable error in the main stream of the flow. The theoretical data plot shows developed Poiseuille flow in the same region with the same peak velocity.

The flow recorded was not fully developed, although the curvature plot shows partially developed flow. Data was matched for peak velocity, not for flow rate. This was to exhibit the semi-developed nature of the experimental flow.

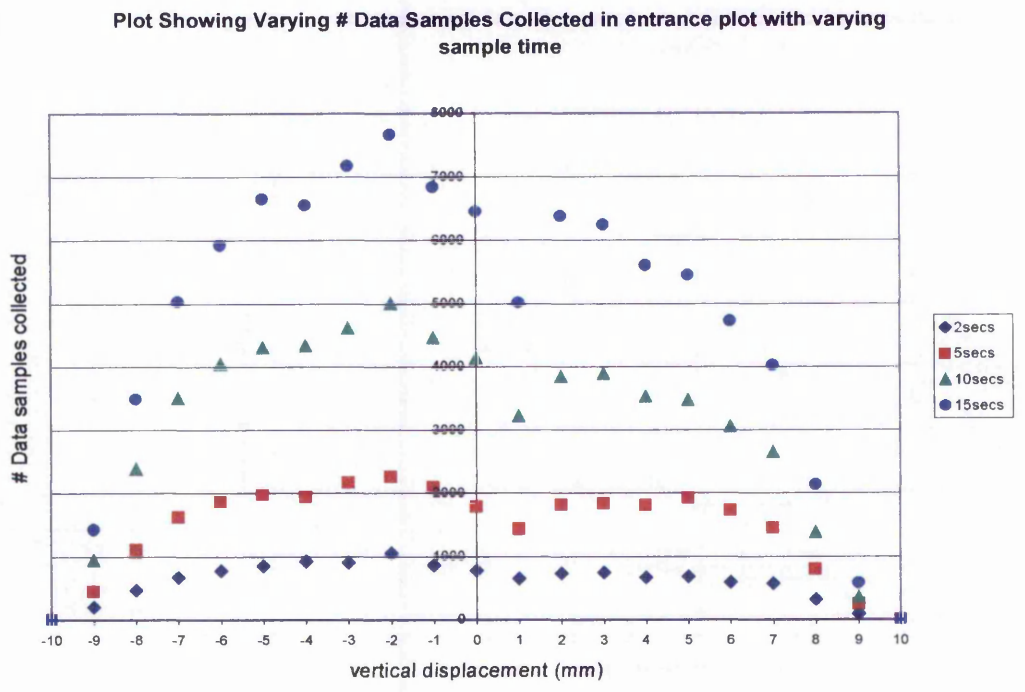

Figure 3-17 plot showing data # collect at the entrance with differing sample time

For the same region the number of data samples recorded was plotted above. In fast flowing regions it can be seen that even 5 second sample times gather sufficient data for confidence in the results. This was seen to be over 500 counts in all but within 2mm of the wall.

It can be seen from this data that in simple flows where the uncertainty and variation in the local flow rates is low, that a high-count rate is not required to provide quality data.

Downstream the flow was more complex. The mean velocities 85mm distal to the aneurysm entrance showed a peak core flow similar to that found at the inlet, but also reversed flow within the bulbous sides of the AAA.

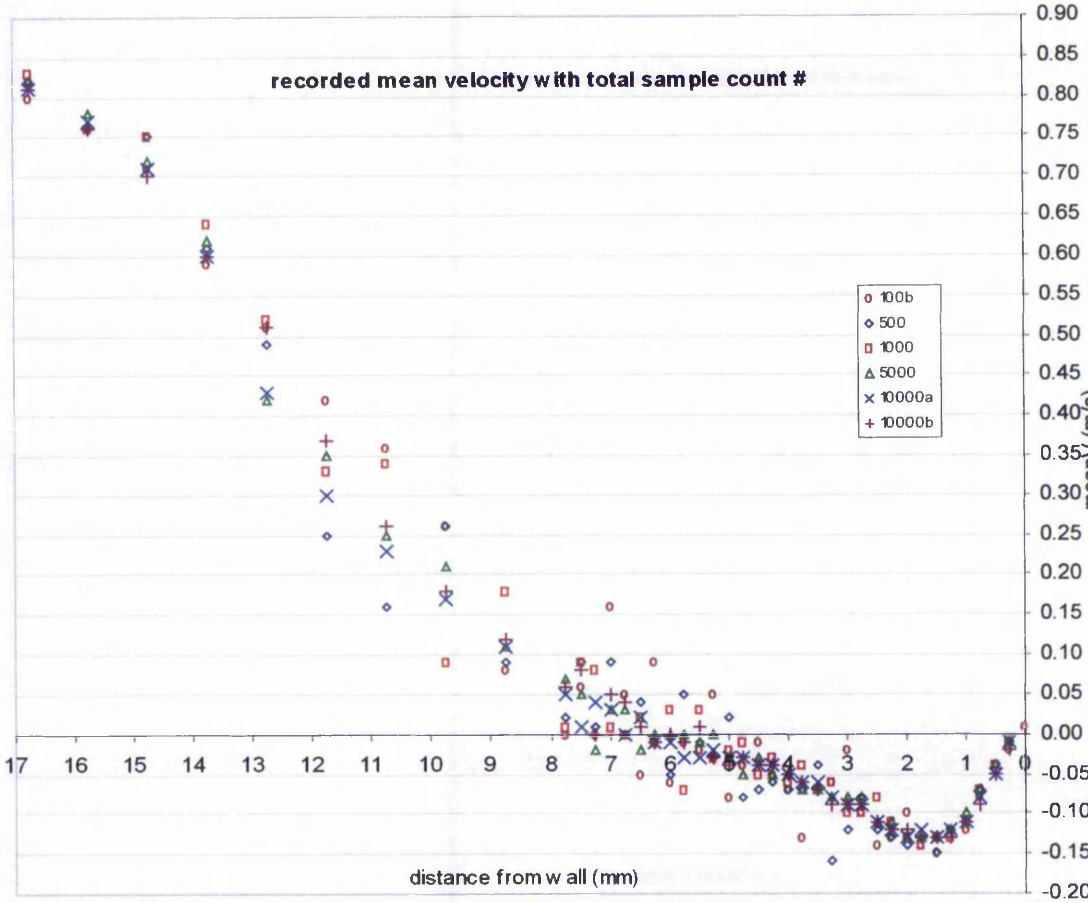

Figure 3-18 Scatter plot showing recorded velocity against no. data samples collected

It can be seen that there is a great scattering of data between different numbers of data samples collected. There are also three main regions of interest here.

The core velocity flow (14-19mm from the wall) can be seen to be clearly laminar and uncomplicated. 100 samples is enough to match the velocity readings taken by the 10,000 sample data points.

Between 2mm and 13mm from the wall however, the flow becomes less easily quantified. Taking 10,000a and 10,000b (identical consecutive runs) as the datum it is shown that there is considerable scatter in the lower numbers of data samples collected. Even at this level of samples taken (which drops to 300-500 samples close to the wall) it can be seen that there is great uncertainty in the flow in the recirculation with oscillations of recorded velocity especially about the point of inflection. However, the main steam velocities and those very close to the wall were highly quantifiable.

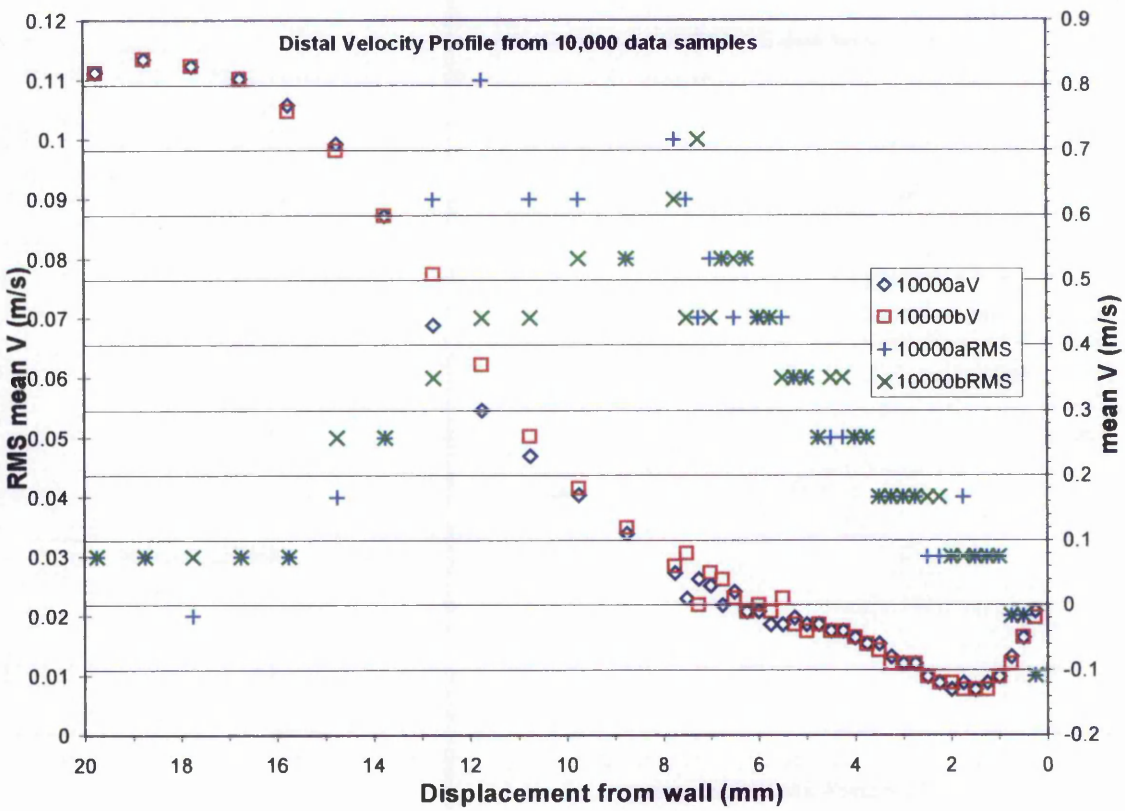

Figure 3-19 Velocity profile 85m distal to the entrance of the AAA

Due to the errors and low flow rates encountered near the wall distally within the aneurysm it was decided against taking time-constrained data samples.

1000 samples in the peak flow where the RMS of the mean velocity was very low provided adequate data. However, closer to the wall, the data rates were much lower. This was due to several factors. The low velocity (especially where the chart passes through a point of inflection) meant that less seeding would pass through the measurement volume. Furthermore, noise due to the proximity of the wall might interfere with valid data collection. Therefore more data was required without an unnecessary excess of data in the centre stream. Therefore a study of sample number dependence was undertaken to show the accuracy of velocimetry results under varying flow conditions. This point 85mm into the aneurysm provided a suitable area of study, showing high peak flow, recirculation, velocity inflection and near wall shear stresses.

In the distal location of the AAA a large and dominating recirculation can be seen which caused flow reversal at the walls. From the above figures is can be seen that the near-wall velocities were highly linear until the flow becomes embroiled with the uncertain area leading back to the point of inflection in the velocity profile. This region contained an area of unaccountably uncertain velocities, even when sampled over many minutes and 10,000 data measurements are taken. The near wall velocities were sampled at points along the length of the aneurysm and it was shown that at points close to the wall a linear velocity was measured.

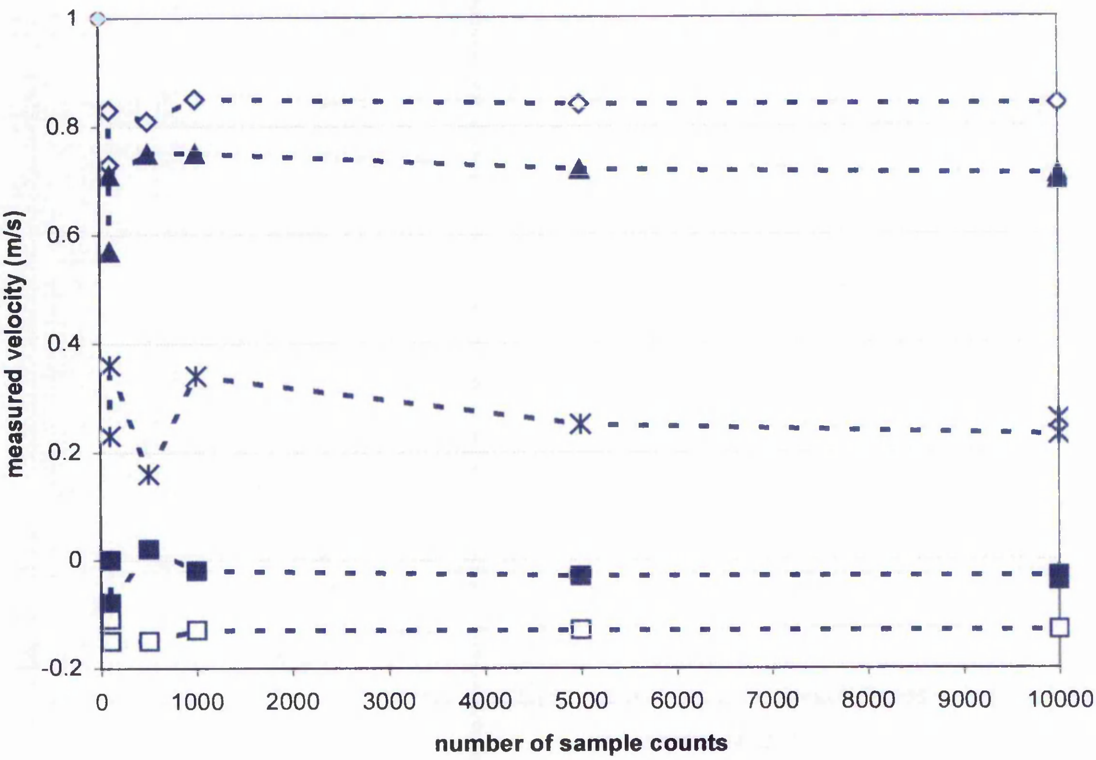

Figure 3-20 Graph showing velocity deviation with low sample rate where each series signifies a different measured velocity value.

The variation in measured velocity for different flow rates in the centre of the aneurysmal flow is shown in Figure 3-20. Both high velocities and also lower flow rates near the interior wall are plotted. It can clearly be seen that there is a variation in the velocity measured by the apparatus until a 500 or 1000 counts are taken. This, varies, however, as velocities in chaotic or turbulent flow may require a higher data count to ascertain their properties, as these data points will exhibit a higher RMS value in the data collected. The middle plot on Figure 3-20 is an example of one such velocity, measured in a region of uncertain flow. It can be seen that under conventional conditions, velocity can be measured to within 10% of the accurate value within 1000 counts.

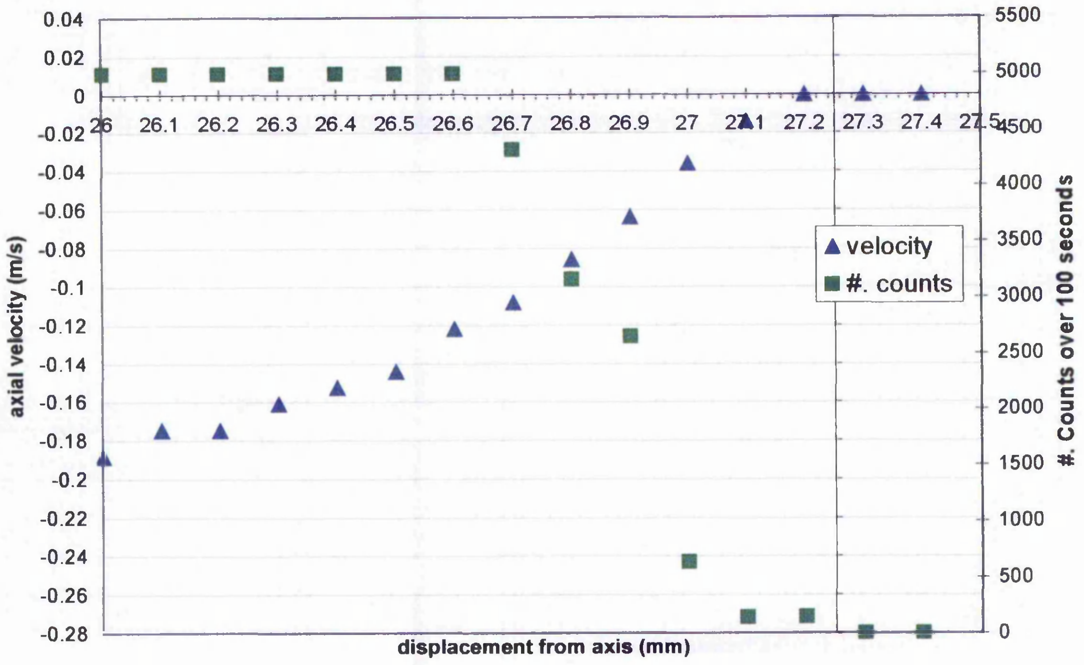

Figure 3-21 detailed near wall velocity profile 75mm distally into the AAA

The example above shows the near wall profile distally 75mm. The linearity of the profile breaks down after 0.5mm from the wall. However, within this boundary layer, in the steady flow section, a well-defined linear velocity gradient was observed from which it was possible to deduce the wall shear rate (WSR). In the above example is it possible to see the counts taken at each point. At a distance of 27.2mm a strong zero velocity count was observed. This represents a point where the measuring volume is only partially within the main flow. As such this point was discounted from the WSR calculation as being unreliable, due to the velocity bias that occurs within a measurement volume only partially exposed to the main flow.

When the measurement volume is located to some degree in the wall there is a marked overestimation of the velocity. This can be explained by visualising a measurement volume submerged into the wall to 50% of its width. The movement of particles through this volume generates the LDA signal. When fully exposed to the flow, the majority of particles are measured when they pass through the centre of the measurement volume. As this centreline is on the wall, the relative centre of the measurement volume becomes that of the remaining volume exposed to the flow. In this case where a velocity reading should read zero on the wall, it in fact reads a higher velocity component somewhat away from the wall. The results of this effect will vary considerably. Where the measurement volume is very large, this will have a detrimental effect on the accuracy of near wall measurements. This over estimation can either be corrected with compensation or the data from these points excluded from the resulting profiles. In the figure above the first data value was excluded. At a displacement of 27.2mm it can be seen that the data collected was of <200 samples with a strong zero reading, however, the RMS of the data collected was very high. As the measurement volume moves completely into the flow at 27.1mm the data rate does not increase to any degree, but there is a measured velocity and the RMS of the data drops considerably. Only data points collected from this point on into the flow were considered in the calculation of the WSR.

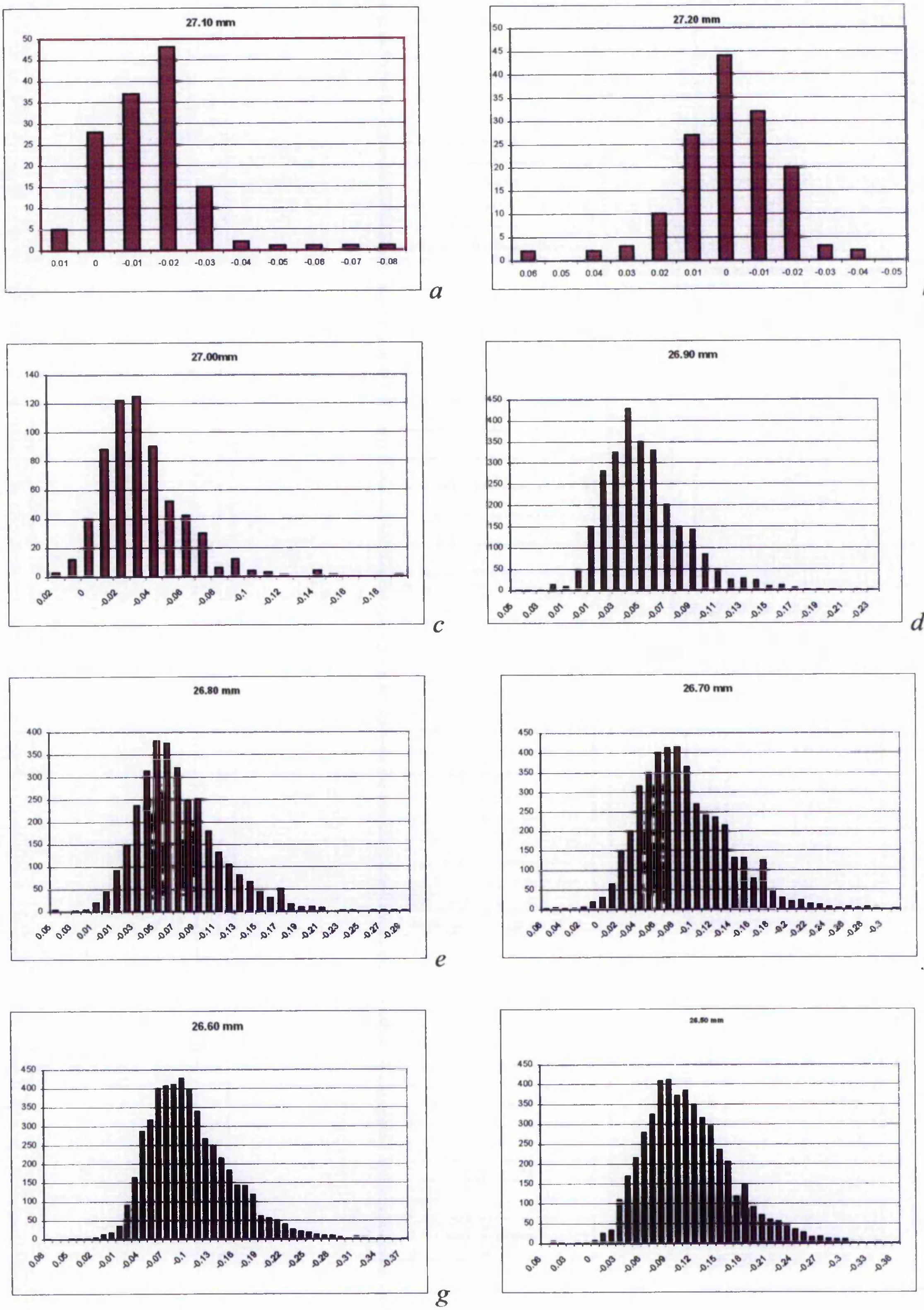

Figure 3-22 Histogram of collected velocity data showing frequency distribution of velocity (m/s) within 0.5mm of the wall which is located at ~27.20mm

The above histograms describe the distribution of data counts for near wall measurements when traversing from the wall. Figure 3-22a shows a low count rate that seems to have a zero velocity peak superimposed upon it throwing the centre of the distribution to one side against the trend of the other graphs. Any additional wall noise seen in Figure 3-22b shows a strong zero velocity reading, however, this was considered to be only a marginal bias to the shape of the histogram. At 200-500μm from the wall (histograms shown in Figure 3-22d-h) the basic shape of the histograms can been and become more resolute with the increasing data count of 5000 as seen in Figure 3-22g and h (Figure 3-22d-h contain more than 2500 data points).

The initial point A showed a high RMS in the recorded velocity values due to near-wall interference.

3.10 Validation Pulsatile Flow Data Collection

Due to the time dependent nature of the pulsatile flow, there were many issues to be considered before data could be collected as well as limitations in the temporal resolution and data acquisition limit of the hardware/software utilised in this investigation.

Firstly due to the limitations of software associated with the data collection and the volume of data at different points that needed to be acquired it was decided to cap the data at each collection point. A maximum of 10,000 counts, for each velocity channel (BSA1 and BSA2), with a maximum temporal window of 20 seconds was used for the collection of bulk flow data. This constituted over 23 pulsatile cycles in the areas of low count rate and complex flow. In the positions of high flow rate the number of pulses represented in the data was decreased, however, from data collected in the scope of this project the number of data counts was considered sufficient to represent the high-speed flow. Due to the very nature of this method of data collection regions of low flow rate, recirculation and uncertainty were more cautiously monitored.

The Dantec software handled the allocation and averaging of the data into usable time bins and the resultant averages for each time phase was output to a text file for each data point collected. The selection of time bins used was something that merited careful consideration.

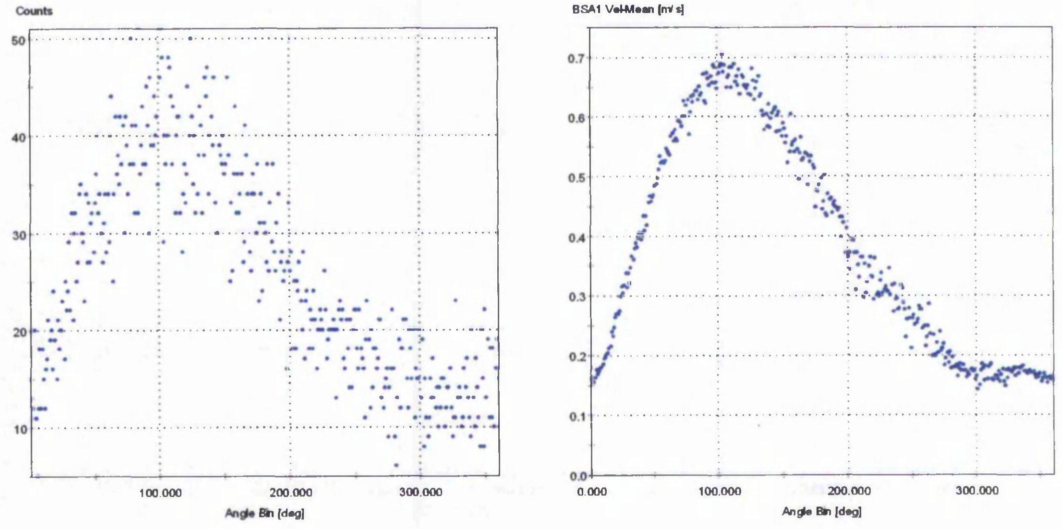

Figure 3-23 Pulse velocity waveform described into 360 time bins

Above is a graph of the raw data collected over 5 cycles (high flow rate at the entrance centreline). The graph represents 10,000 counts of data collection. The software naturally parses the data collected into a circular re-occurring form subdividing the time between reset pulses (active at the commencement of each pulse wave) into a maximum temporal resolution of 360°. Each of these sections of phase averaging is called an 'angle bin'. In the collection of time dependant data it is important to recognise the bearing this resolution has on the collection of data.

Data was required from 4 points within the flow cycle. These included both systolic and diastolic points of flow. It can be clearly seen from the above figure that taking a time bin from the point of peak systolic flow rate would give not only an inadequate rate at that point of merely 50 data counts but, due to any timing lag in the mechanics of the reset pulse, may not be accurately representative of the point of peak systole. To this end a balance was struck between temporal resolution and data rate at each point along the pulse.

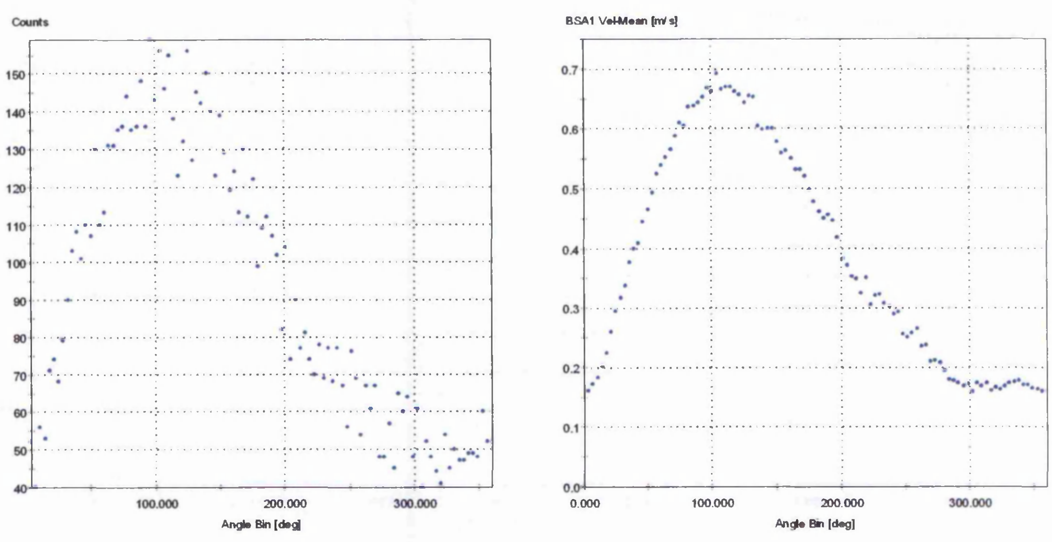

Figure 3-24 Pulse velocity waveform described into 100 time bins

With 100 angle bins the waveform is still accurately described although the data-rate in each bin is too low for the validated portrayal of the velocity.

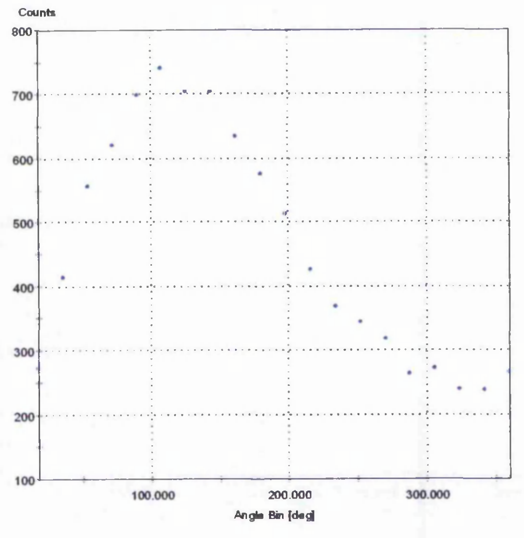

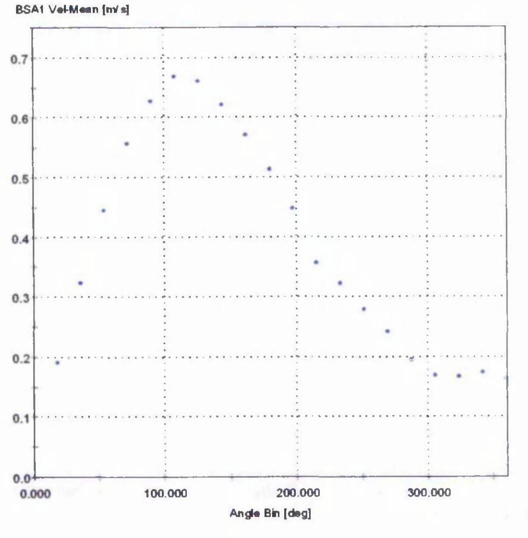

Figure 3-25 Pulse velocity waveform described into 20 time bins

Dropping the number of bins considerably, to that of 20, still enabled the waveform to be represented. However, the data count at each point was respectable including a peak data count of 700+ during peak systole. 250 counts are maintained throughout each point of the cycle. Decreasing the number of angle bins from the 20 represented here was considered both unnecessary to further increase data count and also detrimental to the representation of the pulsatile waveform.

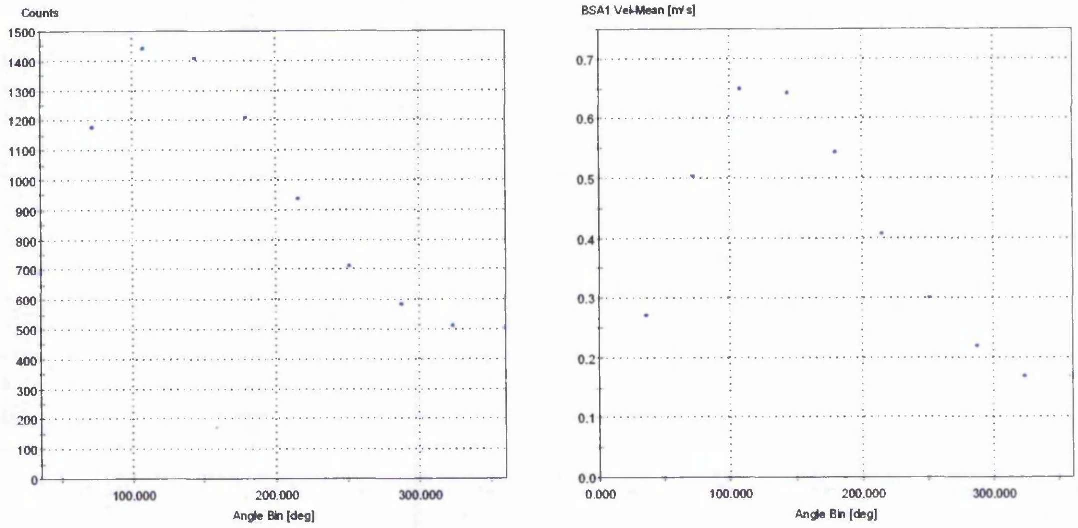

Figure 3-26 Pulse velocity waveform described into 10 time bins

As an example Figure 3-26 is included to show the limits of decreasing the temporal resolution of the angle bins. With only 10 time frames, the data represented in each angle bin is respectably high, however, the waveform has lost some of the characteristics seen in the other graphs. The entrance and exit velocities are considerably mismatched, and the peak systolic characteristics of the wave have been flattened to produce a less marked peak velocity.

As such to maintain both data integrity and accurate representation of the data flow, a total of 20 angle bins was used in the processing of the flow data.

3.11 Representation of the Pulsatile Flow

To economise the amount of data handling, velocity readings from 6 angle bins were collected in the pulsatile studies to represent stages of the flow phase. These were not distributed evenly throughout the pulsatile cycle but chosen to represent characteristic phases within the velocity waveform.

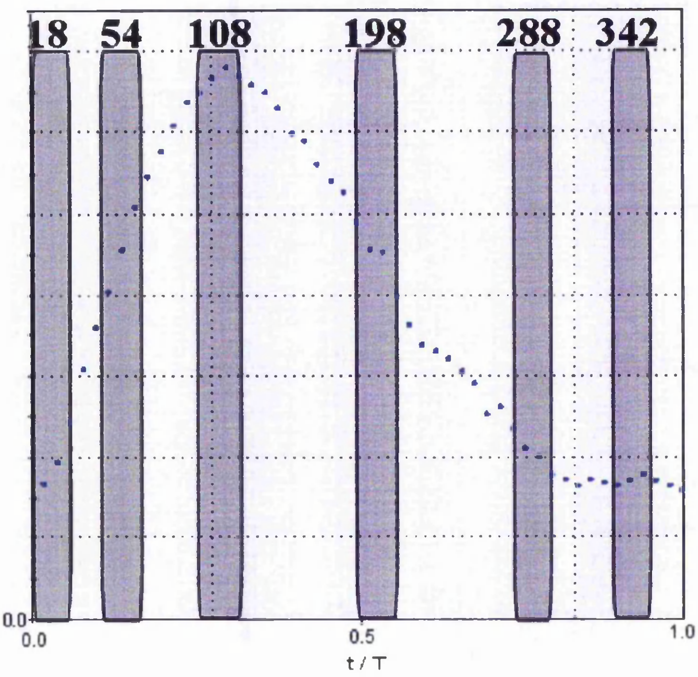

Figure 3-27 Distribution of time bins utilised in the acquisition of data

The angle bins used were 18, 54, 108, 198, 288 and 342 where 360 degrees of the cycle was divided into 20 discrete angle bins. Each represented data acquired within the previous 20th of the cycle and as such data was collected and presented from:

- the commencement of systole
- mid-acceleration of the flow
- peak systolic flow
- mid-flow deceleration
- mid-diastole where deceleration had ceased
- the 'resting' period of the pulsatile waveform

From these a suitable representation of the pulsatile flow cycle was presented and discussed.

3.12 Calculation of Wall Shear Rate

Wall shear rate (WSRs) were used to assess shearing effect of fluid flowing against the wall within the distal region of the aneurysm. The measurement of these forces was carried out by the employment of near-wall LDV measurements and subsequent analysis of the data results.

The measurement of WSRs has been considered in literature (Fatemi, 1994., Rowe, 1999) however, due to the complexity of the wall boundary layer in this model a technique was applied to account for all eventualities. Firstly, it must be considered that the velocities measured here are considerably low and furthermore the lowest increment of measurement capable using the apparatus used was 0.01m/s. The use of such a resolution necessitated changes in the methodologies employed. No-slip conditions were assumed to occur at the wall and through examination of the near wall boundary profiles it was demonstrated that the boundary layer examined in these experiments occurred linearly within the first 1mm of the wall.

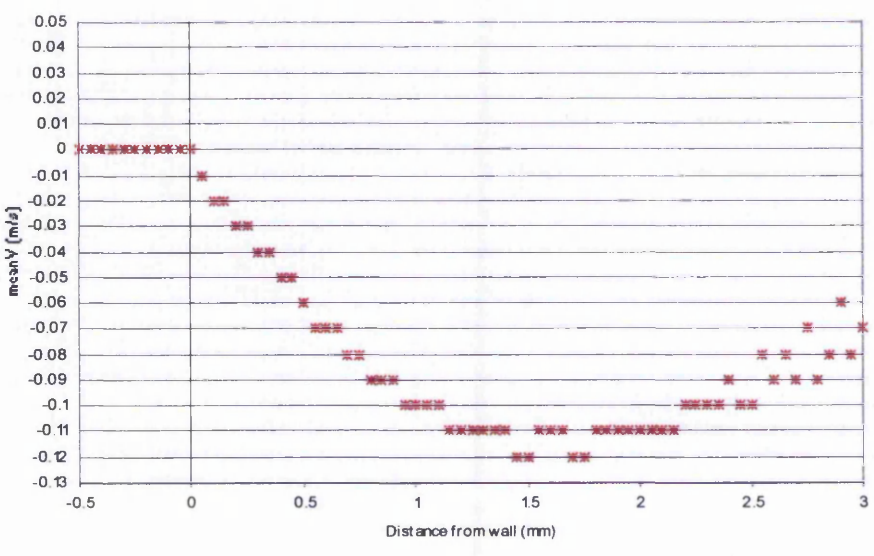

Figure 3-28 Example of near wall boundary layer velocity

The near-wall velocities shown in the above figure indicate flow reversal. This is due to the sample profile shown being taken distally within the aneurysm near a centre of recirculation. It was deemed suitable to demonstrate WSR derivation at this point, as this is the region of interest within the aneurysm. The use of equations to calculate these boundary layers would give erroneous results under these circumstances as they assume fully developed flow and zero wall curvature.

Figure 3-28 clearly demonstrates the linearity of the boundary layer within 1mm of the wall. However, it is also seen that due to the 0.01m/s resolution of the LDV apparatus, that adjacent data points often share the same value, although a linear progression of velocity is assumed and indicated by the shape of the graph.

Spatial resolutions of the traverse mechanism were commendably small (12.5 and 6.5μm in the horizontal and vertical axis respectively). However, the uncertainty involved in incremental measurements at this level was unknown. The measurement volume of the LDV probe was calculated to have minimum cross-sectional dimensions of 250μm, and the portion of this observed by the apparatus was considerably smaller, in the region of 60μm (due to the 'pin-hole' size). In previous literature methodologies took pains to measure velocities at increments of 25μm from the wall (Rowe, 1999). However, it is clear in the above example that several data points taken within the same 100μm region near the wall would potentially exhibit the same measured velocity. Furthermore, errors due to the proximity of the wall such as refection and the submersion of the measurement volume in the wall material decrease the use of this technique and facilitate the commencement of measurements at a defined distance from the wall, which implies detailed knowledge of the probe location. Under pulsatile conditions this was seen to be unfeasible due to minor wall distension occurring due to pressure changes. As such measurements were taken extending from within the vessel wall (through examination of the Doppler signal output) into the bulk of the flow in increments of 100μm.

Due to the curvature of the vessel wall it was considered erroneous to assume velocity solely in the direction of the longitudinal axis. As such velocity measurements were taken simultaneously in an axis matching that of the direction of wall curvature and a resultant velocity taken of the two components. This was considered essential in the assessment WSRs close to the outlet of the aneurysm.

From this data, individual velocity profiles were plotted and the gradient of the resulting graph plotted using the least-squares method. Zero values and those misrepresenting near-wall velocities due to submersion of the measurement volume into the wall, were discounted. Velocities showing non-linearity away from the wall were also removed, as it was assumed that these points had entered the bulk of the flow-field and no longer represented WSRs. In this method linear data points were collected numbering between 5 and 10 for each gradient and confidence was gained through the pursuit of R-squared values of 0.90+ that represented the suitability of the fitted gradient.

Under torsional conditions a second set of measurements was taken that represented the third vector of velocity not measured in the first instance. During rotation of the geometry measurements were repeated and the non-axial velocity component of the flow was included in the derived resultant in order to represent near wall velocity values.

3.13 Experimental Errors

The degree of error involved in the acquisition of these measurements varied depending upon the location of the measurement taken and the speed of the flow.

In bulk flow it was seen that measured velocities were typically 0.25-0.7m/s giving an error due to the maximum resolution of the LDV apparatus. This was 0.01m/s, producing errors in the range of 4% and decreasing to 1.5% in peak flow conditions.

Steady flow conditions were examined for repeatability and the steady flow pump output was measured continuously over a period of 2 hours. Axial velocities measured were seen to drop throughout this time but no more than 4% of the original flow rate.

Variation in the pump outlet was examined and repeatability of the pulsatile pump was considered suitable for the experiments. Waveform shape of the pulsatile output was highly regular with variation in peak velocity averaging of 8%.

Error in the reset pulse from the pump apparatus has been previously discussed as being 1.5%.

Therefore pulsatile measurements in the flow were taken with estimated errors of less than 10% in bulk flow regimes. Steady flow was considered to be subject to less error due to the more simple output of the pump. Such errors were seen to be less than 6%.

3.14 Critical Analysis of the Apparatus

As with any experimental apparatus used to provide data upon a subject so complex there are limitations of the equipment and materials utilised here.

The LDA data pool was limited by software to 125,000 samples before the buffer became full. Although this is sufficient for steady flow, when considering discrete time frames, in this case 20 time bins, the data cannot be distributed to those bins required for data collection. As such the natural maximum data produced per angle bin was 6250. This was found to be adequate to the job in hand, however, for areas of uncertainty this would have to be a consideration.

As this project concentrates upon the measurement of near wall data, it is important to understand the effects of the local wall upon the measurement volume, most especially when the measurement volume is partially submerged within the vessel medium. The author has made efforts to exclude data corrupted in this manner, however, the possibility of this occurring, especially on measurements taken diagonally through a wall curving in two planes cannot be ignored.

The vessel wall of the model was seen to be partially distensible, to within agreeable limits. The wall distended under pressure no more than 5% at its weakest point where *in vivo* vessel distension is seen to occur up to 10%. However, the distensible nature of an AAA is untested. Furthermore the distensibility of the wall was proportional to its thickness, which varied along the model. The only mitigating factor in these experiments is that such measurements were taken from within the wall traversing outwards, so that at any point of maximum pressure/distension would be taken into account. No fixed wall location was assumed to be maintained throughout the whole pulsatile cycle.

Critical to these experiments three-dimensional data was taken, however, this was taken through rotation of the whole apparatus. Some factors, such as gravity, cannot be maintained through such rotation. However, datums were used and controls were taken to assure the validity of the data and to minimise any variables that were not uniform. Demonstration of the small scale of these changes was undertaken and presented in this document.

The analogue fluid was designed around its optical properties. However, one primary variable not mimicked was the non-Newtonian behaviour of whole blood. It has been discussed in this work that Newtonian behaviour can be attributed to the blood analogue as a compromise when working in large arteries and at shear rates >100s^{-1}. However, some research has been carried out to contradict this assumption. It was considered valid to utilise these properties in the realm of experiments considering large arteries at this time.

3.15 Summary of Methodologies

This chapter has documented the design and commission of the apparatus used in this investigation and the experimental methodologies employed in the course of this research. The error involved in the collection data and the calculation of results derived from this data has also been discussed showing the experimental viability of research carried out within the scope of this project.

RESULTS: PRESENTATION AND DISCUSSION

4.1 Flow Field Results

The results presented here are show quantitative point velocity measurements throughout a three-dimensional geometry. To simplify the flow, measurements were taken in single planes through the model. Wall shear data was derived from similar data taken at high resolution near the model walls.

The velocity vector plots are presented in colour. This was due to the detail of the flow that would be lost in a plot showing scaled vector points. Linear displacements and dimensions were non-dimensionalised against the inlet diameter, d (20mm), and the velocities were non-dimensionalised against the peak inlet flow rate. All velocity vectors are scaled by colour so that the crucial direction component of the flow could be appreciated. Low velocity regions of stagnation or recirculation were considered to be less visible using alternate methods of plotting.

4.2 Steady Flow, Non-torsional Inlet Velocity Data

4.2.1 INLET PARAMETERS

Detailed below are the inlet flow conditions encountered in the experimental apparatus (Figure 4-1). True axisymmetric flow was not possible due to experimental fluctuations and imperfections in the rig; however, a generally semi-developed boundary condition was created and maintained for all the steady flow experiments with an Reynolds number of 4000 representing the peak flow seen in the pulsatile work.

The second plot (Figure 4-2) shows the inlet flow encountered when it was necessary to rotate the geometry. This is included to show the consistency between the two conditions. The formation of the central velocity core is not identical but maintains a trend suitable for the work. Peak velocities were maintained within between the two rotations to within 2.5%. The shape of the vertical and horizontal profiles was also similar in each case. It is worth noting at this point that the horizontal becomes the vertical due to the required rotation of the geometry in order to take the data in the direction of the third axis.

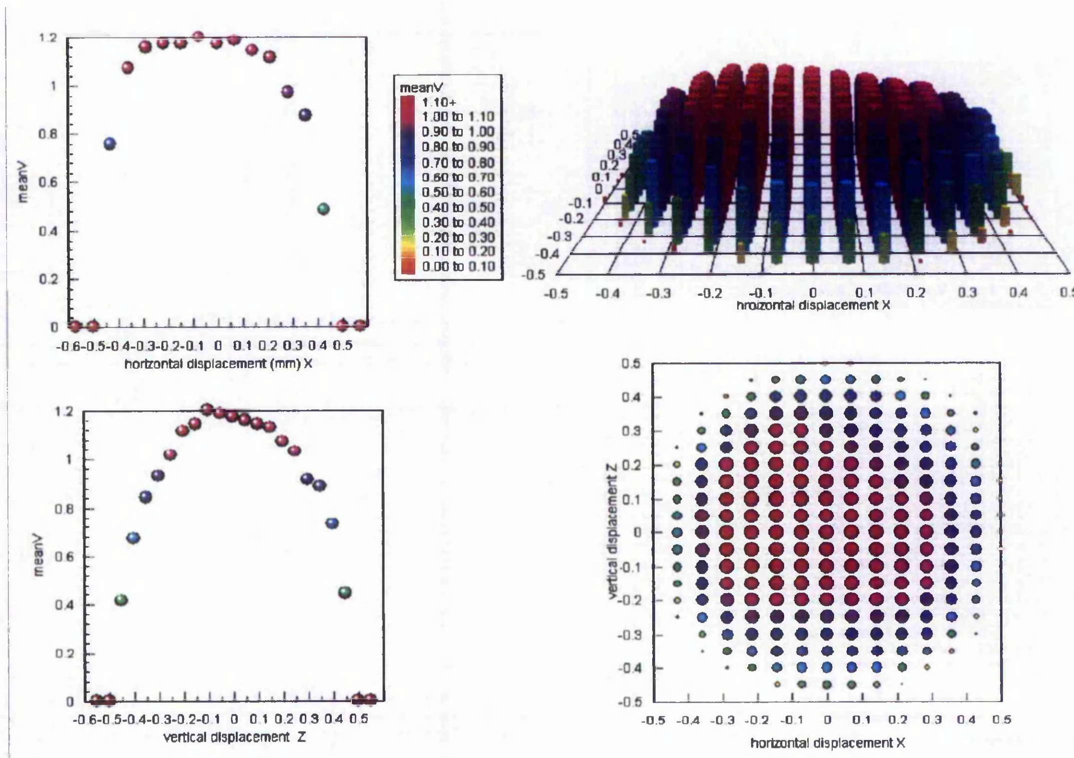

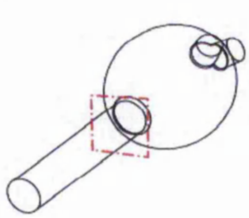

Figure 4-1 Plots showing steady flow, normal inlet boundary conditions

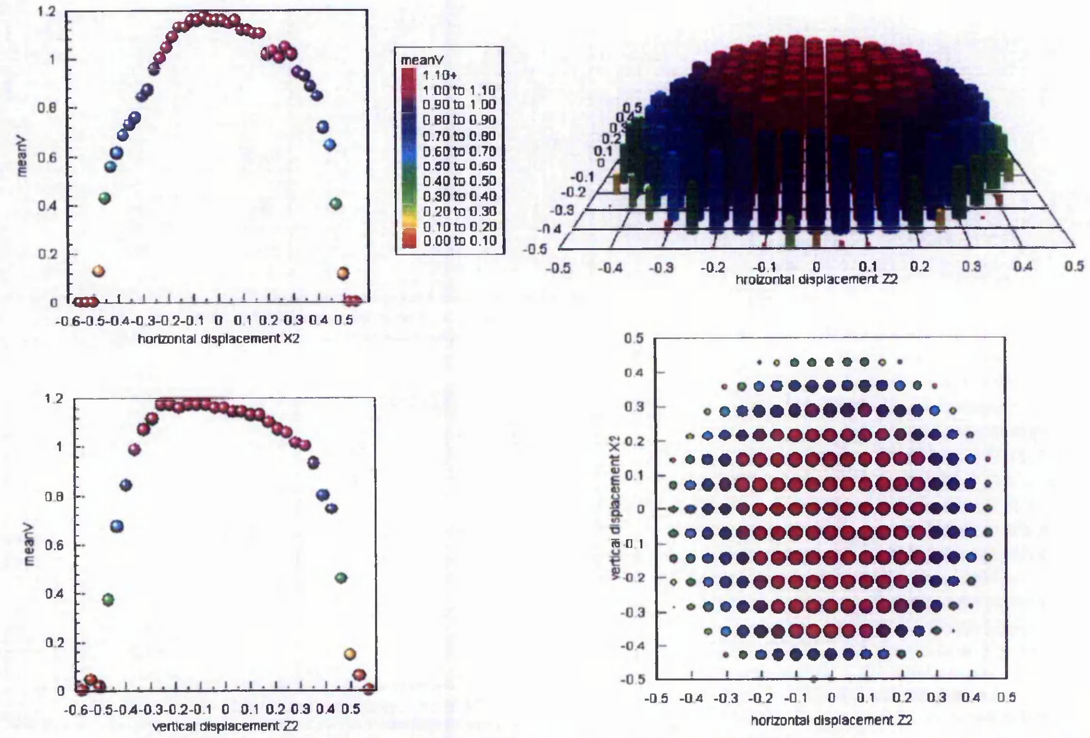

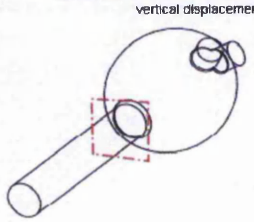

Figure 4-2 Plots showing steady flow rotated inlet boundary conditions

4.2.2 FULL FIELD VECTOR PLOT DATA

The vector plots show qualitative full-flow field velocity distributions throughout the model. Red/triangle data points with no magnitude show zero velocity data collected in the wall of the model and remain in the plot for completeness. They indicate the complete traverse grid used to map the flow and show both the shape of the aneurysm and the curve of the bulk flow that accommodates and follows the wall boundary.

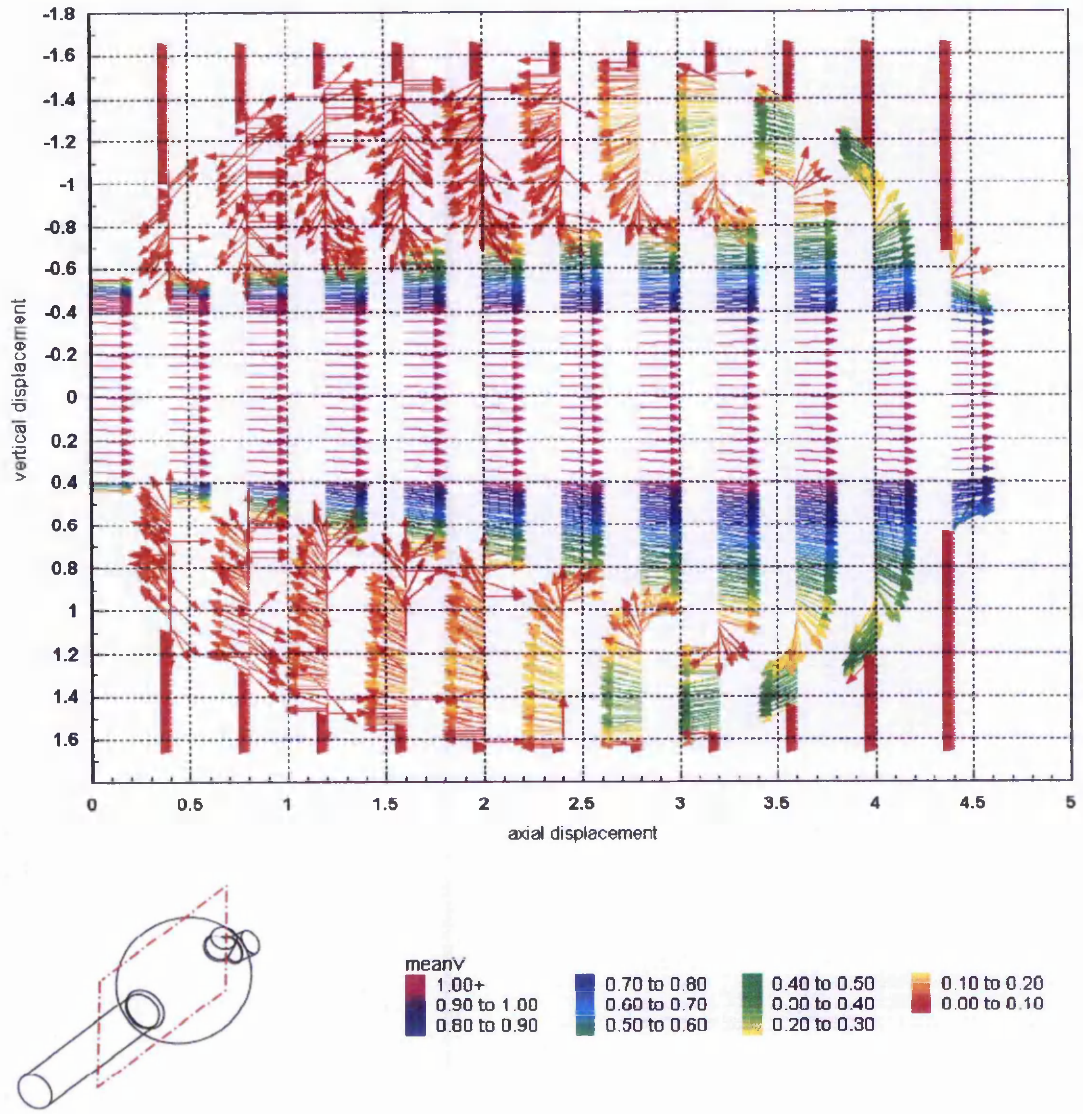

Figure 4-3 Full field velocity plot, non-torsional inlet-steady flow, vertical Y-Z plane

Figure 4-3 shows a vector plot describing a vertical plane through the flow field. The flow maintained a steady state once the flow field was fully developed.

The velocity core was maintained throughout the length of the aneurysmal dilatation and only minimal expansion of this maximal velocity was seen. Outside this central core rapid deceleration occurred due vessel expansion at entry into the aneurysm. This contributed to the expanded core impinging upon the distal wall of the aneurysm, which caused a reversal of flow along the wall of the AAA and a vortex ring to appear universally around the core flow. The flow was not perfectly symmetrical. This was due to imperfection in the uniformity of the inlet conditions. A marginally greater velocity in the upper section of the inlet caused a delayed deceleration of the flow in the upper quadrant of the geometry. In turn this caused the vortex seen to be generated further distally in the aneurysmal bulge. Proximal to the vortex ring was a further deceleration of flow leading to a region of disturbed and chaotic flow. In these areas velocities were very low and the oscillation of velocities measures very high. Flow from this region was also seen to feed back slowly into the main core. On the dorsal side of the AAA flow was less chaotic where the vortex was located more centrally in the bulge. In the upper half of the geometry the region of uncertain flow was considerably larger and less of this stagnant flow is returned to the core. From visual observation particles in the flow were seen to often become accelerated distally when coming into contact with the flow core. However, the acceleration was not complete and often such particles were fed back into the recirculation when approaching the vortex.

It can be surmised from this vector plot that more rapid flows decelerate to a region of recirculation more distally than flows caused by a lower entrance velocity and also that the vortex from the more rapid core leaves proximally a region of uncertainty. The more central vortex of the dorsal side of the AAA leaves less room for flow stagnation.

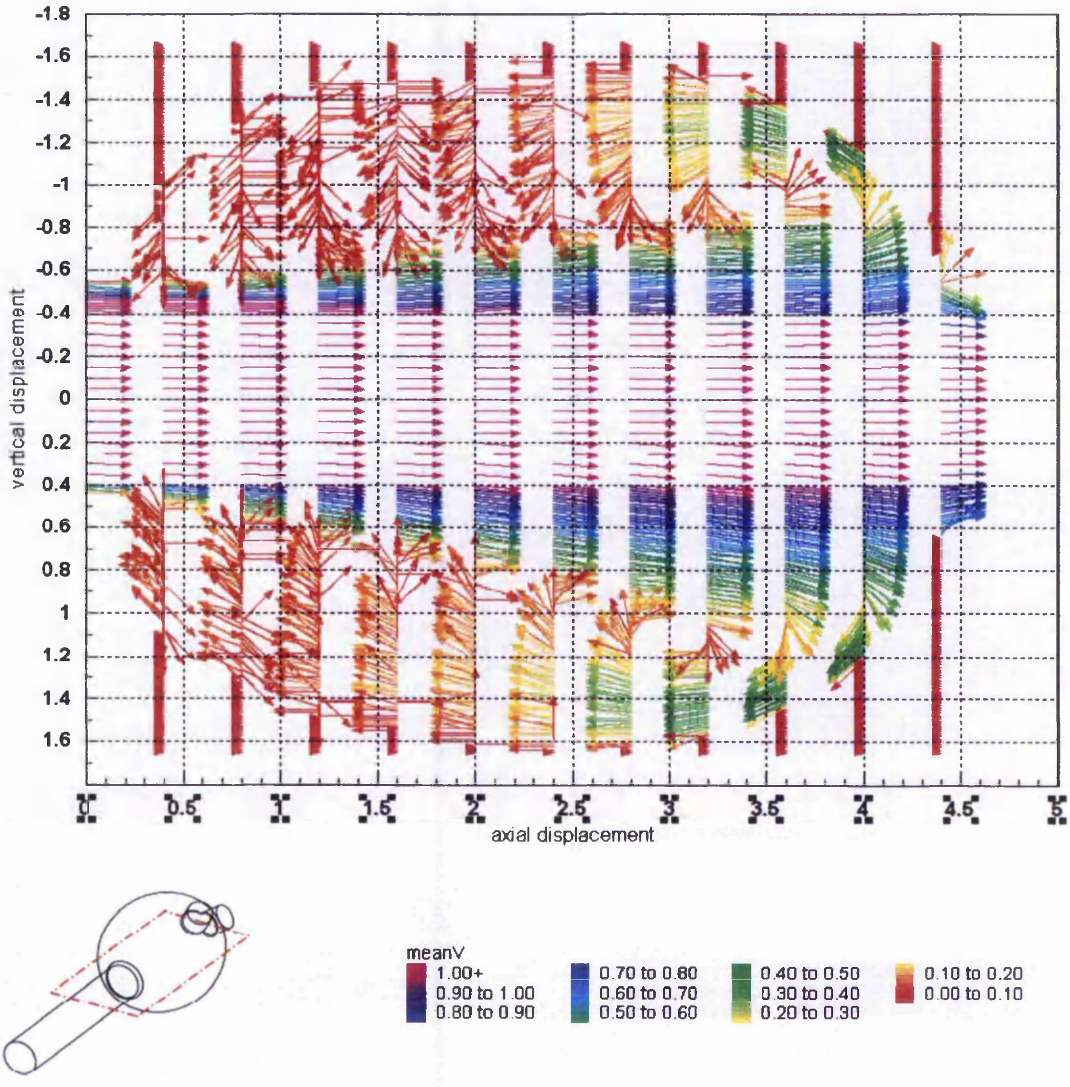

Figure 4-4 Full field velocity plot, non-torsional inlet-steady flow, horizontal X-Y plane

The vector plot above shows the mean velocity measured in the horizontal plane of the AAA. However, the geometry was rotated for these measurements so that appropriate velocity data could be taken. Through observation of flow visualisation carried out this formation of main flow and vortices was seen to be stable.

The ease of comparison between this and other studies, included below is a representation of Figure 4-4. However, such plots do not easily show recirculations and lack non-axial velocity directions.

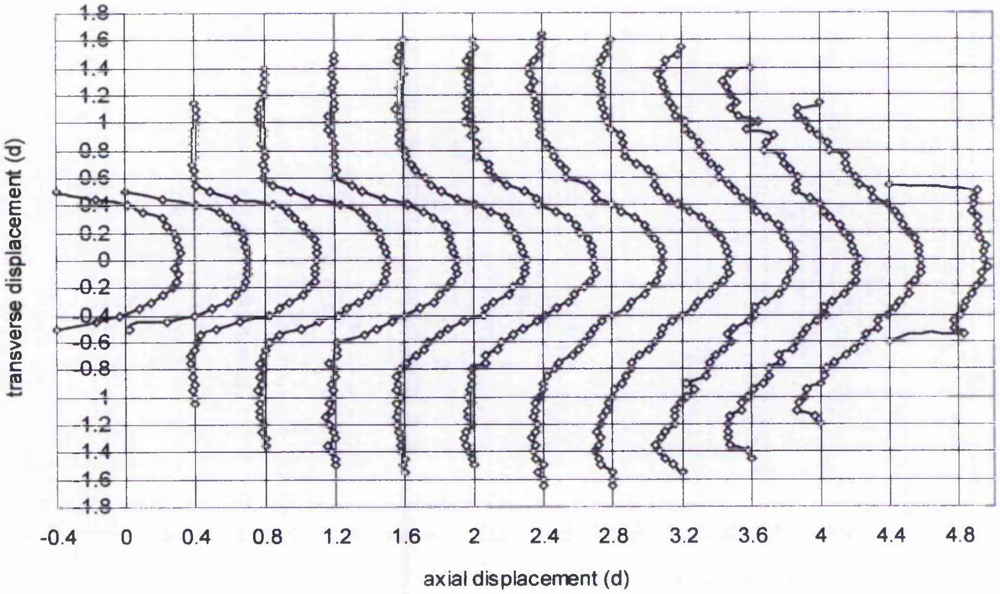

Figure 4-5 Plot showing axial velocity data in the horizontal plane

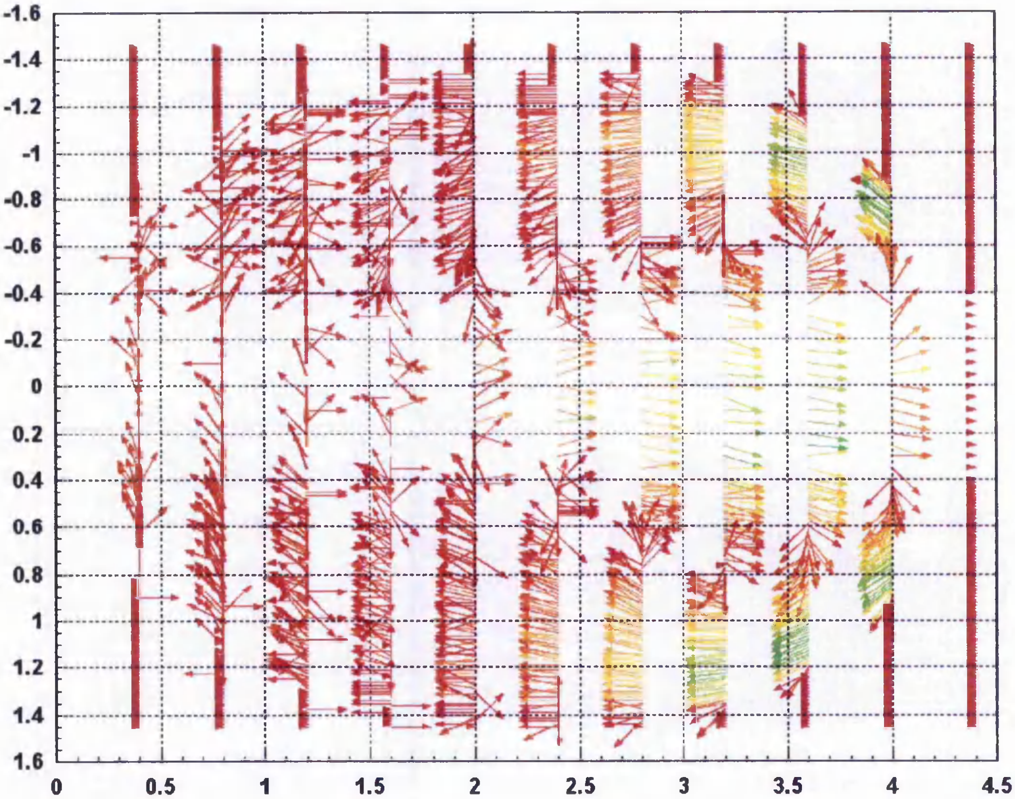

Figure 4-6 Offset velocity profile, non-torsional steady flow: +0.55d from central axis

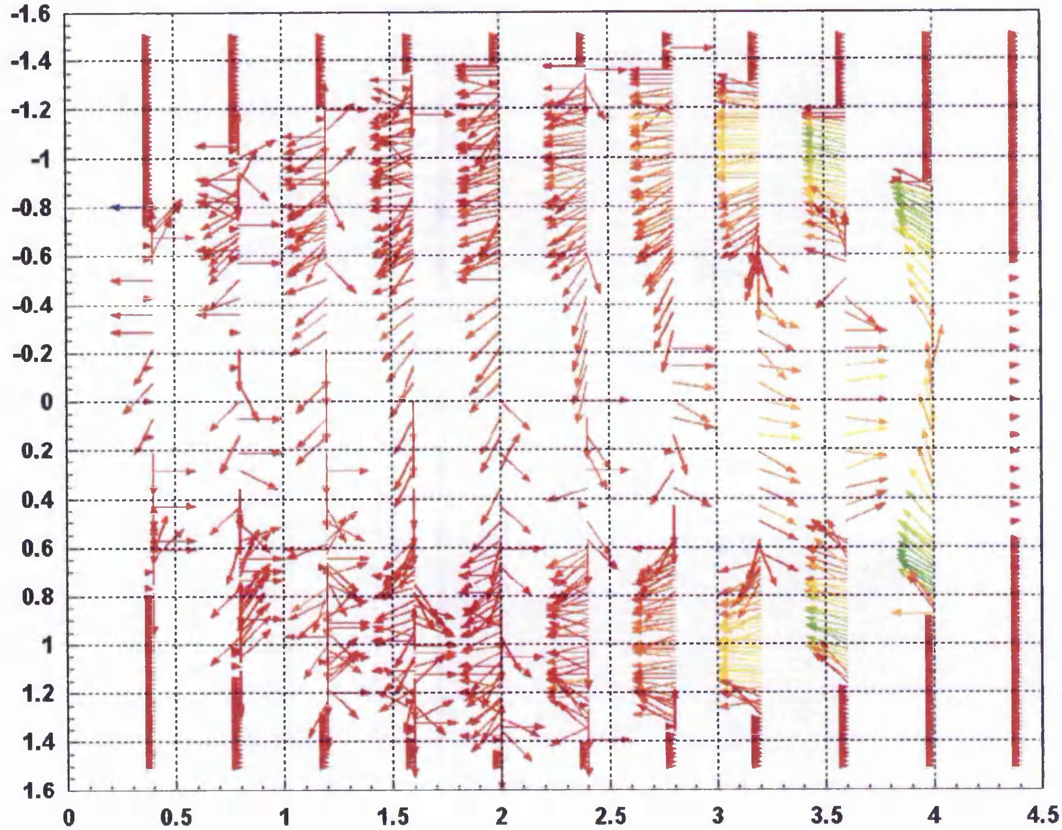

Figure 4-7 Offset velocity profile, non-torsional steady flow: -0.55d from central axis

Figure 4-6 and Figure 4-7 show flow fields taken from the conventional geometry rotation. The velocity core closely matched the radius of the inlet (1/2d).As such these plots show velocity flow fields either side of the main flow stream. Distal flow can be seen to be associated with the edge of the core flow, possessing a lower velocity than that seen in the central flow region. The proximal centreline flow region (0.5-2.5d details the random nature of the flow close to the inlet, upstream of the vortices. These velocity plots also exhibit both the symmetry of the flow and the stable halo of recirculation approximately 3.5d into the model.

4.3 Steady Flow, Torsional Inlet Velocity Data

4.3.1 INLET PARAMETERS

The torsional parameters of the flow were implemented due to the upstream geometry of the modelled aortic arch. Axial velocities were measured 5mm proximally to the inlet of the AAA to document the distribution of velocity across the entrance to the aneurysmal geometry. As documented, during the experimental investigation it was necessary to rotate the geometry (including the arctic arch) so that transverse velocities could be measured. To ascertain the effect of this rotation on the inlet flow parameters axial velocities were compared between the two conditions (Figure 4-8).

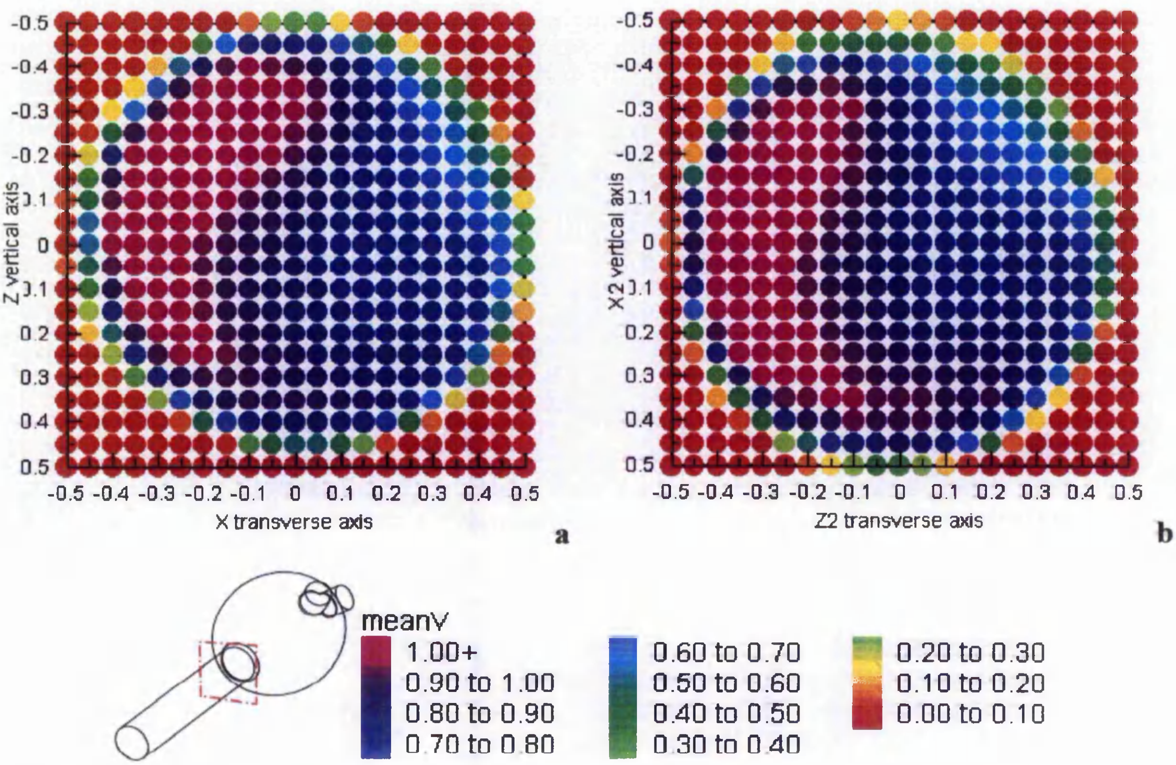

Figure 4-8 Plots showing the axial velocities measured at the normal and rotated steady-flow torsional inlets.

(Plot **a** being the normal and plot **b** showing the rotated inlet)

It can be seen that there is a strong correlation between the two boundary conditions with regards to the axial velocities. The peak velocities were out of alignment by no more than 6% and the peak velocities measured in each case were within 1.25%. From this confidence was given to the validity of comparing measurements taken under normal and rotated conditions.

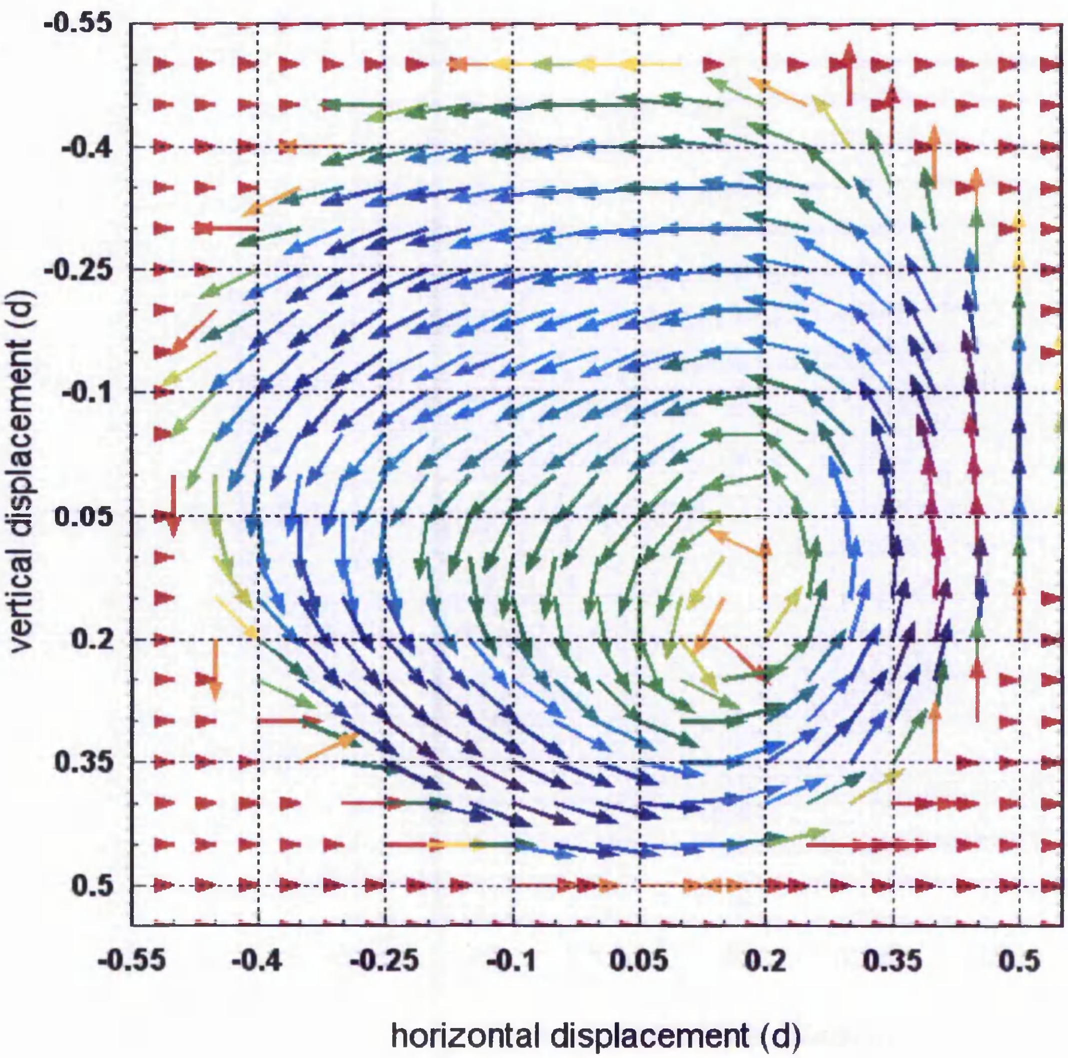

Figure 4-9 Vector plot showing rotational aspect of the steady torsional inlet

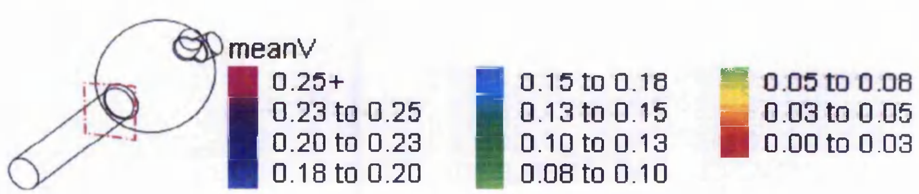

Due to the strong three-dimensionality of the inlet, transverse and dorsal velocities (during rotation and normal alignment of the geometry respectively) were measured and combined to show the torsion experienced by the fluid at inlet.

Figure 4-9 shows rotation dominating the entire of the inlet plane, the centre of which was offset from both horizontal and vertical centrelines. This was located towards the inside of the lateral plane and offset toward the top of the inlet, in favour of the direction in which the arch curves out of plane. The greatest rotational velocity was seen to be 25% of the maximum axial velocity and occurred in a region of relatively low axial flow.

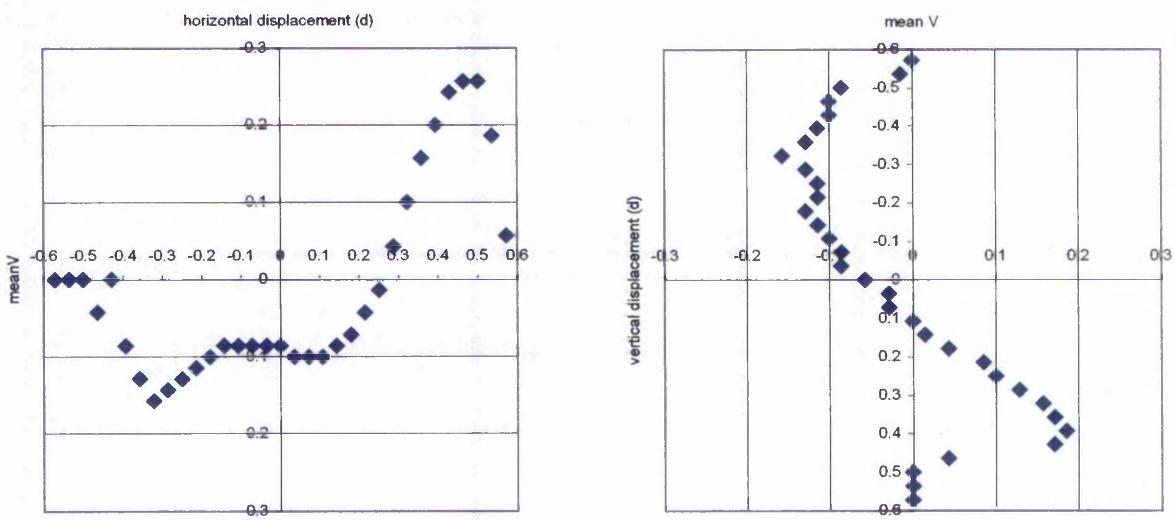

Figure 4-10 Plots showing axial rotation at the inlet in vertical and horizontal planes respectively

Figure 4-10 shows a relatively simple representation of the torsionality induced at the inlet. This is for purposes of comparison with the pulsatile representation of inlet boundary conditions (Section 4.5.1). It can be seen that peak velocities are offset from the origin of both axes and the rotation is highly asymmetrical.

4.3.2 FULL FIELD VECTOR PLOT DATA

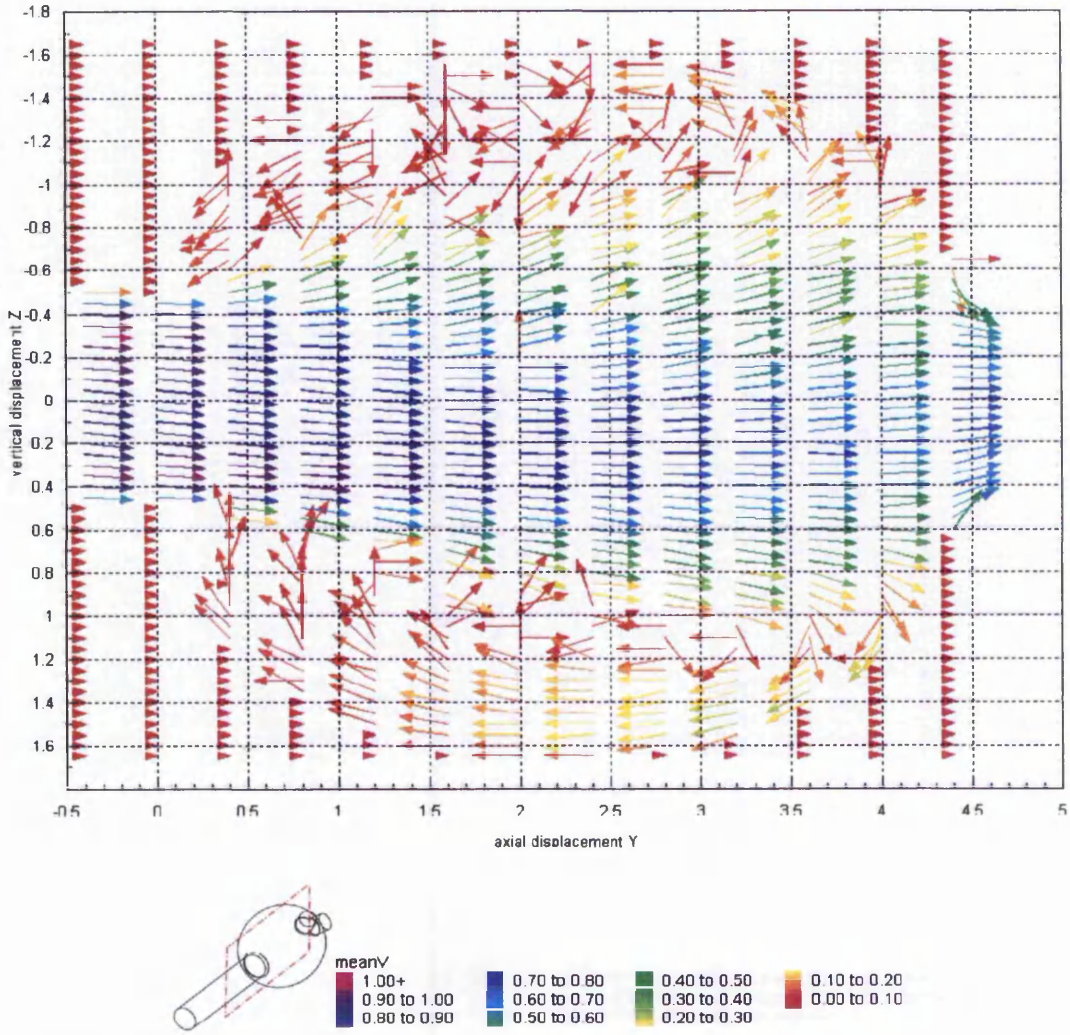

Figure 4-11 Full field velocity plot, torsional inlet-steady flow, vertical YZ plane

The vertical profile of the full field flow was clearly affected by the torsional aspect of the inlet. The phase of the rotation at the entrance to the AAA caused a deceleration in this plane and the jet flow was skewed to the dorsal side of the bulge. The velocity core was also greatly more dispersed than in the non-torsional inlet model, fanning out almost from the inlet to fill the aneurysmal bulge causing lower velocities. Also although the jet impinges on the distal wall of the aneurysm, the velocities at this point are also diminished. As physiologic aneurysms are rarely axisymmetric jet impingement would take place regardless of the upstream torsion.

The vortices present in the upper and lower halves of the dilatation are more pronounced than in the steady flow model, the lower occupying the entire sector.

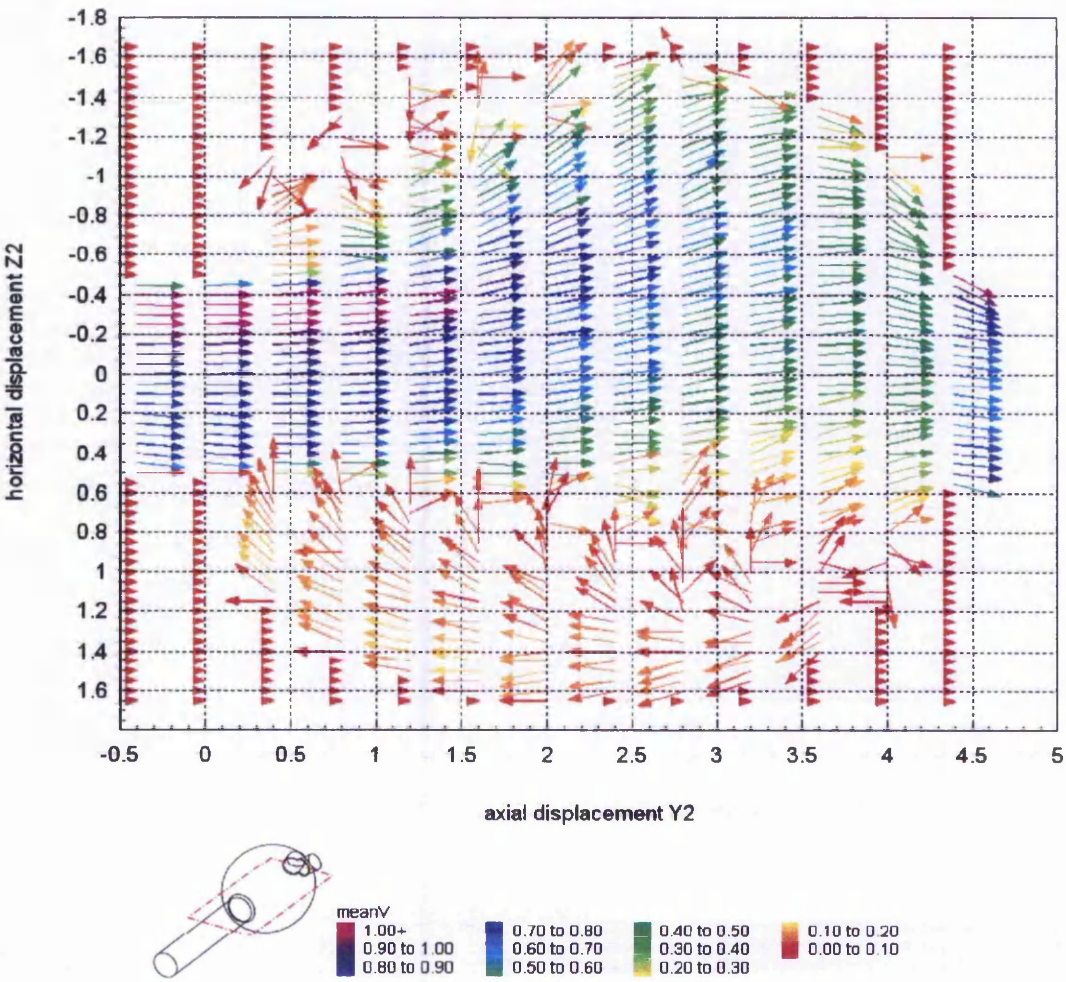

Figure 4-12 Full field velocity plot, torsional inlet-steady flow, horizontal XY plane

The horizontal data (Figure 4-12) shows the flow to be markedly skewed to outside section of the aneurysm. The flow became detached from the wall shortly after the inlet there was a region of detached, stagnation that occurred trapped behind this skewed flow. The expanded jet proceeded to fill the outside sector before accelerating at the outlet. On the opposite sector a large zone of recirculation was generated. A small, distally located vortex can be seen in the vector plot, however, there is no stagnant uncertain flow region. It is apparent that this area of reversed flow sweeps the adjacent wall of the aneurysm to rejoin the core flow at the inlet. The exit velocities were seen to remain attached to the upper distal wall of the geometry and leave the aneurysm sweeping with a dorsal vector. The highest velocities were seen at the top and bottom edges of this exit

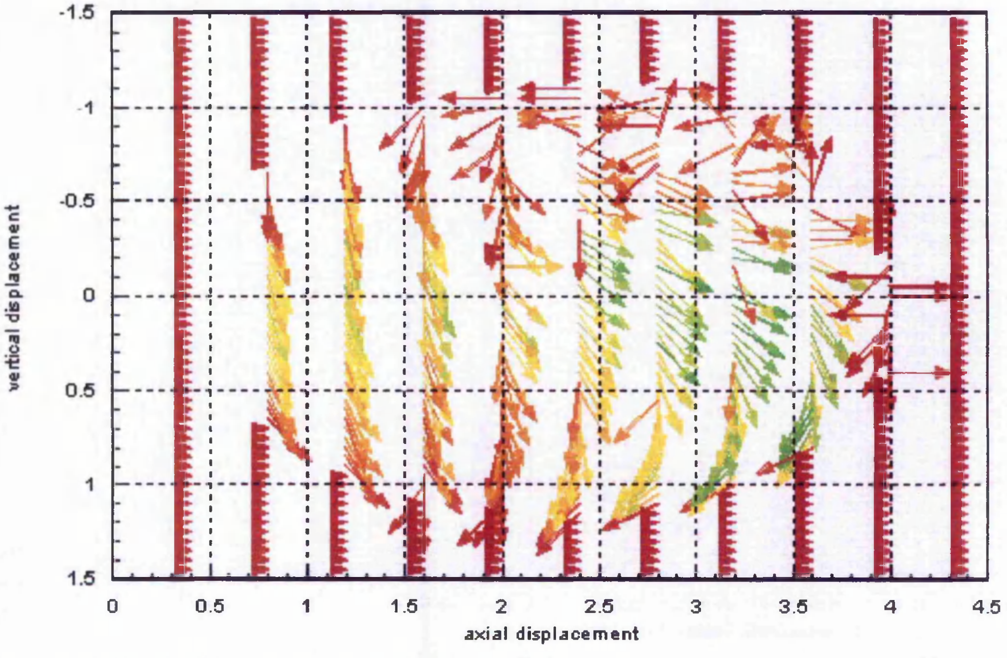

Figure 4-13 Offset velocity profile, torsional steady flow: -0.55d from central axis, vertical plane

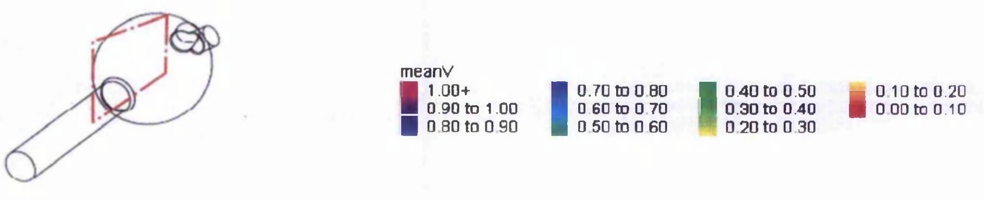

Figure 4-13 shows the outside sector of the aneurysmal bulge where the flow is swept due to the aortic torsion. It can be seen that the flow also rotated dorsally and either exited the model or impinged distally upon the lower wall. A small vortex was seen where the flow detached from the top of the aneurysm.

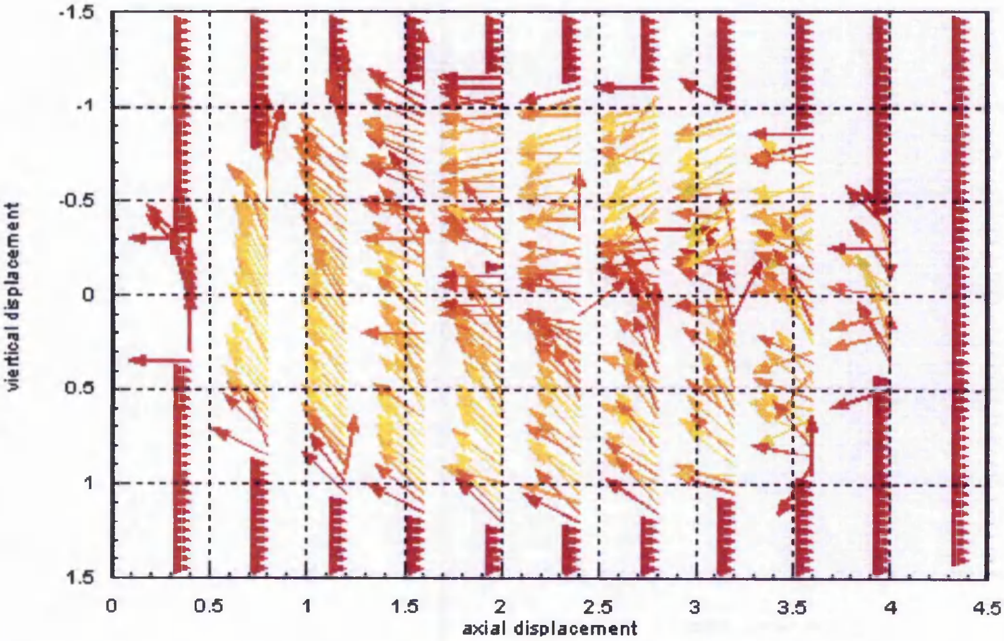

Figure 4-14 Offset velocity profile, torsional steady flow: +0.55d from central axis, vertical plane

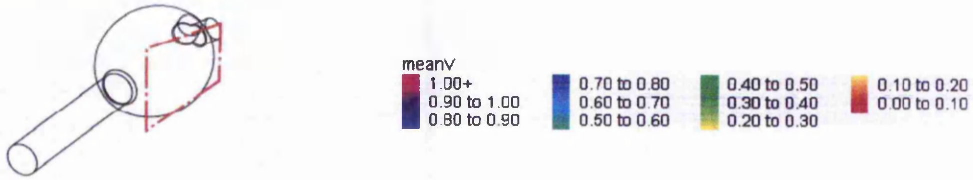

The flow plane on the opposite side of the bulge (Figure 4-14) was generally ordered and no stagnant regions were seen. In this half of the aneurysm the inlet torsion has prevented areas of stagnation.

4.4 Non-torsional Inlet Pulsatile Flow Results

4.4.1 INLET CONDITIONS

The graphs on the proceeding pages show the pulsatile inlet boundary conditions in two manners.

Firstly the measured velocity profiles across the vertical plane of the inlet, each graph representing a different time frame within the pulsatile cycle. The second graph in each category indicates the velocity of measured particles perpendicular to that plane in order to indicate any rotation involved. The Y-axis shows velocities that are non-dimensionalised against the peak inlet velocity used in this investigation.

The velocity profiles show data taken in the vertical profile of the inlet. Comparable graphs were plotted from the horizontal inlet plane and were seen to correspond to the trend shown here. Quantitative peak values comparing the horizontal and vertical profiles for each time frame matched to within 2-8%. The horizontal velocity plots likewise showed little or no rotation in the flow. Any velocities measured in either plane were randomly distributed and seen to be between $-0.02<u_x<0.02$m/s and $-0.02<u_z<0.01$m/s for the vertical and horizontal profiles respectively showing no torsion in the inlet flow.

Flow parameters were maintained between steady and transient flow wherever possible and can be seen in section 3.1.3.

Secondly complete vector plots (Figure 4-15 to Figure 4-20) are presented which show the same data under a more comprehensive grid of data points. Axial velocities taken from these experiments are also included for completeness. However, this data suffers from a lower data rate and is of more qualitative value.

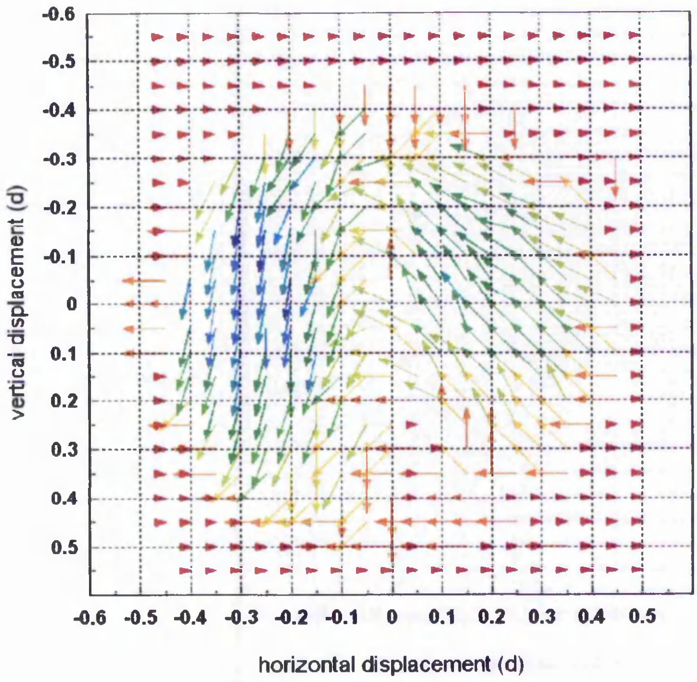

Figure 4-15 Cross section of pulsatile inlet at 0.05t

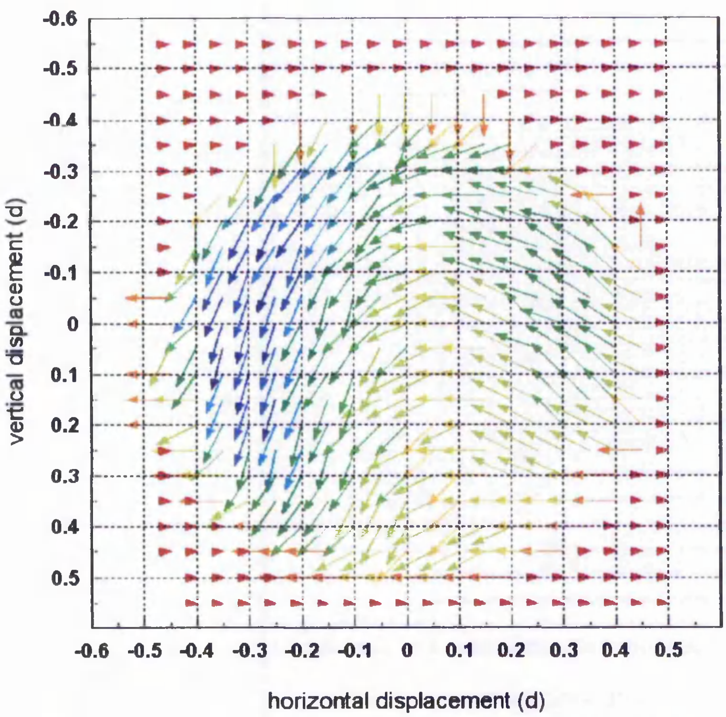

Figure 4-16 Cross section of pulsatile inlet at 0.15t

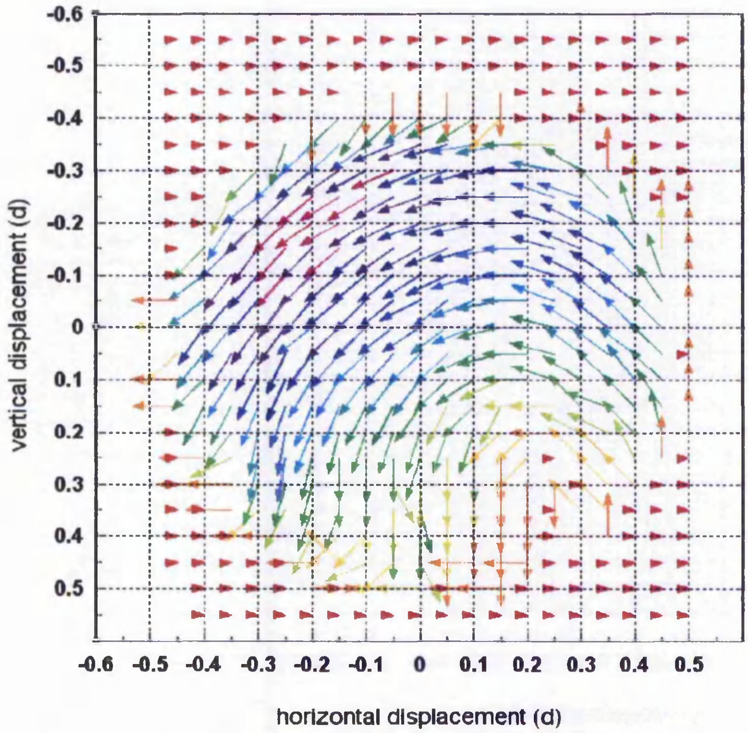

Figure 4-17 Cross section of pulsatile inlet at 0.3t

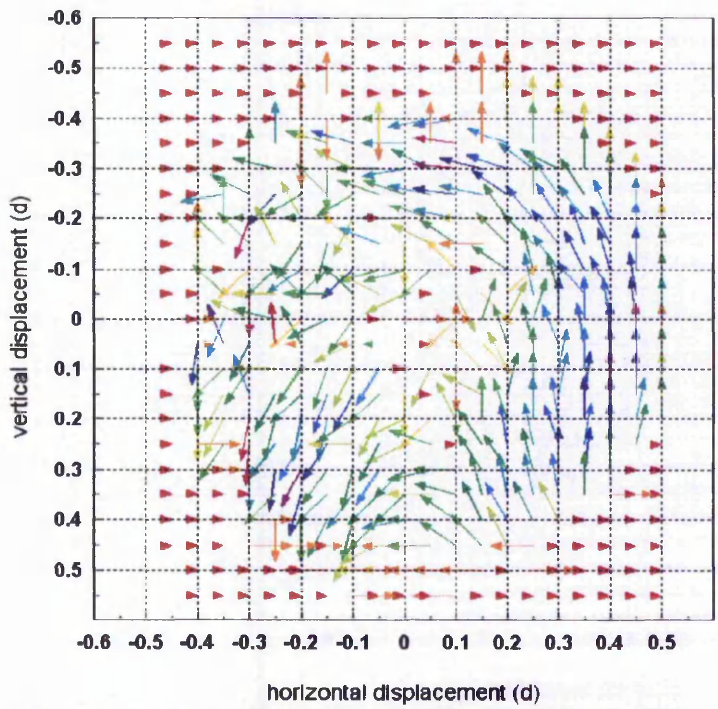

Figure 4-18 Cross section of pulsatile inlet at 0.55t

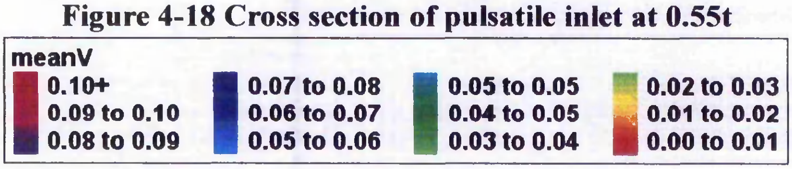

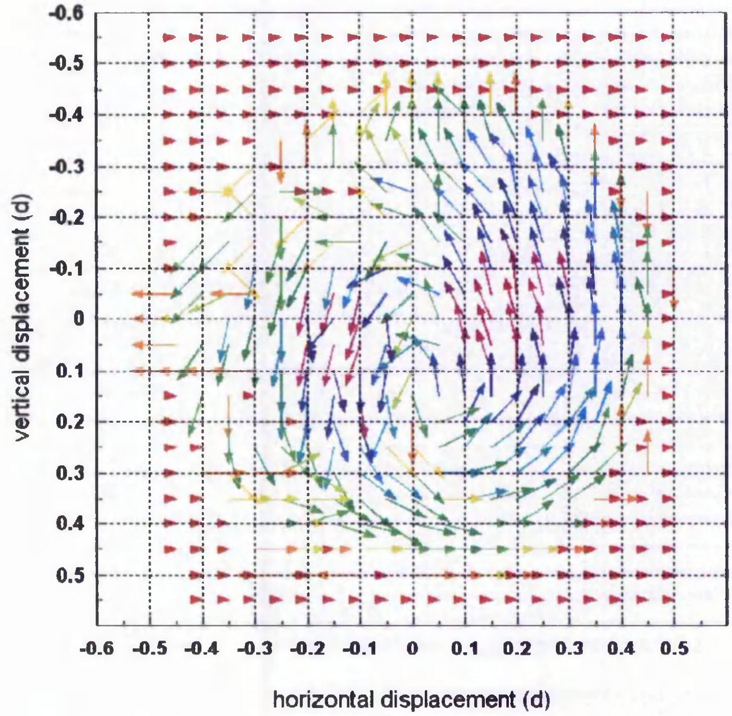

Figure 4-19 Cross section of pulsatile inlet at 0.8t

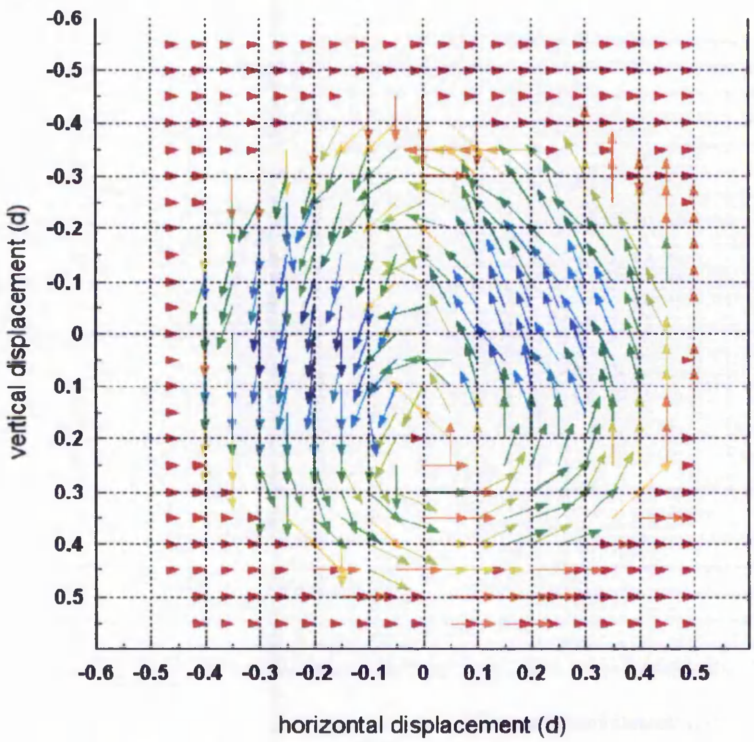

Figure 4-20 Cross section of pulsatile inlet at 0.95t

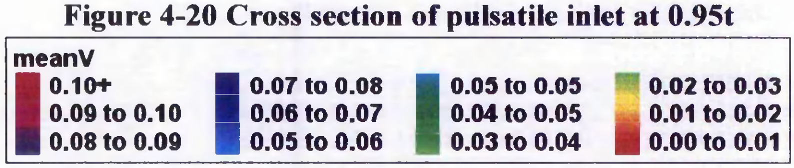

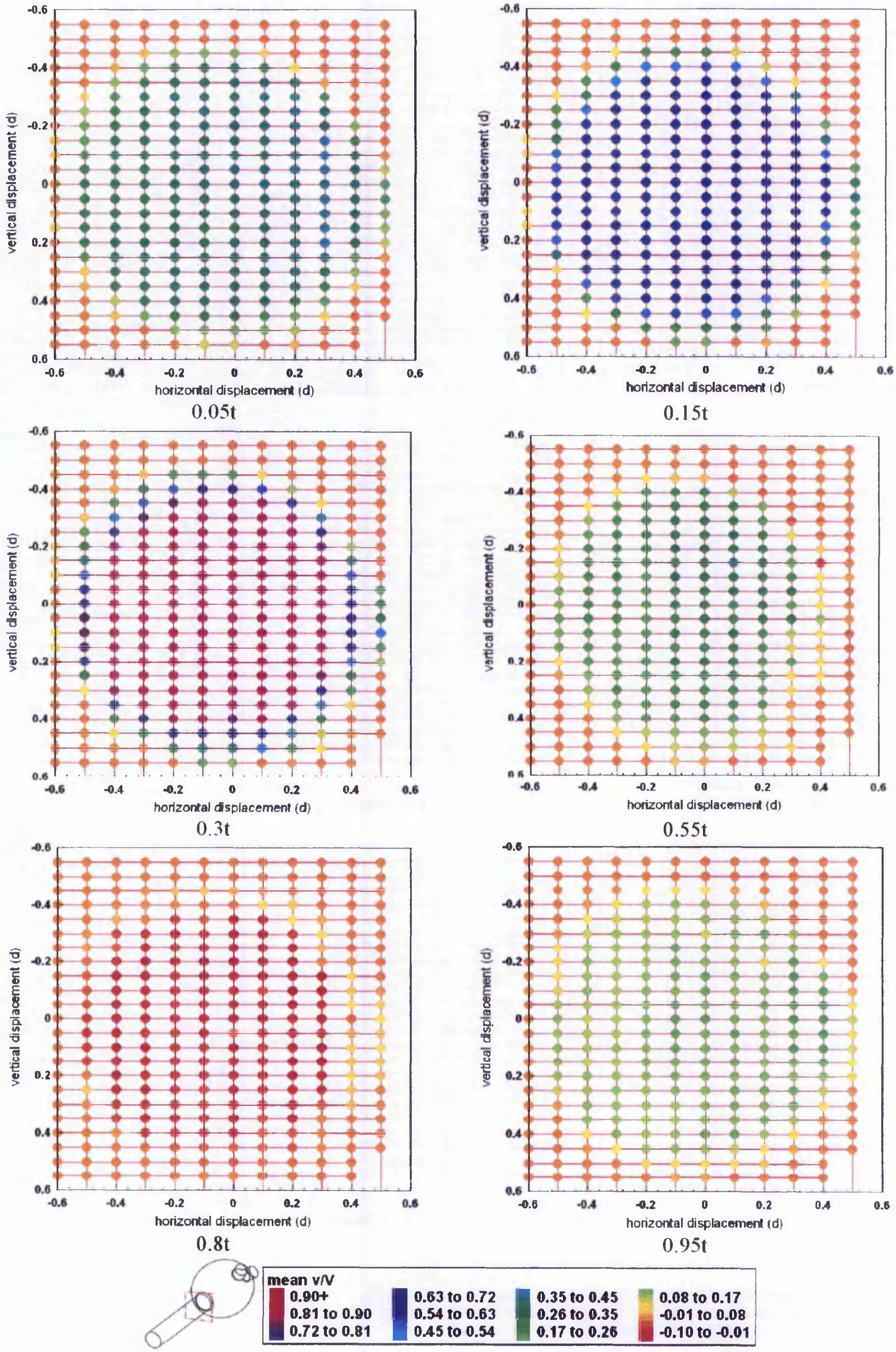

Figure 4-21 Plots showing velocity distributions throughout the pulsatile cycle

Non-dimensionalised axial velocity against axial displacement (d)

Non-dimensionalised transverse velocity against axial displacement (d)

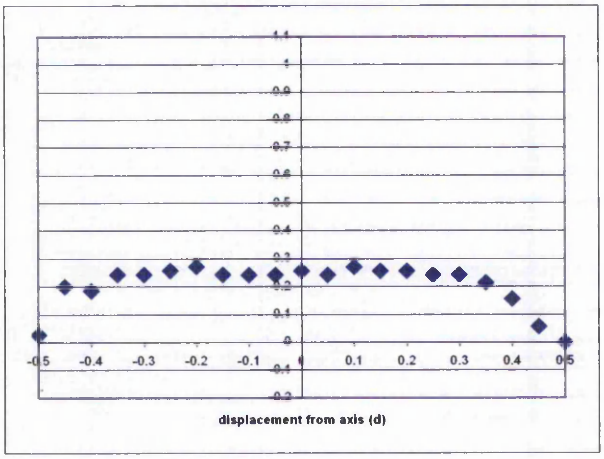

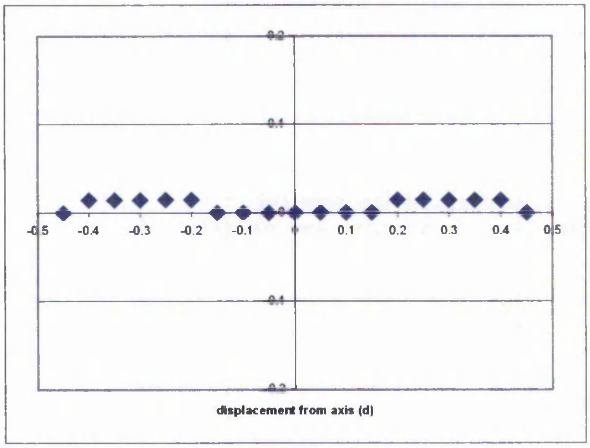

0.05t

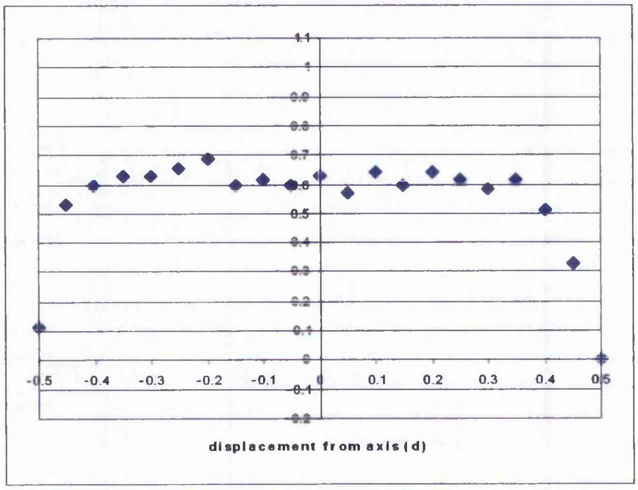

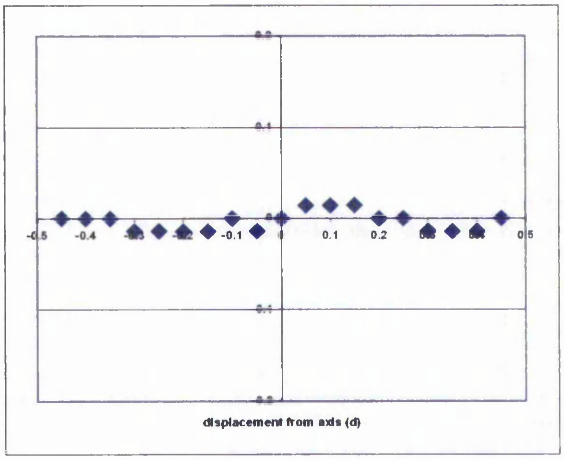

0.15t

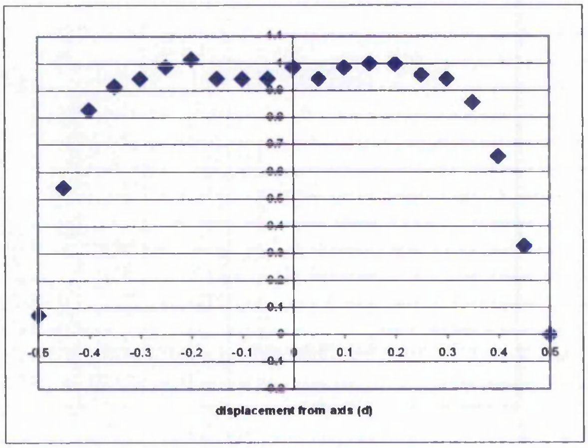

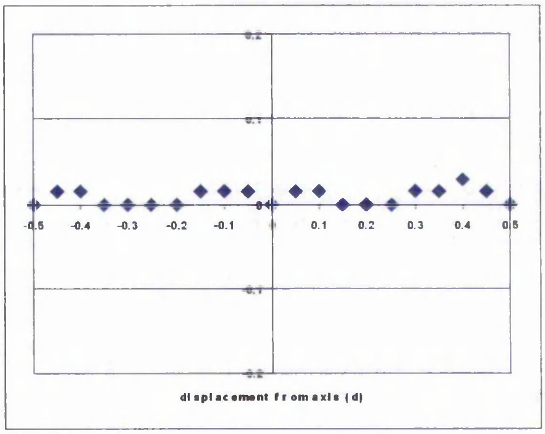

0.3t

Non-dimensionalised axial velocity against axial displacement (d) | *Non-dimensionalised transverse velocity against axial displacement (d)*

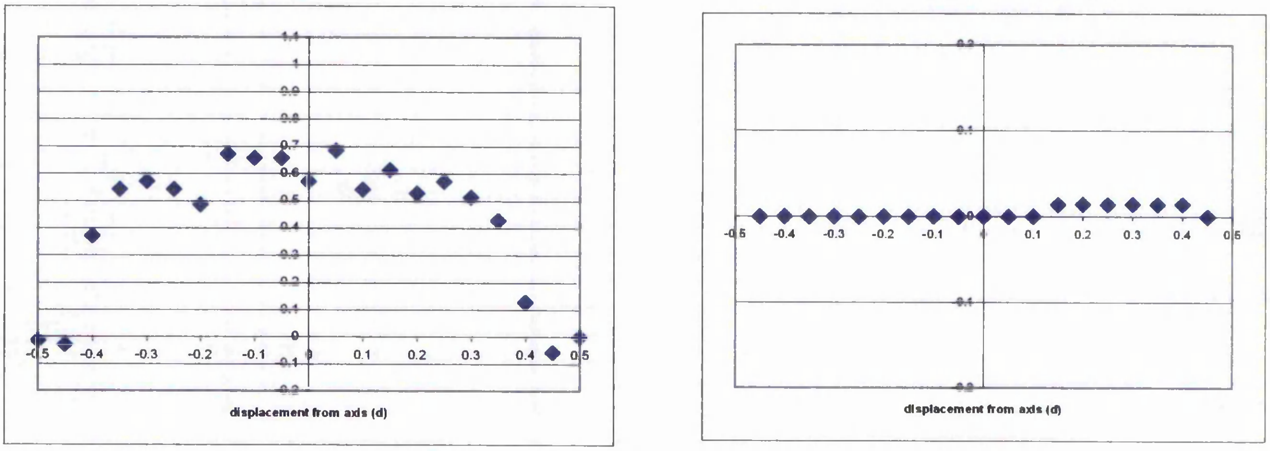

0.55t

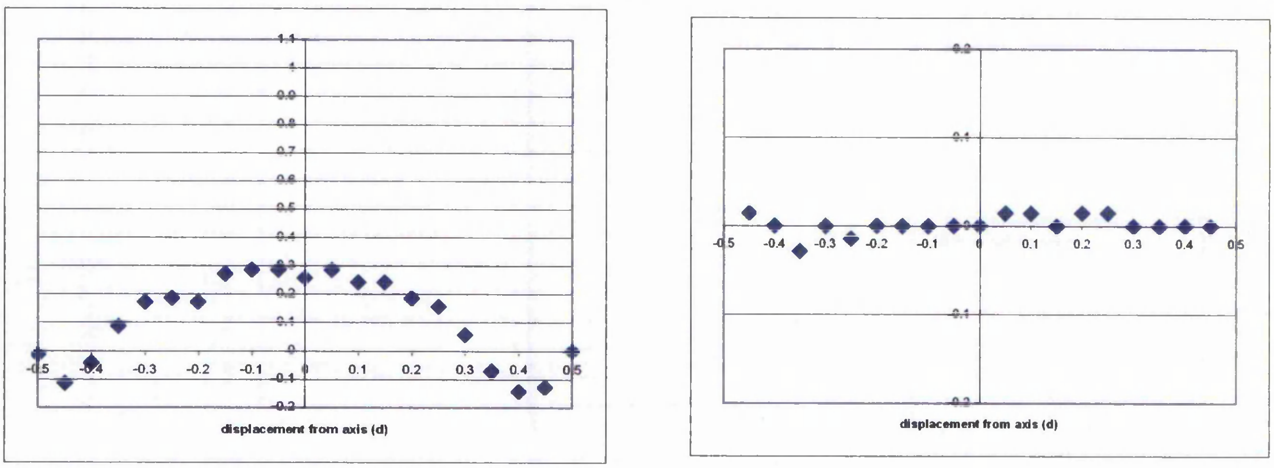

0.88t

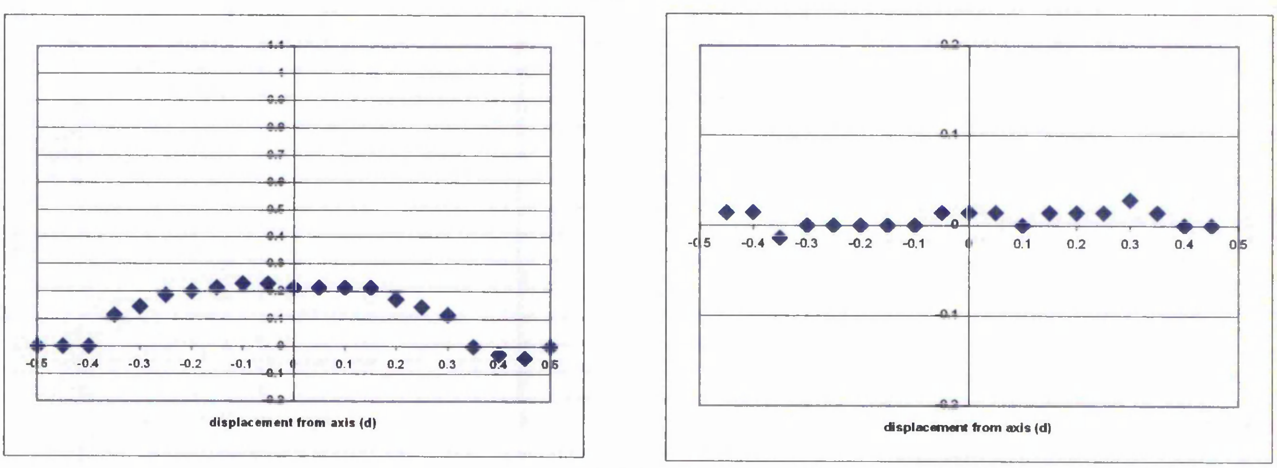

0.95t

Figure 4-22 Scatter plots showing pulsatile non-torsional inlet velocity profiles in the vertical plane

4.4.2 FULL FIELD VECTOR PLOT DATA

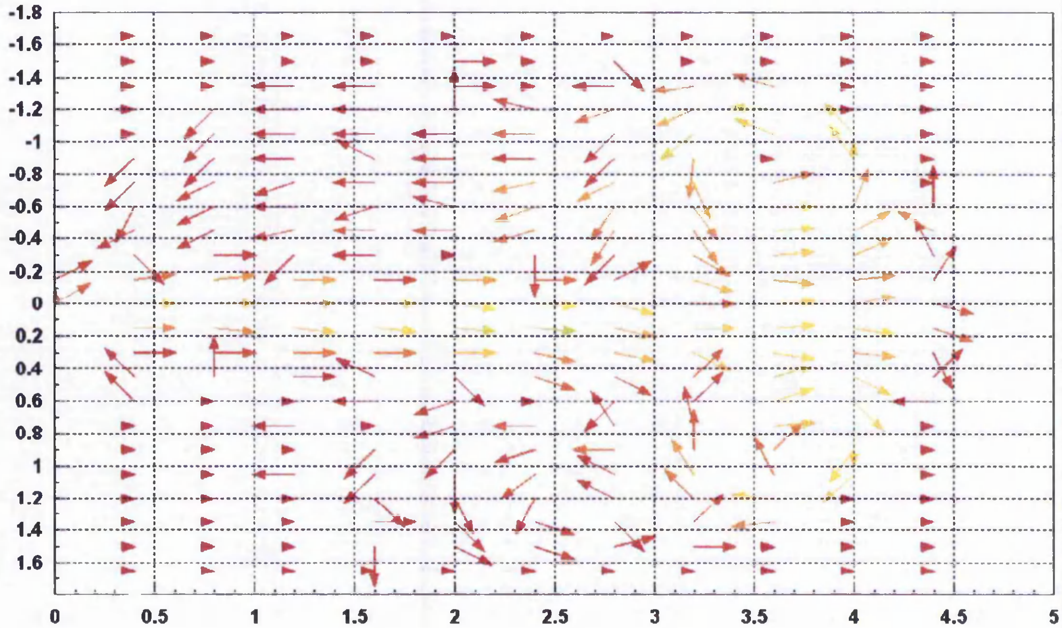

Figure 4-23 Pulsatile full-field flow, ZY plane, angle bin 18

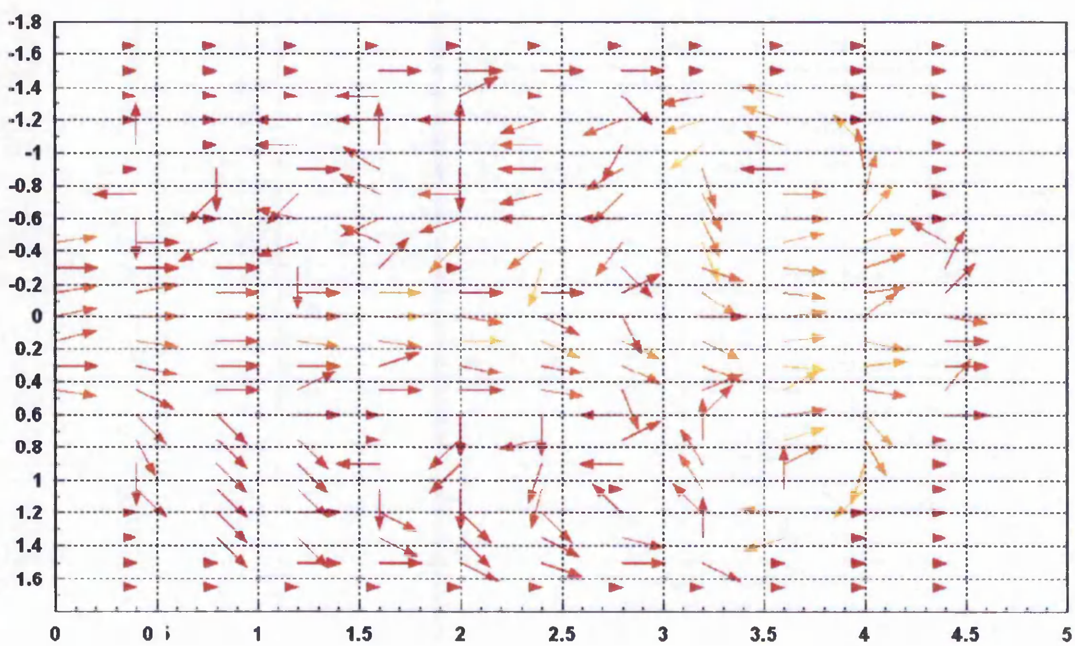

Figure 4-24 Pulsatile full-field flow, ZY plane, angle bin 54

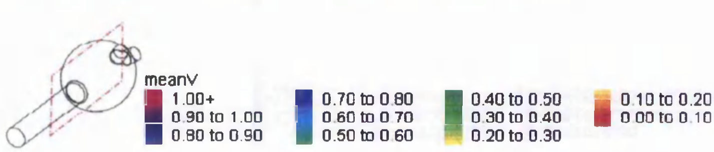

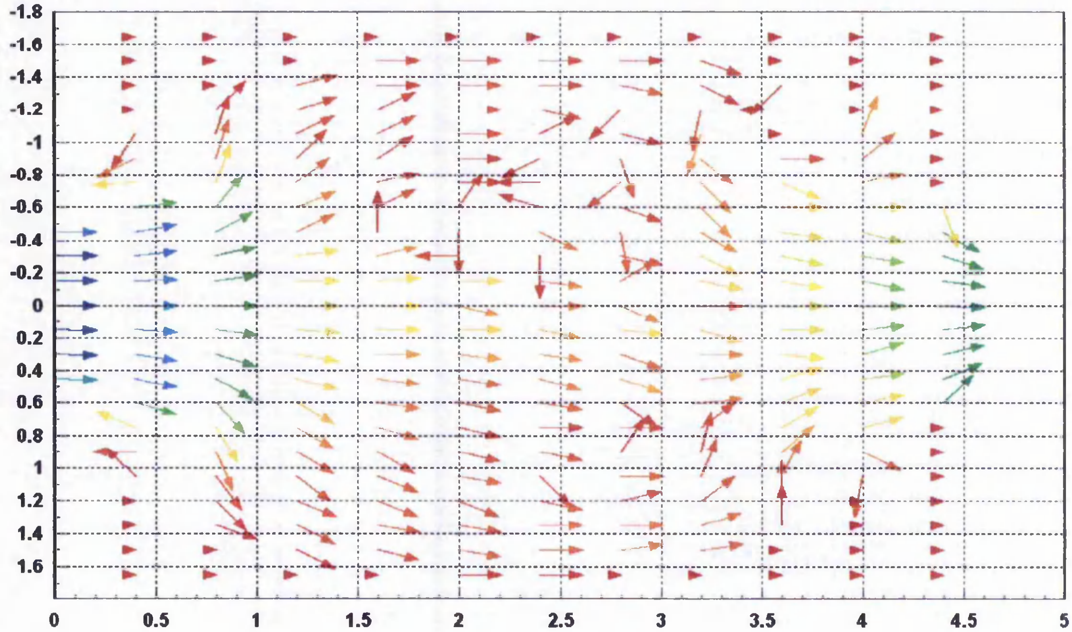

Figure 4-25 Pulsatile full-field flow, ZY plane, angle bin 108

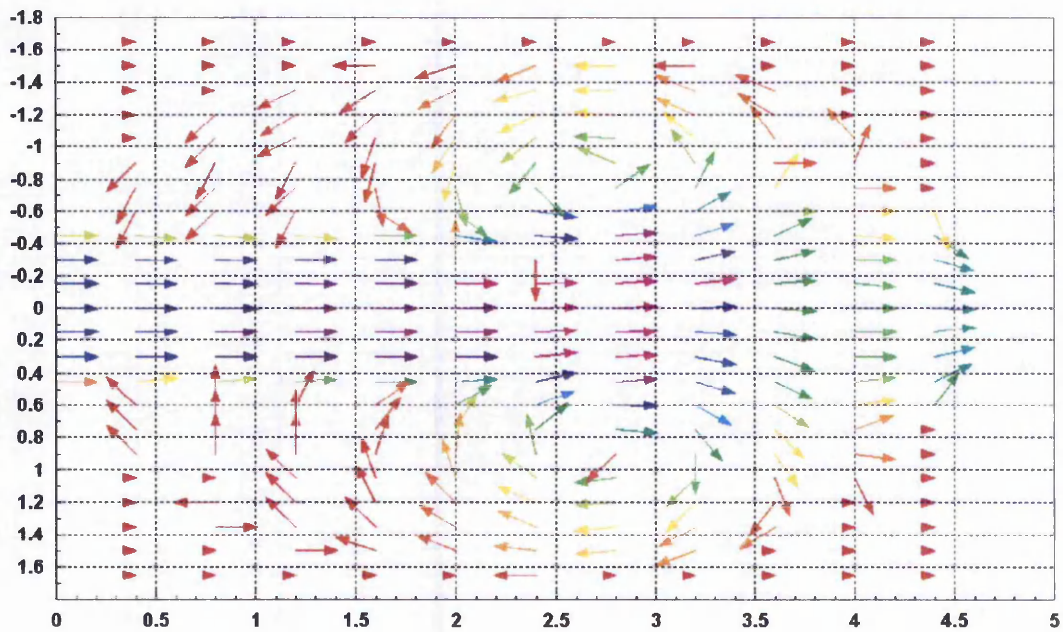

Figure 4-26 Pulsatile full-field flow, ZY plane, angle bin 198

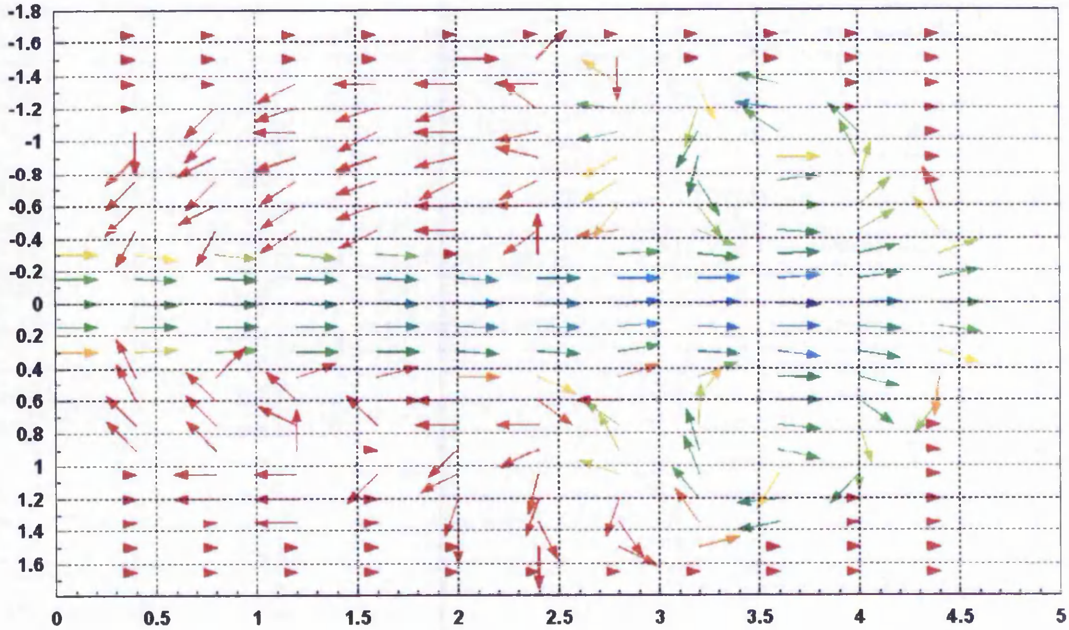

Figure 4-27 Pulsatile full-field flow, ZY plane, angle bin 288

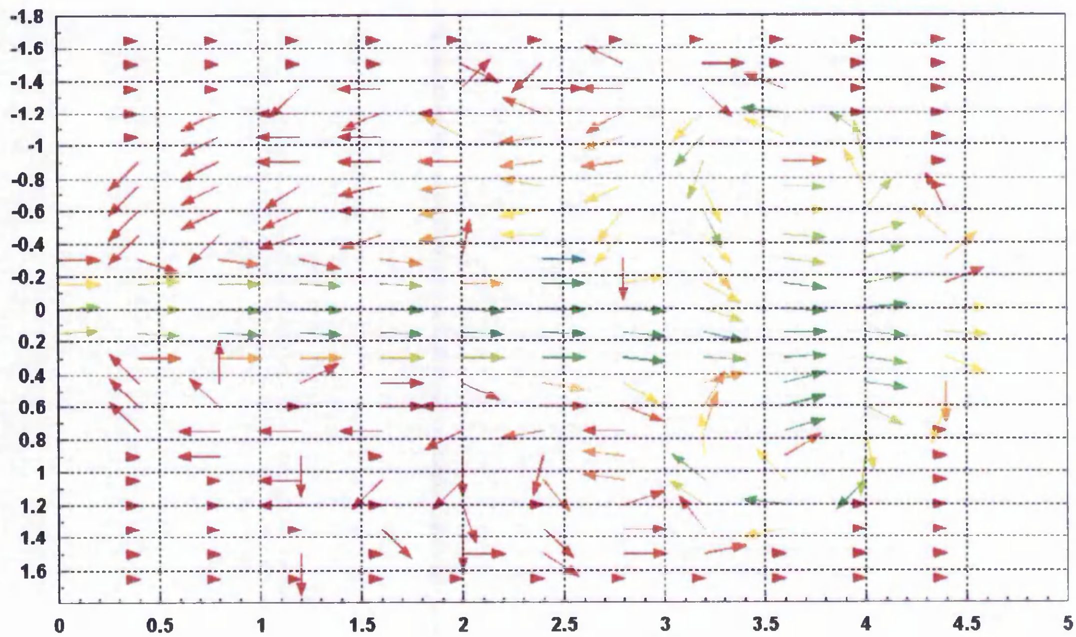

Figure 4-28 Pulsatile full-field flow, ZY plane, angle bin 342

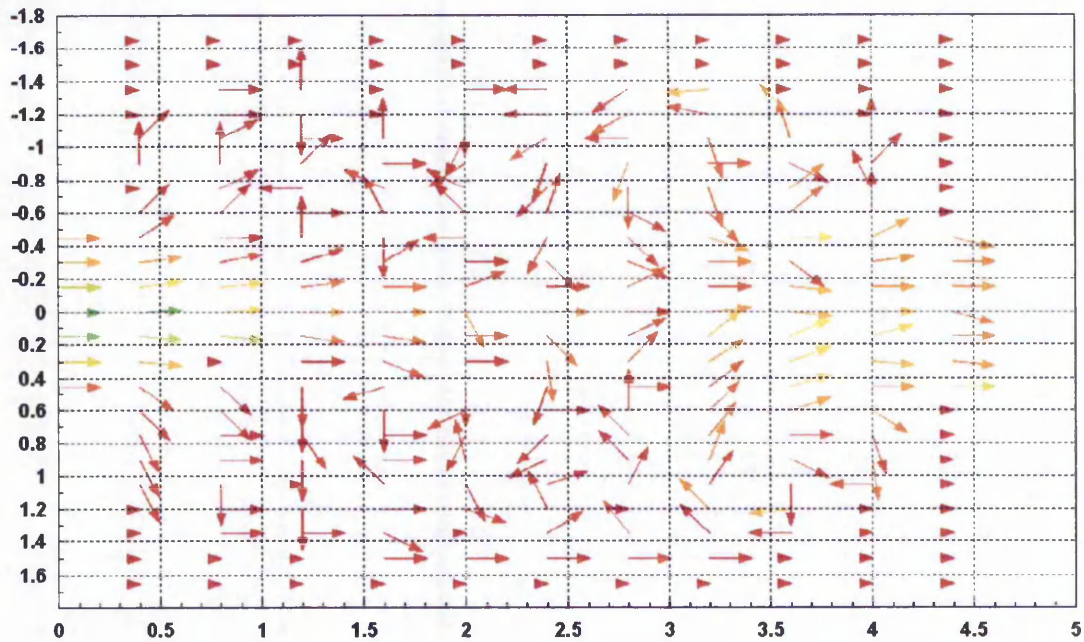

Figure 4-29 Pulsatile full-field flow, XY plane, angle bin 18

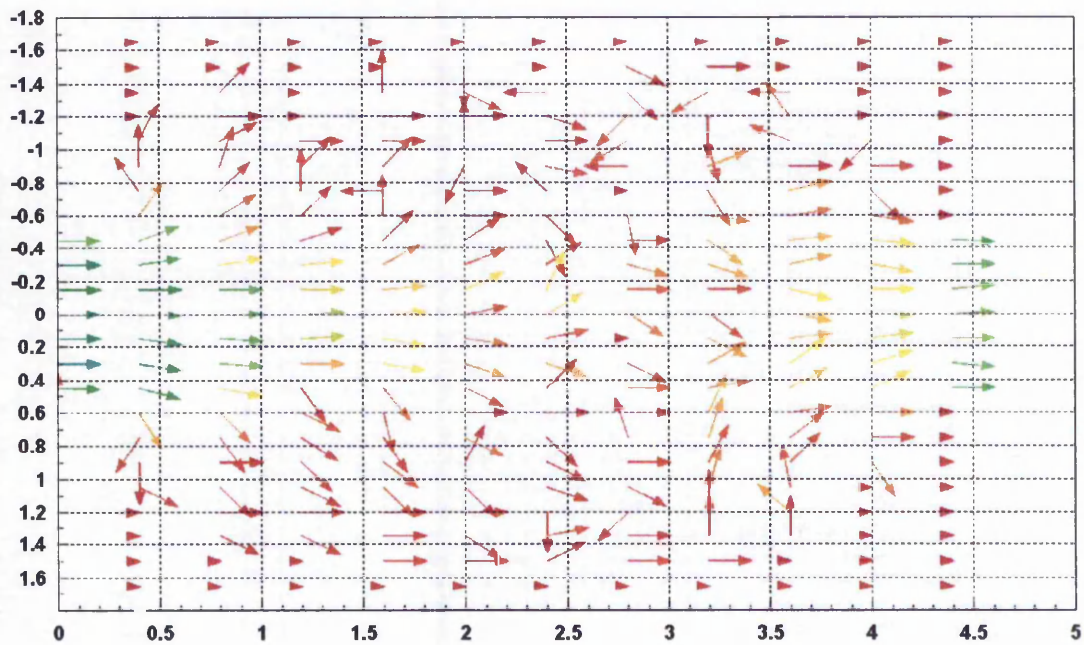

Figure 4-30 Pulsatile full-field flow, XY plane, angle bin 54

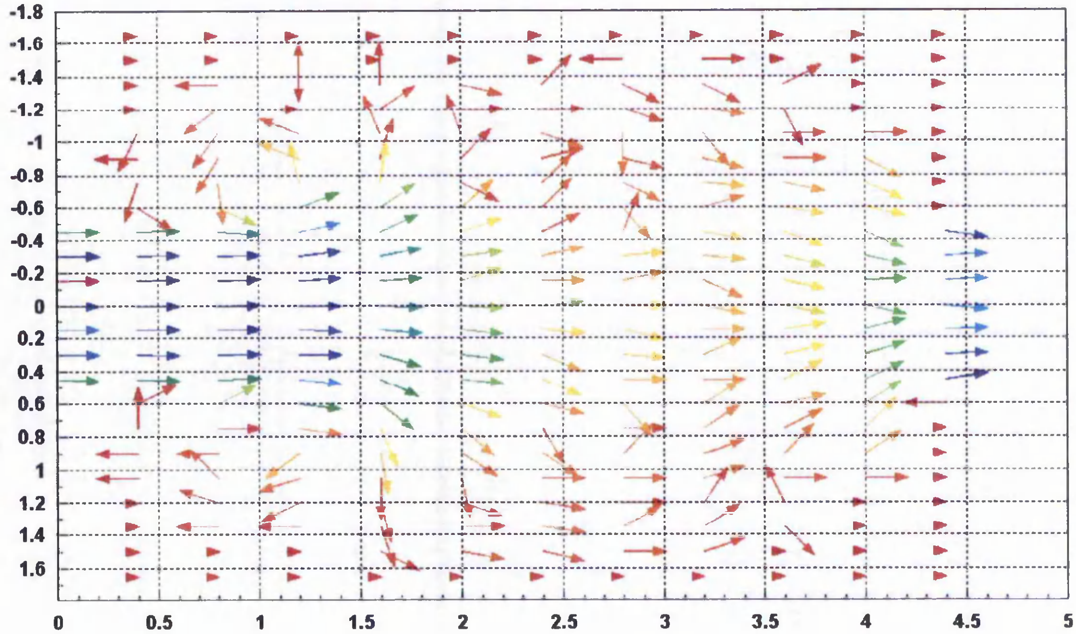

Figure 4-31 Pulsatile full-field flow, XY plane, angle bin 108

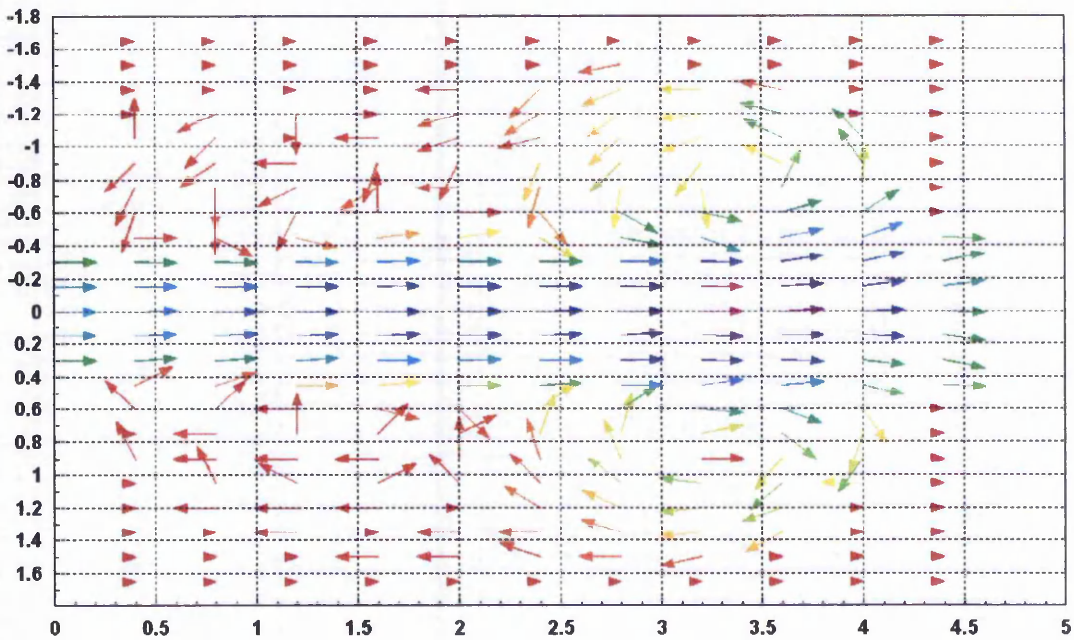

Figure 4-32 Pulsatile full-field flow, XY plane, angle bin 198

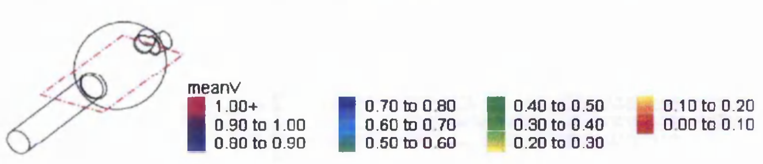

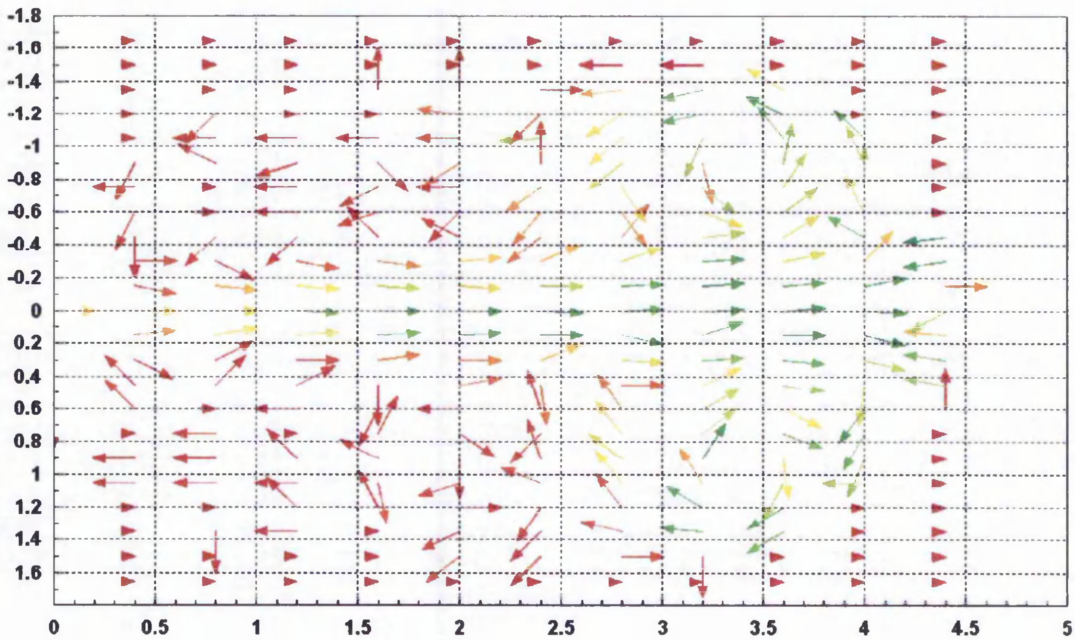

Figure 4-33 Pulsatile full-field flow, XY plane, angle bin 288

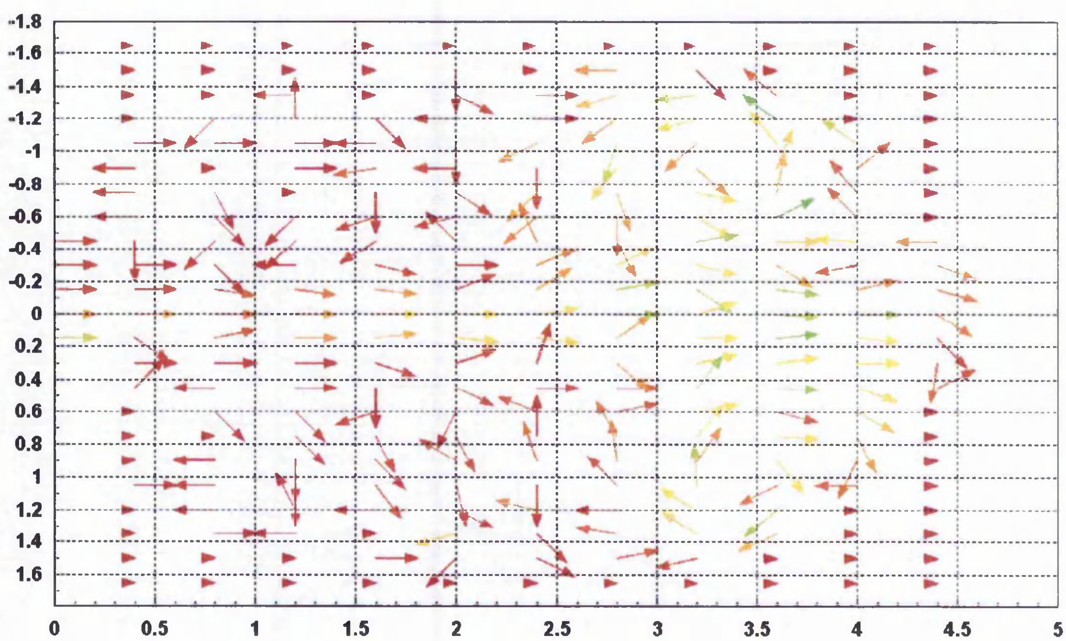

Figure 4-34 Pulsatile full-field flow, XY plane, angle bin 342

During the first stages of systole in the vertical plane (Figure 4-23) the flow presented a small central core of low velocity that terminated distally in gentle vortex formation, which did not fill the aneurysmal bulge. Although there was a trend in the upper section of the aneurysm for flow to return to the inlet only chaotic flow was seen in the lower half of the AAA close to the inlet.

During the acceleration (Figure 4-24) of the flow little acceleration of the jet core was seen, however, the distal vortices were maintained and the distal flow returning to the core became more disordered. In the Lower part of the AAA though, attached flow was seen to develop that impinged upon the lower wall of the AAA. This was not seen in the upper half of the aneurysmal bulge perhaps due to the returning flow seen in the previous phase of systole.

At peak systole (Figure 4-25) acceleration could be more clearly seen at the inlet and attached flow was present in both halves of the aneurysm. During this stage no discernable vortices were seen although a pocket of uncertain flow was seen along the centreline. This flow region would not be dominated immediately due to the velocities present. The outer regions of flow had a lower inertia and as such the cross-section of velocity across the centre of the aneurysm was seen to be almost evenly distributed. It is worth noting that in this geometry there were small areas of uncertain flow located close to the inlet. These might not be present in a model exhibiting a less extremely curved aneurysm.

Late systole (Figure 4-26) showed the formation of large recirculating vortices and near symmetry within the flow field. Core velocities were strong although the pulse of peak velocity was seen to be present distally in the model only offset from the centreline by 0.5d.The strong vortices formed left no room for areas of stagnation.

During diastole the flow was seen to decelerate and the domination of the central core diminish. Vortices seen in both upper and lower halves of the AAA decelerated and moved distally towards the outlet. Regions of unordered flow were then seen to be present proximally to the vortices, although a return flow close to the inlet was observed in the upper half of the geometry. This discrepancy could be attributed to a lack of symmetry in the experimental parameters at the inlet.

The velocities measured in the same time frames in the horizontal plane show similar flow conditions. However, flow attachment was not seen as clearly in peak systole (Figure 4-31). Instead core expansion appeared to take place later in the aneurysm. Also the vortices shown in late systole (Figure 4-32) did not dominate the entirety of the aneurysmal bulge. As such, from the data measured in the XY plane it cannot be assumed that areas of stagnation and permanently low fluid and wall shear stress do not occur during pulsatile flow under non-torsional inlet conditions in an aneurysm of this curvature.

4.5 Torsional Inlet Pulsatile Flow Results

4.5.1 Inlet Parameters

In a similar fashion to the non-torsional inlet parameters presented in Section 4.4.1 the velocity profiles measured throughout both horizontal and vertical planes are shown here. Critical is the development of rotational flow.

Non-dimensionalised axial velocity | Non-dimensionalised transverse velocity

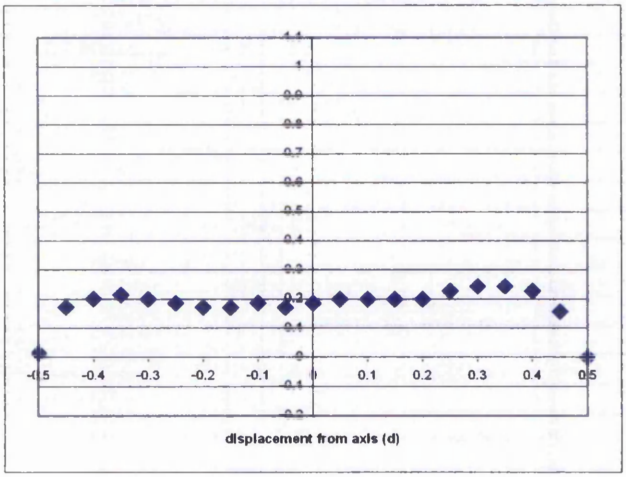

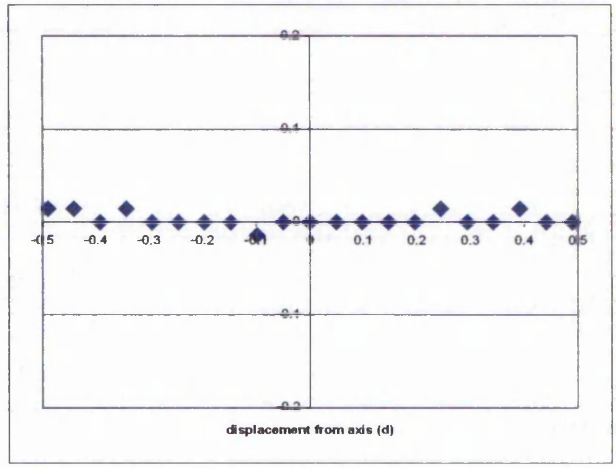

0.05t

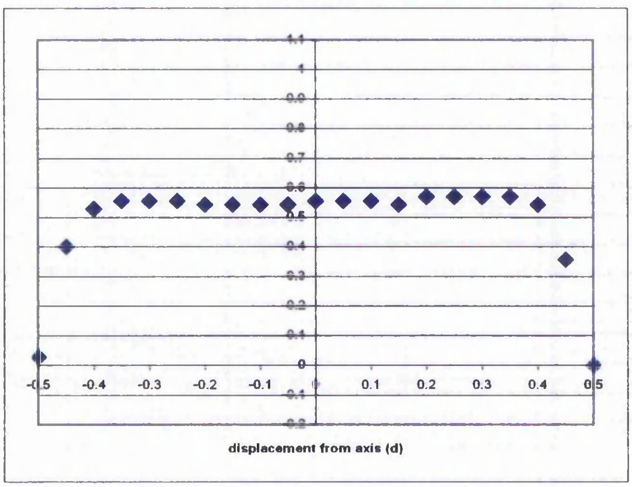

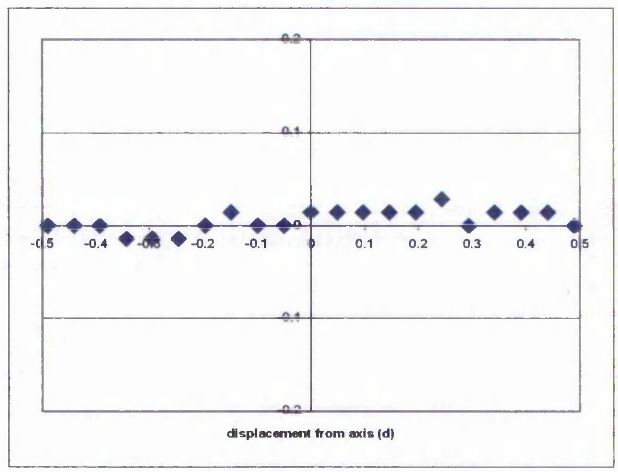

0.15t

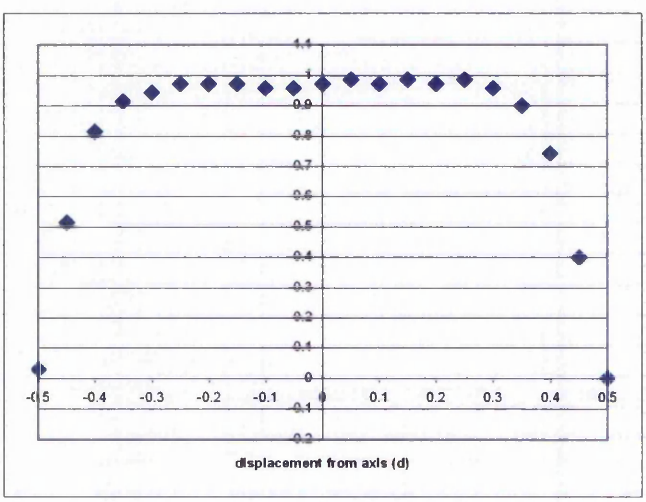

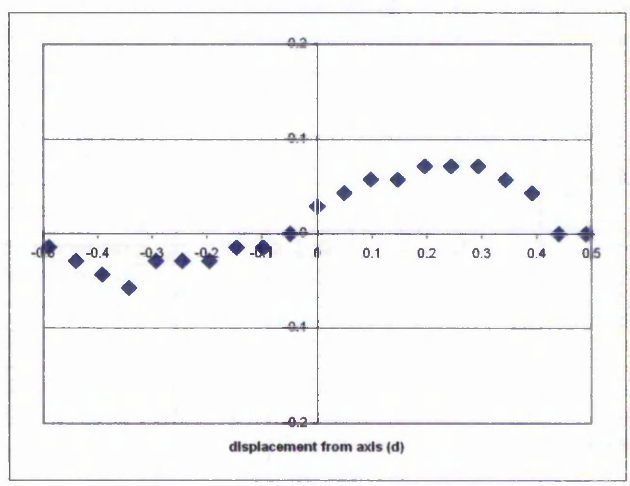

0.3t

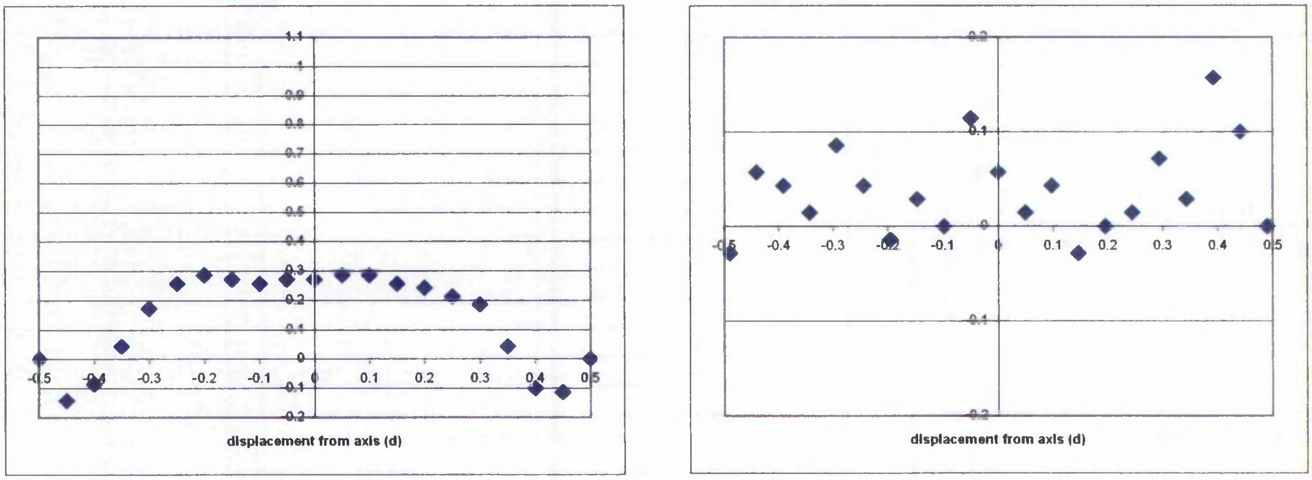

0.55t

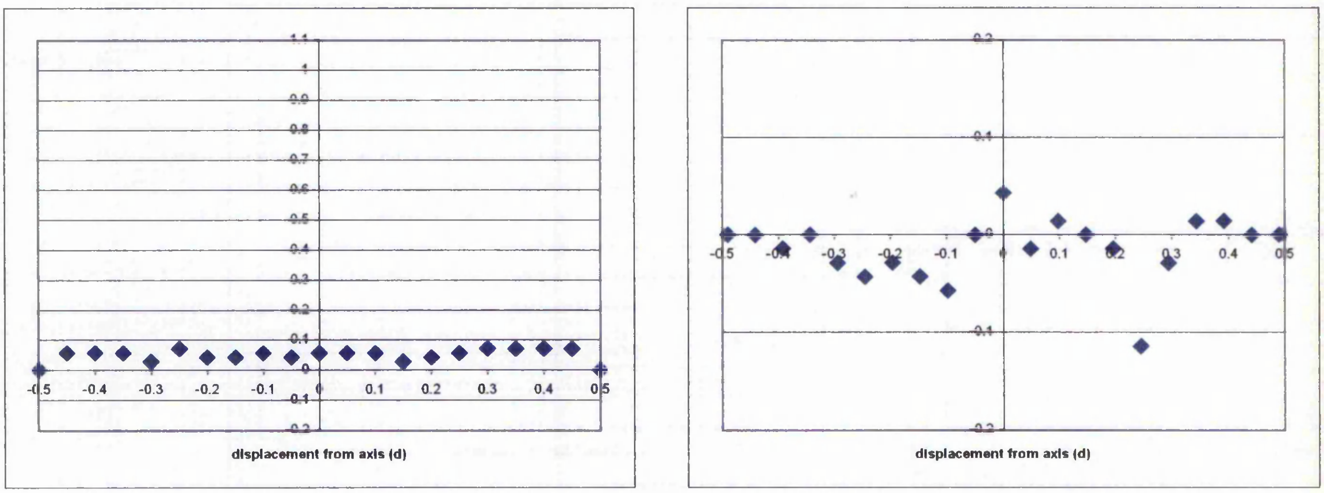

0.88t

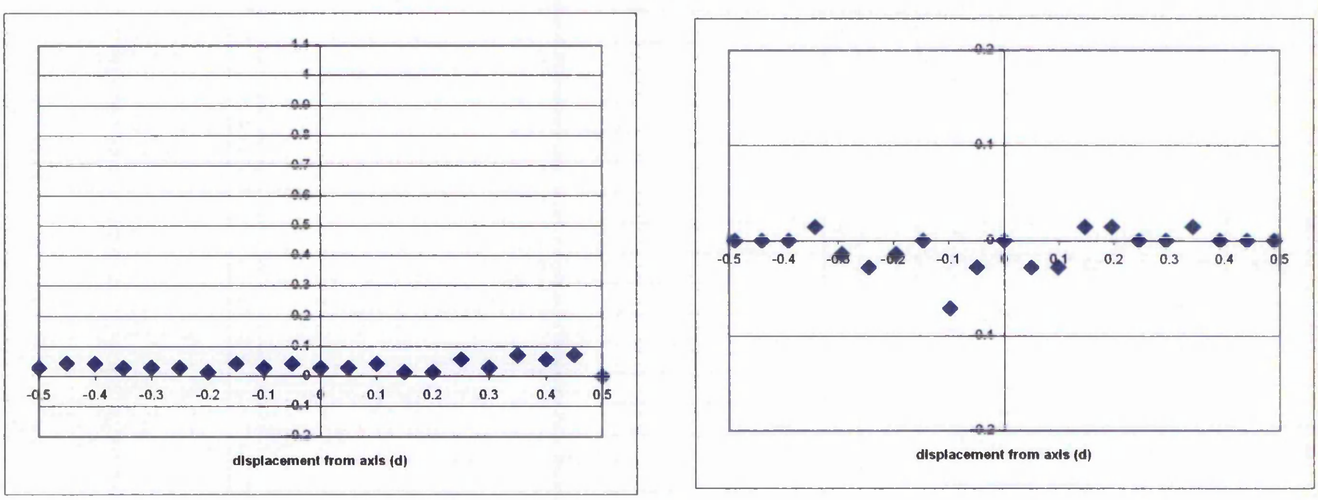

0.95t

Figure 4-35 Scatter plots showing pulsatile torsional inlet velocity profiles for the vertical plane

Non-dimensionalised axial velocity

Non-dimensionalised transverse velocity

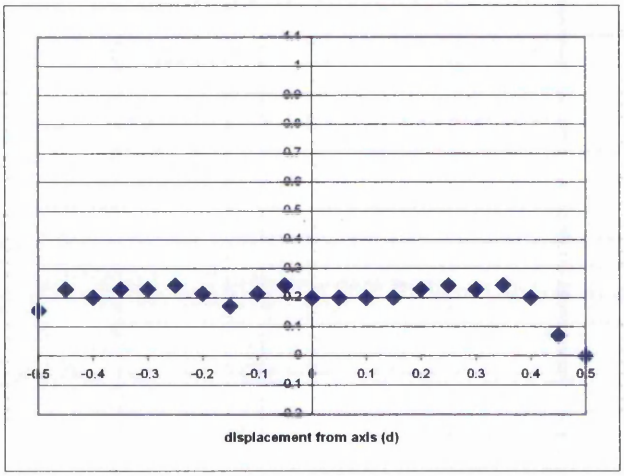

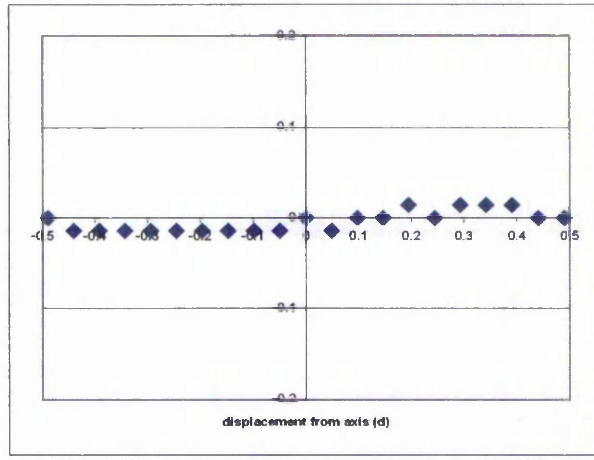

0.05t

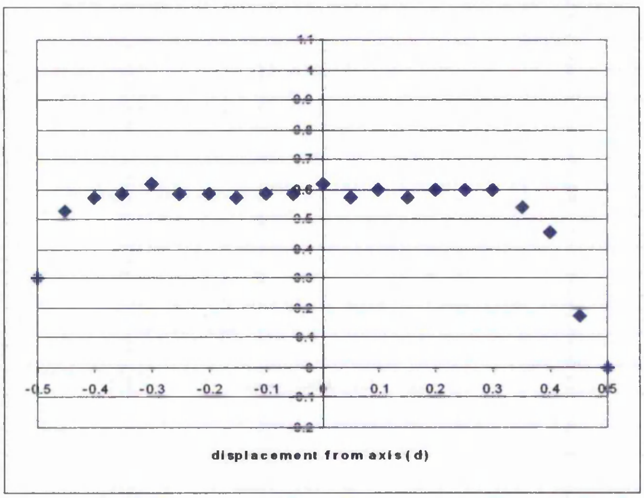

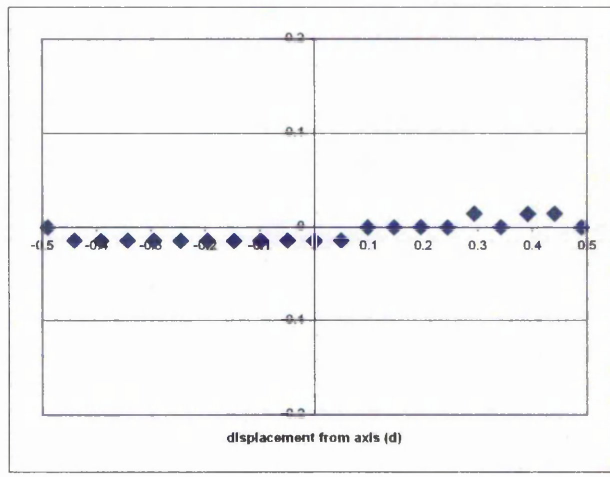

0.15t

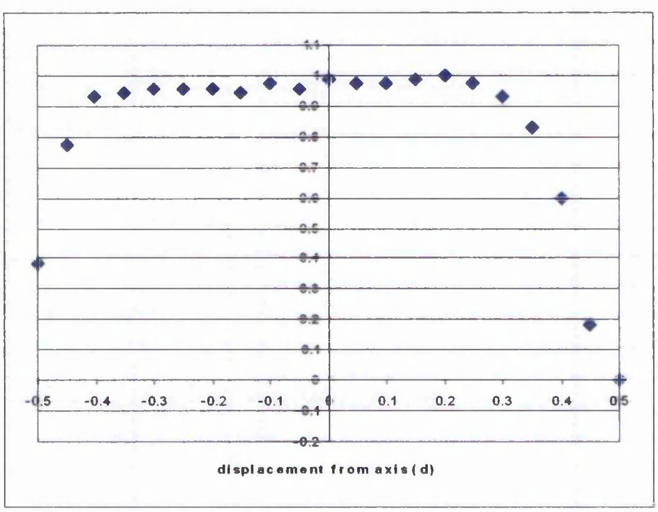

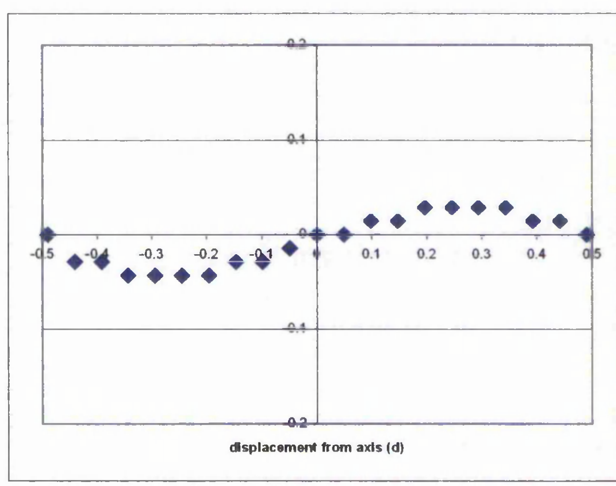

0.3t

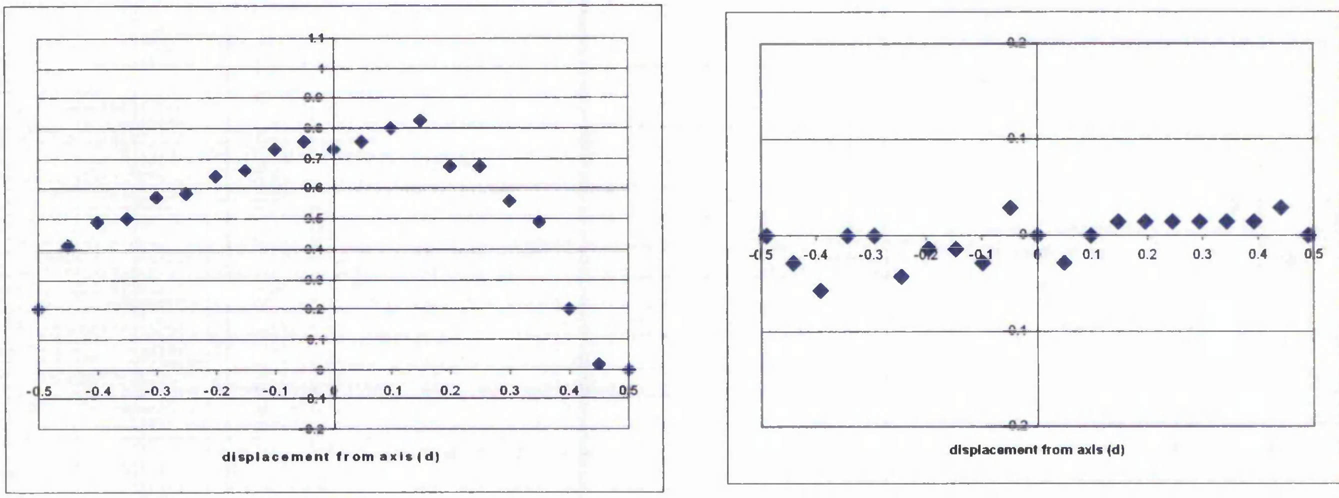

0.55t

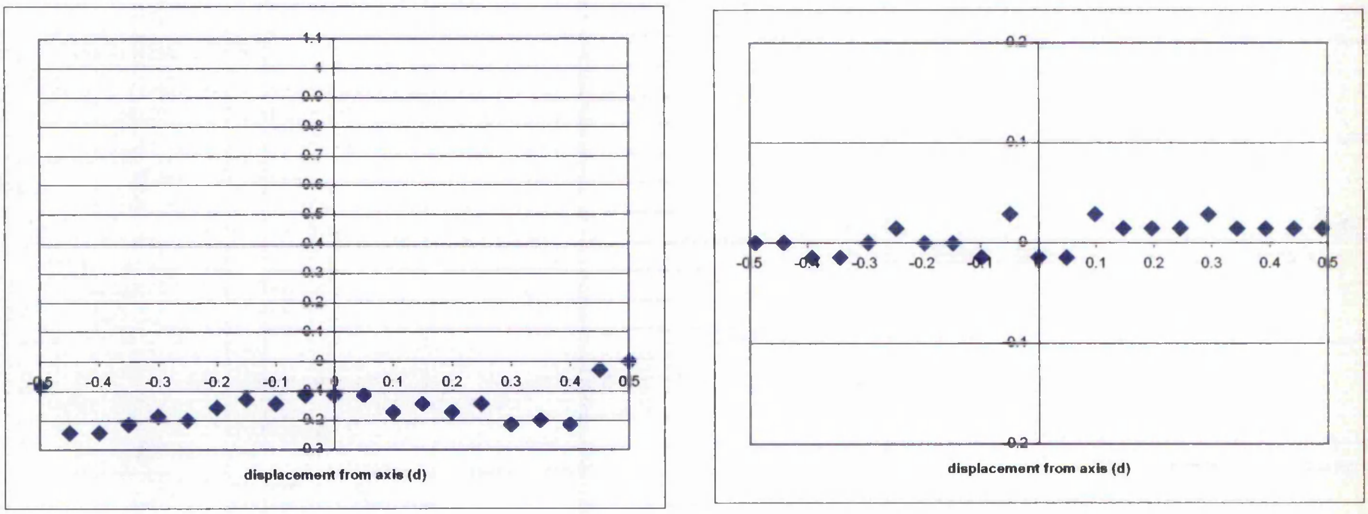

0.88t

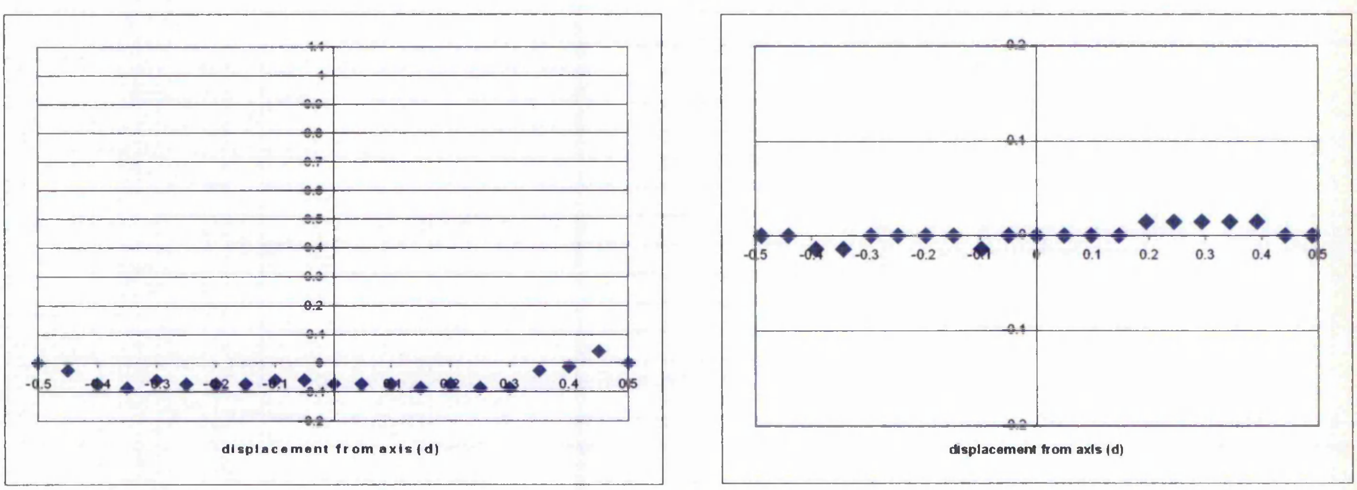

0.95t

Figure 4-36 Scatter plots showing pulsatile torsional inlet velocity profiles for the horizontal plane

4.5.2 Full Field Vector Plot Data

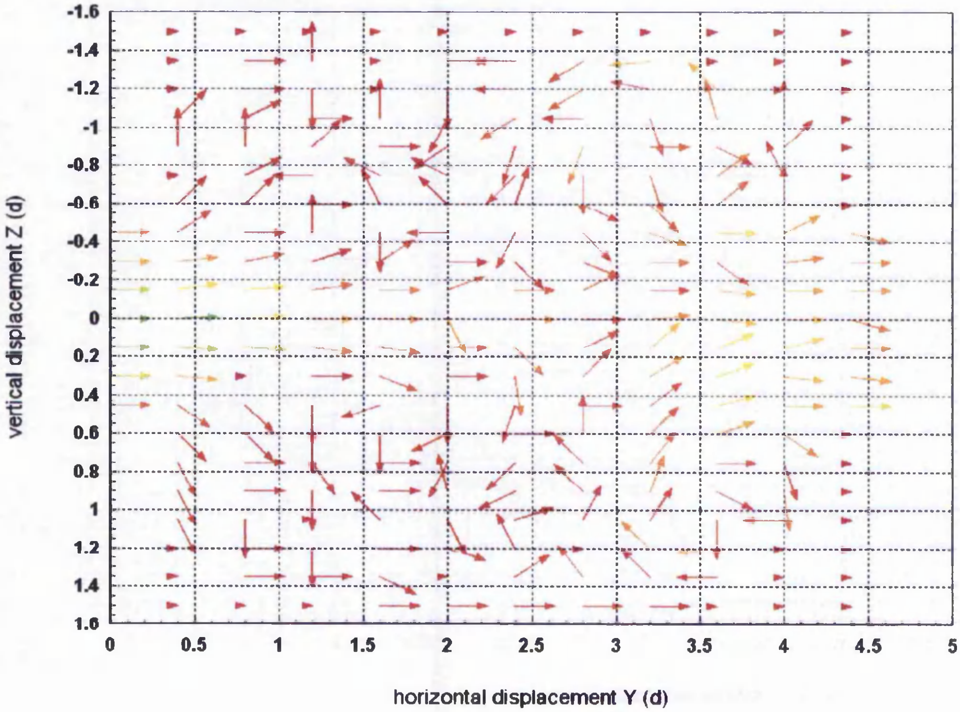

Figure 4-37 Pulsatile torsional full-field flow, YZ vertical plane, angle bin 18

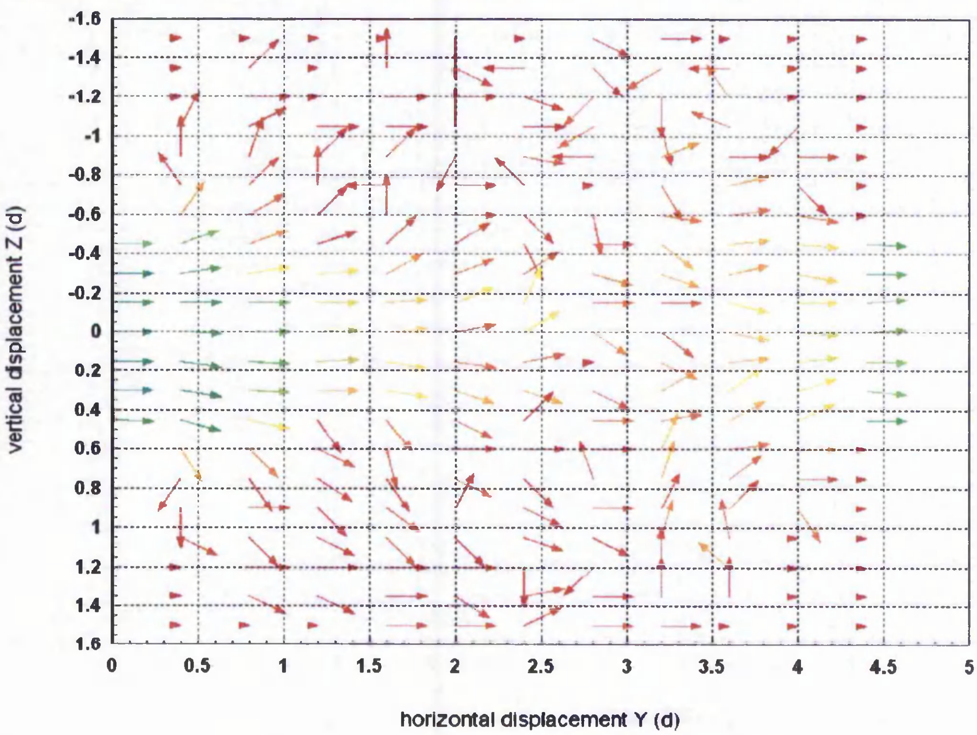

Figure 4-38 Pulsatile torsional full-field flow, YZ vertical plane, angle bin 54

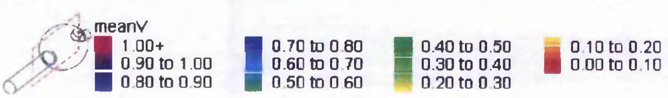

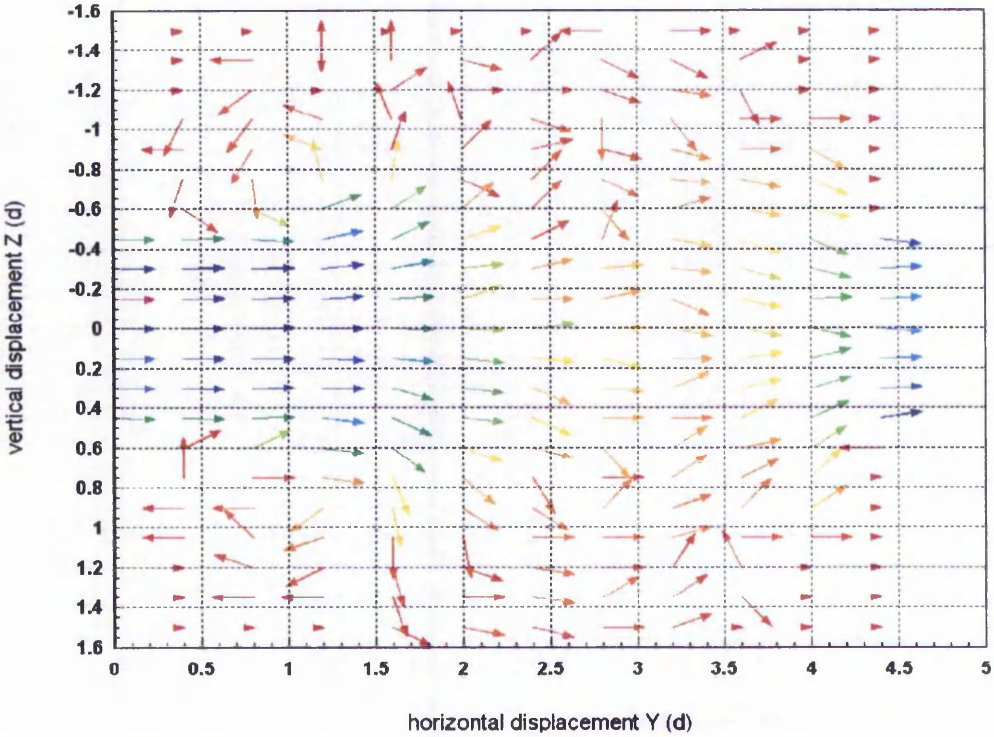

Figure 4-39 Pulsatile torsional full-field flow, YZ vertical plane, angle bin 108

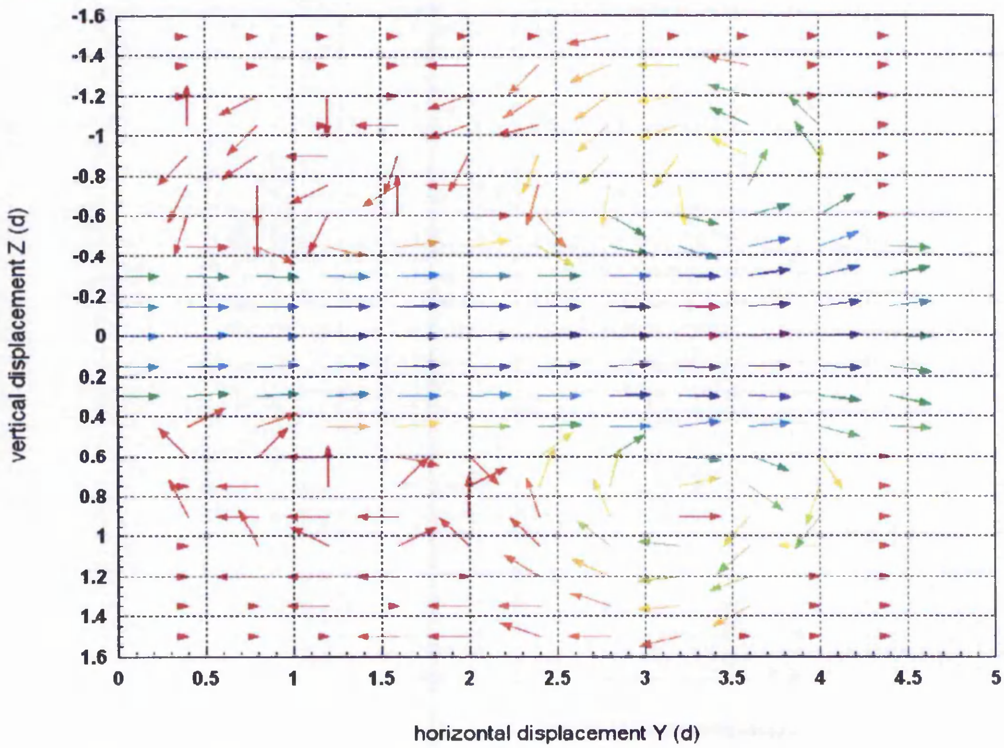

Figure 4-40 Pulsatile torsional full-field flow, YZ vertical plane, angle bin 198

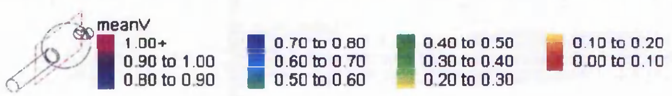

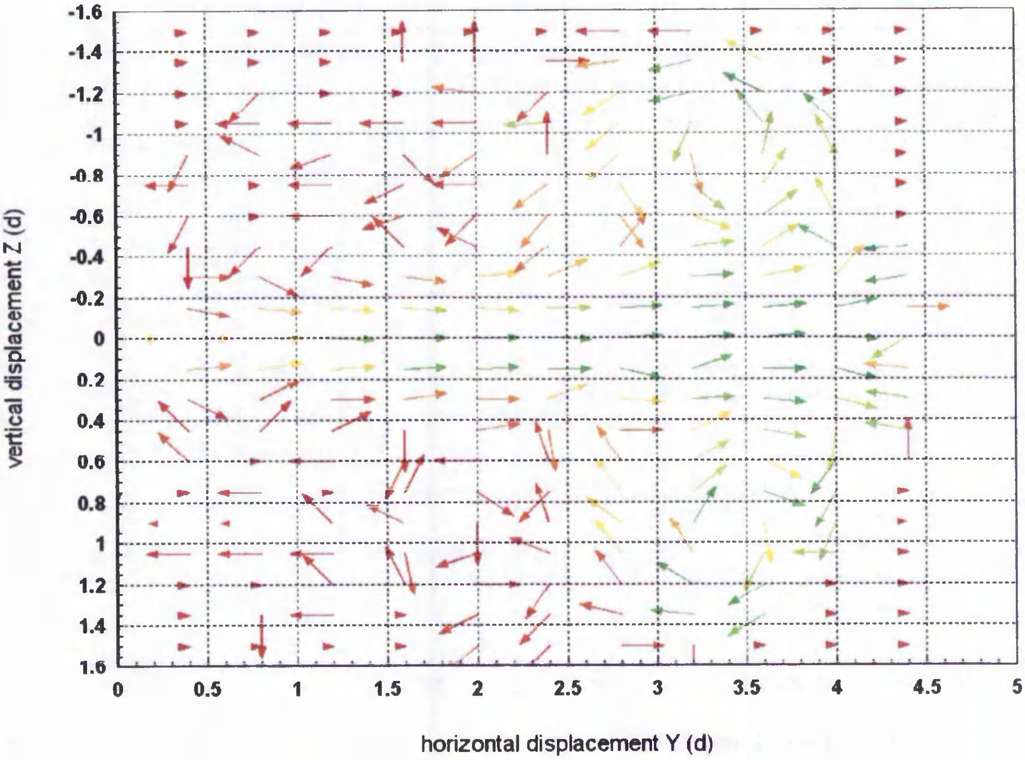

Figure 4-41 Pulsatile torsional full-field flow, YZ vertical plane, angle bin 288

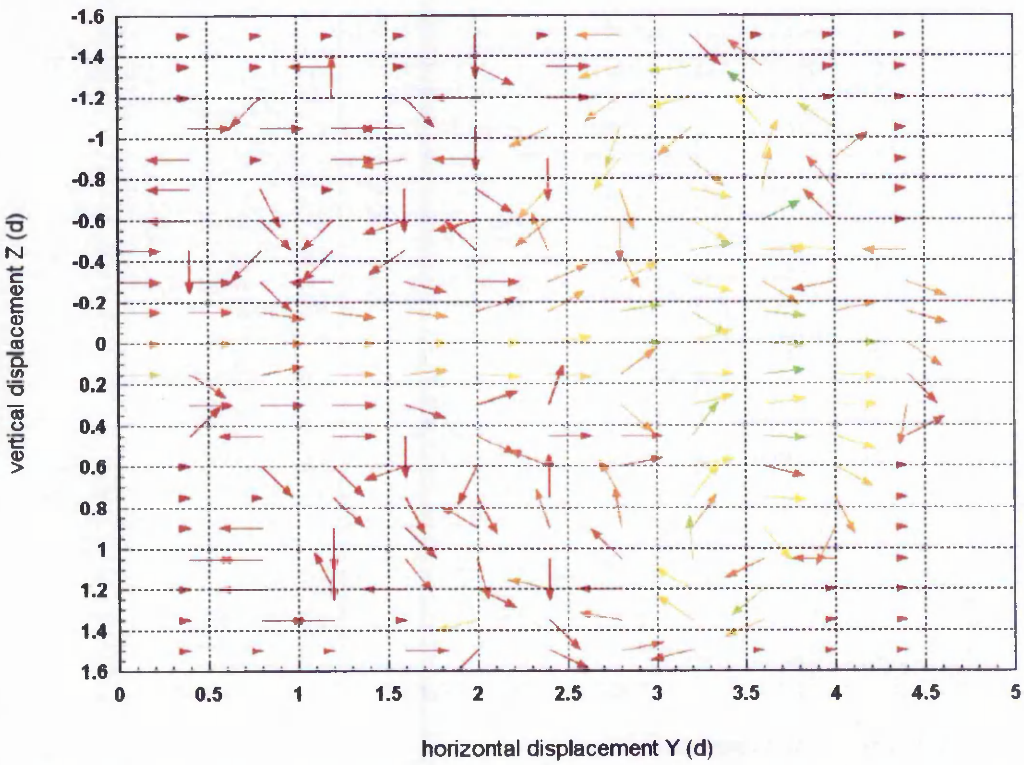

Figure 4-42 Pulsatile torsional full-field flow, YZ vertical plane, angle bin 342

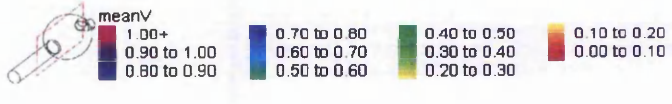

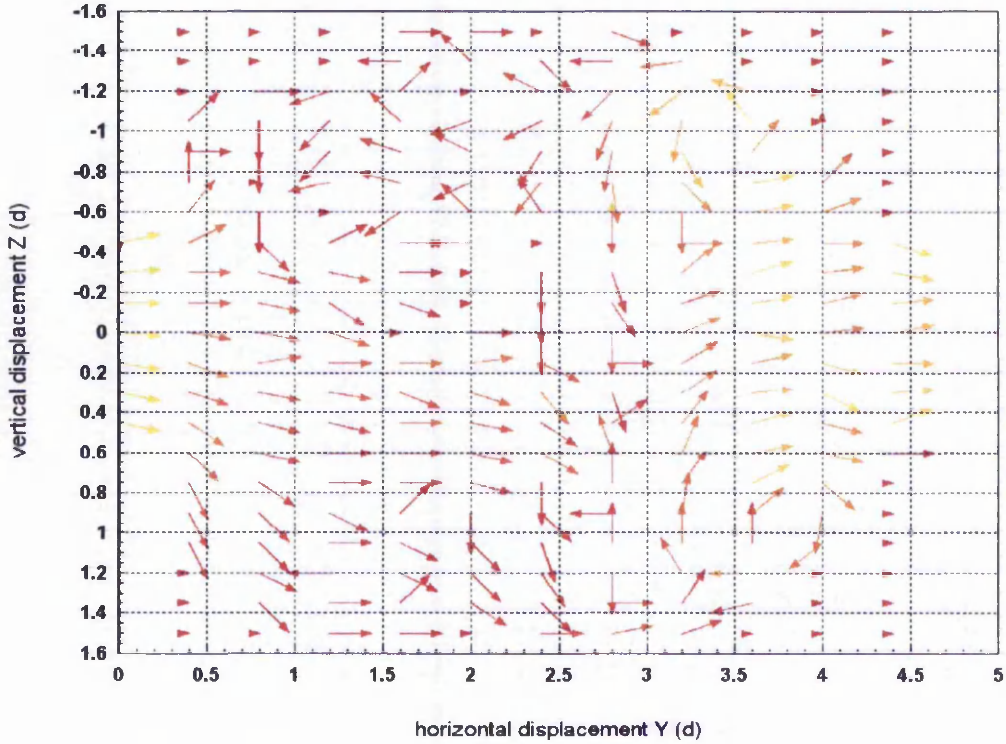

Figure 4-43 Pulsatile torsional full-field flow, YX horizontal plane, angle bin 18

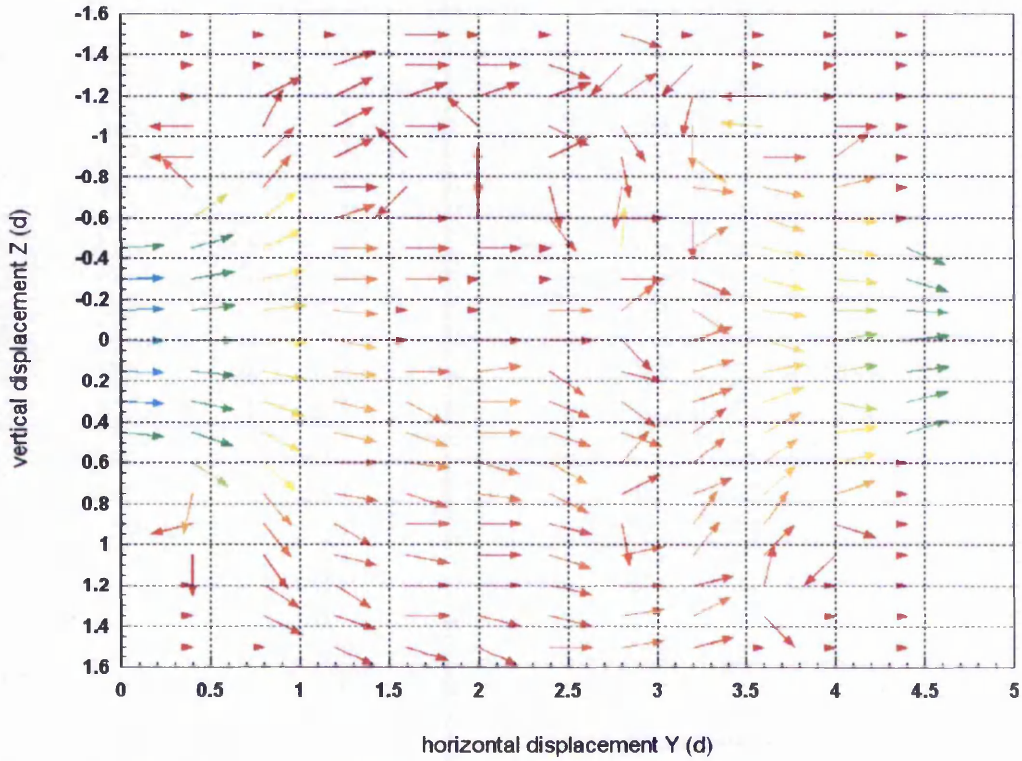

Figure 4-44 Pulsatile torsional full-field flow, YX horizontal plane, angle bin 54

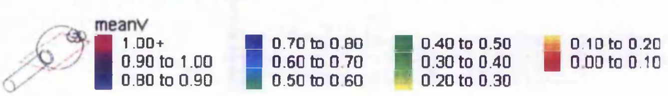

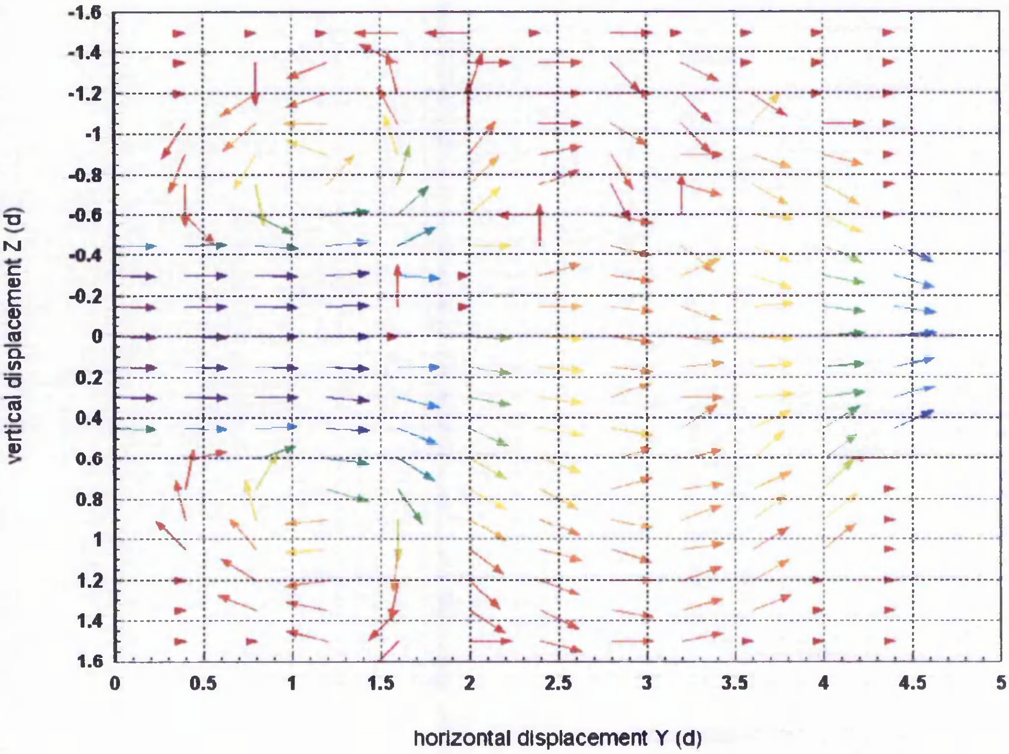

Figure 4-45 Pulsatile torsional full-field flow, YX horizontal plane, angle bin 108

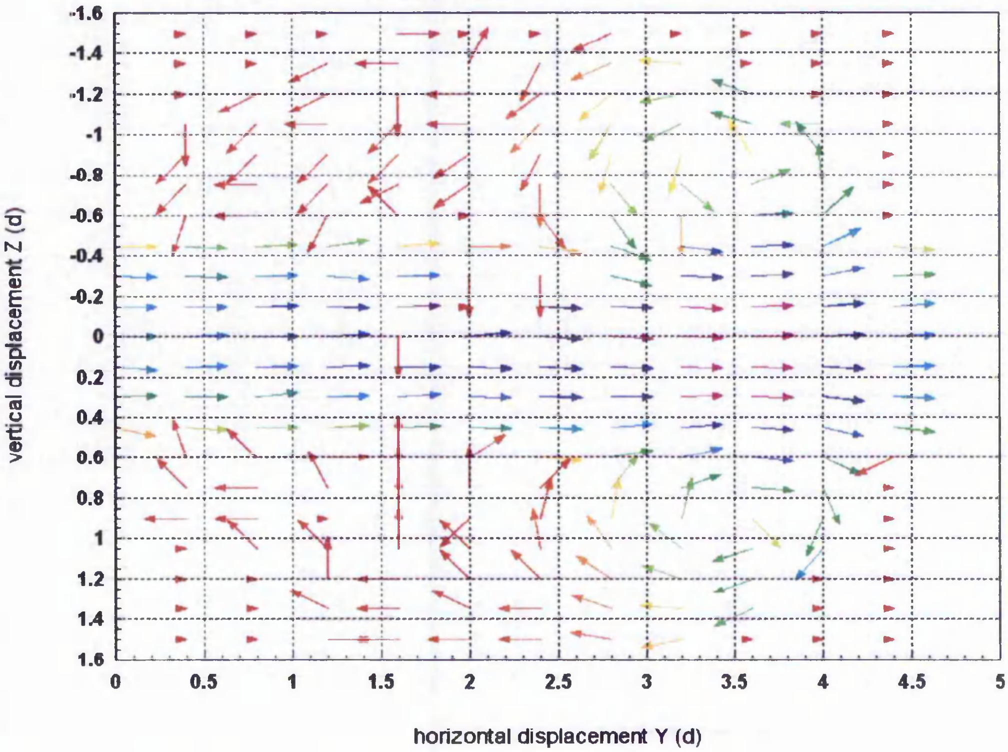

Figure 4-46 Pulsatile torsional full-field flow, YX horizontal plane, angle bin 198

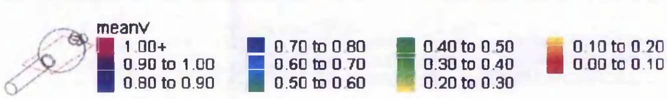

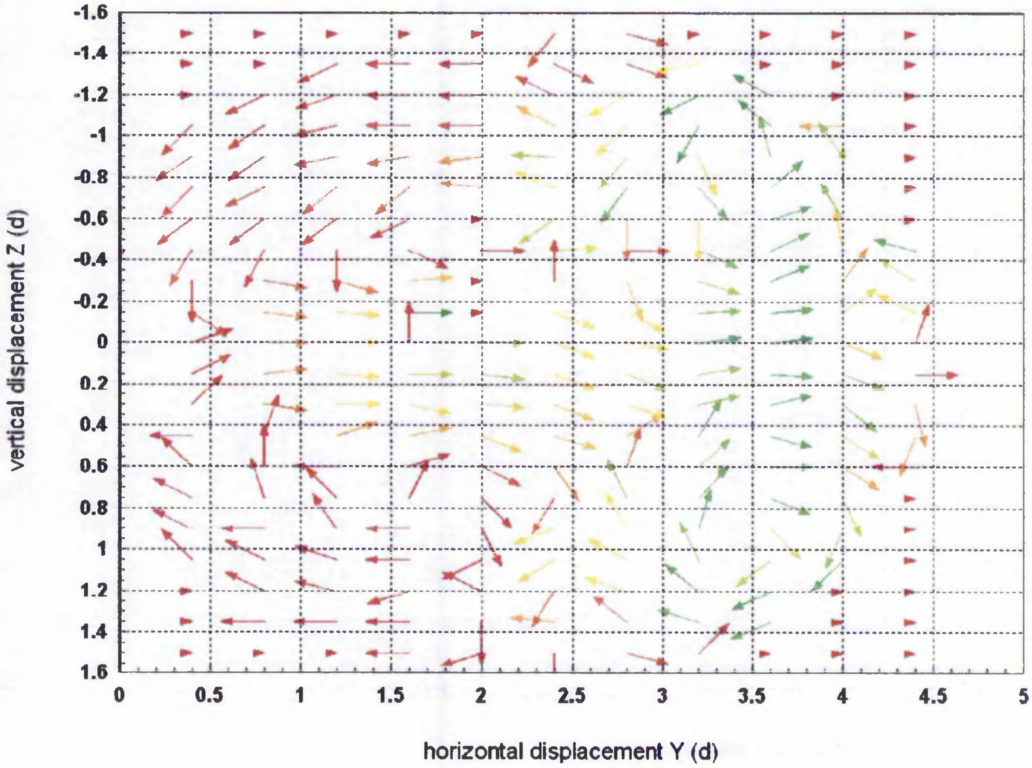

Figure 4-47 Pulsatile torsional full-field flow, YX horizontal plane, angle bin 288

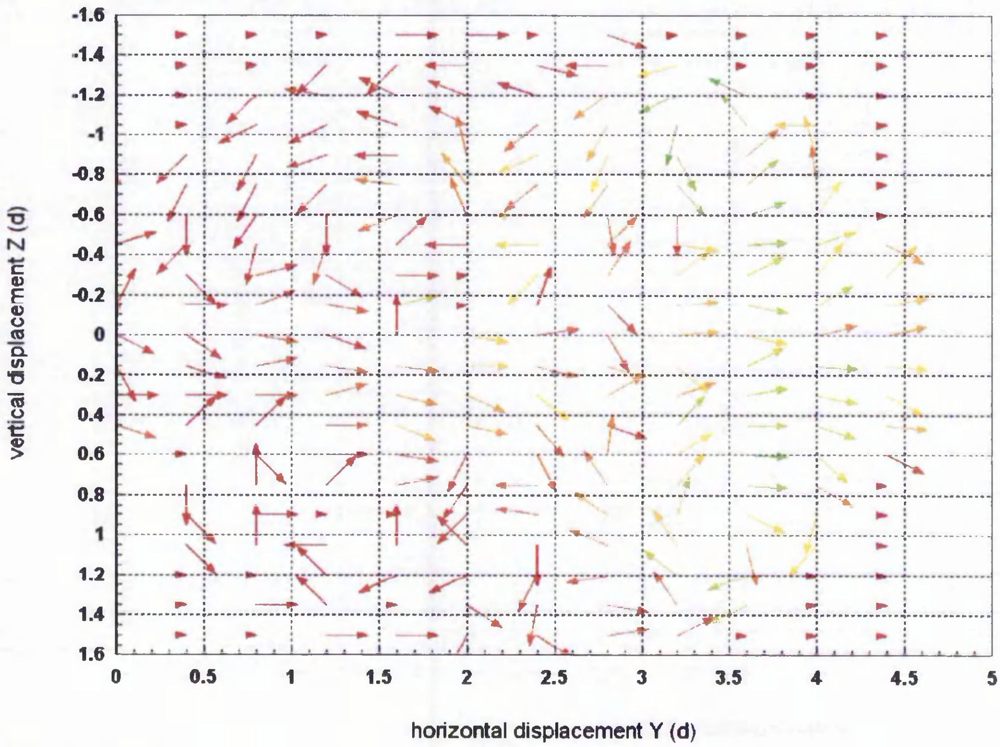

Figure 4-48 Pulsatile torsional full-field flow, YX horizontal plane, angle bin 342

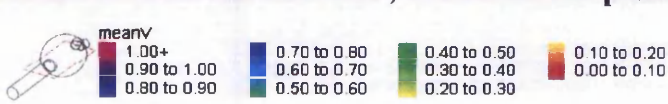

The general flow field seen for the pulsatile torsional flow conditions in each phase of the flow presented in the above figures is similar in characteristics to that detailed for the non-torsional inlet flow parameters (section 4.4.2), however, there substantial differences which will be expanded upon here.

In comparing the vertical profile cases of non-torsional and torsional inlet, for the preliminary phase of the pulsatile cycle (Figure 4-37), less defined recirculation was seen in the proximal end of the aneurysm. Although recirculations were seen distally they were not as pronounced in the torsional case. During systolic acceleration of the flow (Figure 4-38) the jet core was seen to expand more rapidly and the core expanded towards the dorsal section of the AAA. However, this was not as pronounced as that seen in the non-torsional inlet where this expansion seem almost fully attached to the wall. The expansion of the core to encompass the aneurysmal diameter occurred in peak systole (Figure 4-39). This took place almost halfway along the length of the aneurysm and more completely in the dorsal section of the bulge. In comparison with the non-torsional flow there were much greater regions of uncertain flow proximally to this region. Areas that showed low velocity and little uniformity in direction.

During the deceleration of the flow (Figure 4-40) the core of peak velocity had moved in a similar aspect to that seen in the non-torsional inlet model. However, the velocity distributions along the core length were more even in the case of the non-torsional inlet. In the torsional model flow was seen to have a much lesser velocity than the peak seen in the model; this differential taking place over less than 1 diameter. The vortices seen distally in the model did not encompass the entirety of the aneurysmal bulge as was the case in the non-torsional inlet. The effects of the torsion were to create a much more localised effect upon the flow field whereas in the non-torsional inlet model the recirculation extended distally to the inlet. The centres of the vortices were also approximately central at 2.5-3d into the aneurysm. In the torsional model the vortices were located ~3-3.5d into the geometry. Also it is worth noting that the flow was less symmetrical and the ventral vortex occurred more distally to that seen in the dorsal regions.

In the later stages of the pulsatile cycle (Figure 4-41) the flow was seen to be approximately axisymmetric with regions of even recirculation in both ventral and dorsal sections of the aneurysm. However, in comparison with the non-torsional inlet flow case, the flow became more rapidly chaotic with barely defined regions of recirculation. By late diastole (Figure 4-42) the entirely of the flow field had degenerated into a mainly chaotic state which exhibited only barely defined vortices.

In comparing the horizontal flow field recorded for the non-torsional and torsional inlet, much greater distinction and be seen between the two inlet conditions. In early systole (Figure 4-43), once again, the flow was seen to expand more rapidly at the inlet, however a distinct asymmetric flow region was seen to begin development even at this preliminary time bin which was clearly expanding into one side of the aneurysm.

During systolic acceleration (Figure 4-44) the flow had expanded to encompass the majority of the aneurysmal bulge. This expansion was biased towards the right hand side of the aneurysm (traversing laterally into the geometry in the x plane). However, in the case of the non-torsional inlet (Figure 4-31) this filling of the aneurysm did not fully occur even at peak systole. There was a region of distinct uncertainty in the left hand sector of the aneurysm in this time phase in the torsional case; a region of chaotic flow that showed low velocities and no consensus of direction.

At peak systole (Figure 4-45) the flow had encompassed the majority of the aneurysm, maintaining a right hand sided bias, however, the positive direction of flow was no longer attached to the aneurysmal wall. This attachment only occurred 2d into the model, more than two-thirds along the entire length of the bulge. Proximally to this attachment areas of slow recirculation were seen to have developed. In the non-torsional flow case a similar attachment occurred, however, the positive flow was less distinct and the recirculation markedly less pronounced. During early diastole (Figure 4-46) very little right hand bias was seen in the model and the flow field can be considered to be mostly symmetrical. In comparison with the non-torsional flow case, the flow is also remarkably similar, potentially due to the lower rotational velocities at the inlet as the flow uniformly decelerated although the core flow was considered to be more expanded in the case showing inlet torsionality.

During late diastole (Figure 4-47 and Figure 4-48) the flow maintained its symmetry and similarities between the both non-torsional and torsional flow regimes remained unpronounced. However, there was a greater tendency for a more ordered recirculation towards the inlet in the torsional flow case. Any vortices remaining in the geometry at this late stage of the pulsatile cycle were noted to be localised in the non-torsional model.

4.6 Distal Wall Shear rate (WSRs)

Graphs of the WSR results are presented in a simple format in order to aid visualisation of the effect of torsion upon the velocity gradients measured at the wall.

Where relevant graphs are placed around the page representing the data taken at each point on the model. Steady flow data is represented in a simple scatter plot format and axes are scaled in an identical format for each dataset.

In the case of pulsatile flow, three-dimensional graphs are presented, showing the position of measurement downstream on the Y-axis and also the development of the forces gradients with time

4.6.1 STEADY FLOW NON-TORSIONAL INLET

The centreline WSR's were measured for the dorsal and ventral walls of the AAA in the normal geometry position.

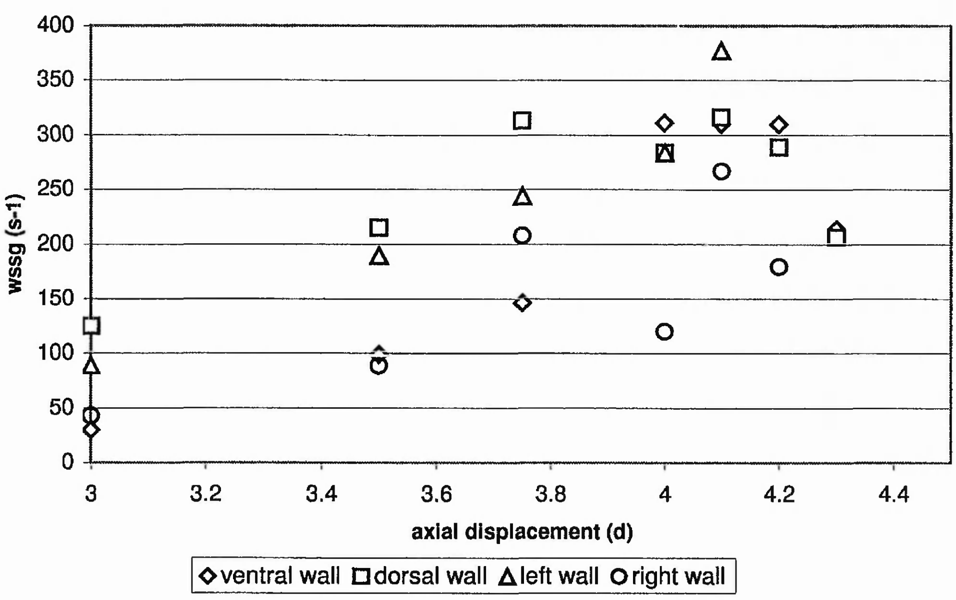

Figure 4-49 Scatter plot showing WSR's in steady flow, non-torsional inlet

Recorded WSRs in the non-torsional inlet model were shown to vary, perhaps due to inconsistencies in the inlet boundary conditions, however, the peak WSRs measured fall within ~15% of the average of recorded values. The trend shown in all plots show a consistent increase in WSR as the flow extends distally into the model until a peak at 4.0-4.2d and a steady decrease further towards the outlet. This was seen to be consistent with the vortices highlighted in the full-field flow data. Maximum-recorded WSRs were in the range of 275 to 375s^{-1} at this point.

4.6.2 STEADY FLOW TORSIONAL INLET

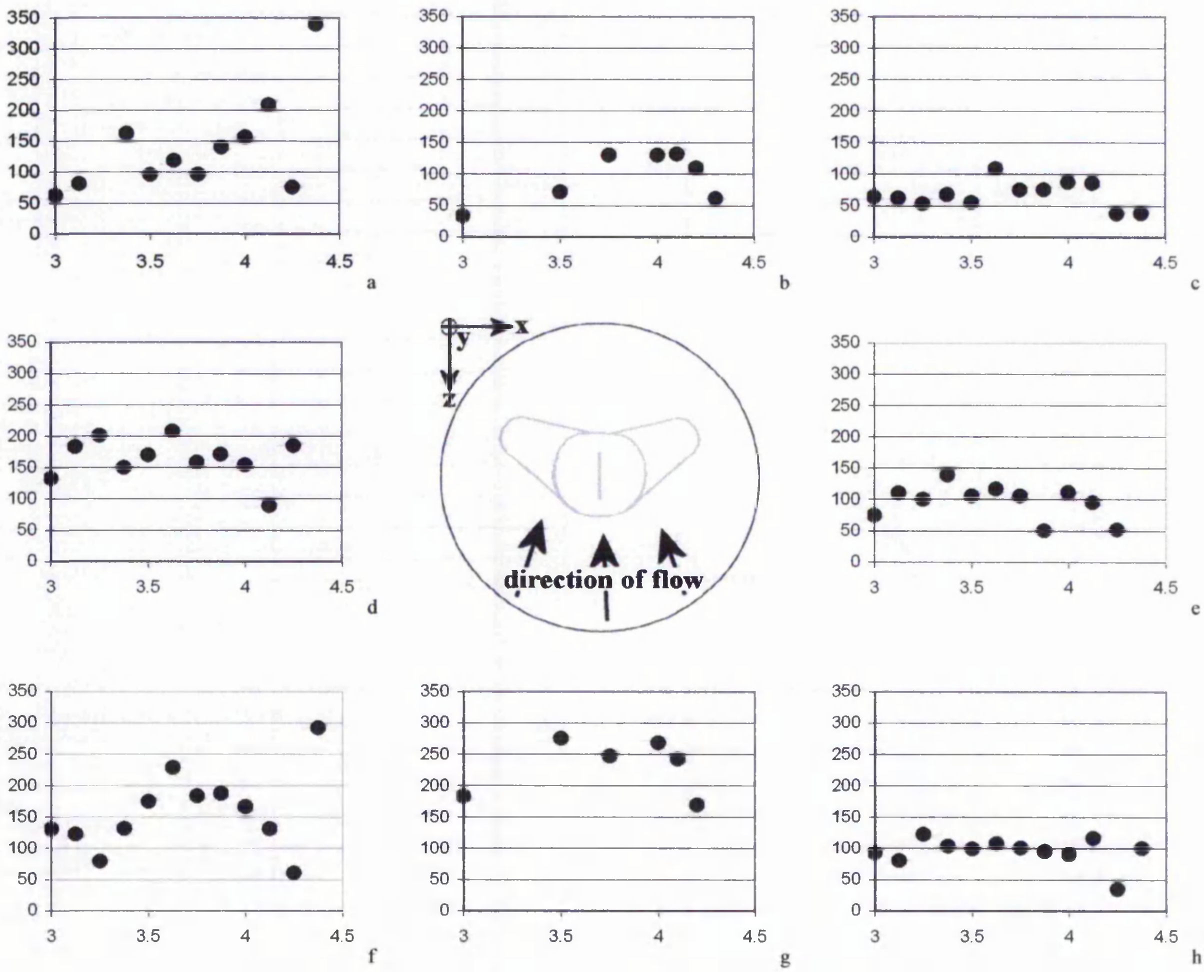

Figure 4-50 Distal WSR's in the steady flow, torsional inlet

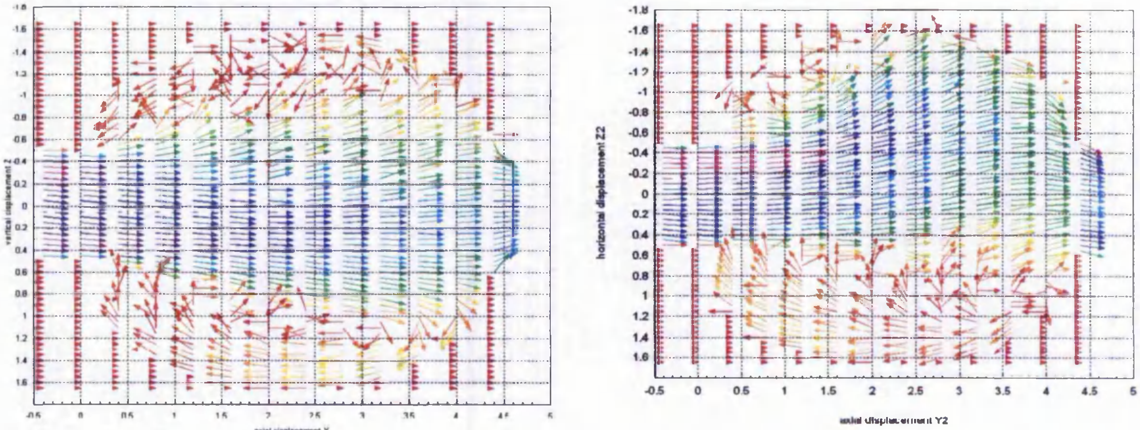

Velocity vector plot-a: vertical plane   Velocity vector plot-b: horizontal plane

Figure 4-51 Summary of steady flow field, torsional inlet

The WSRs depicted in Figure 4-50 are represented as modulus values calculated from the near-wall velocity profiles. The x-axis represents the axial location into the aneurysm (diameters, d) and the y-axis represents the magnitude of the WSR (s^{-1}). The graphs are placed in an array about the central diagram as to represent the position in which the measurements were taken.

a	-x –z diagonally left on the ventral wall
b	on the ventral wall of the model
c	+x –z diagonally right on the ventral wall
d	on the left hand wall of the vessel
e	on the right hand wall of the vessel
f	-x +z diagonally left on the dorsal wall
g	on the dorsal side of the model
h	+x +z diagonally right dorsal wall

It can be seen from the data that there is a distinct change in the WSR profiles experienced in each distal quadrant of the aneurysmal bulge.

The basic interpretation of results is consistent with those expected from observations of the velocity profile. WSRs on the right hand side of the model show uniformly low WSRs in relation to those on the opposite side. This can be attributed to the sweeping of the velocity core towards the left hand quadrant of the bulge that produced an impingement upon this wall. Furthermore, the velocity gradients were inline with the flow and are higher, as expected. On the right hand quadrant of the model wall shear was a result of a large vortex of recirculation, which passes fluid proximally towards the inlet. As can be seen from Figure 4-51b these velocities are considerably lower than those from the redirected core flow. Likewise, the flow against the dorsal section of the model was greater than that seen in the ventral sector. A high WSR was maintained further distally in the lower section, as there was a powerful recirculation that can be seen to extend throughout the entire length of the aneurysmal bulge (Figure 4-51a).

In cases representing a recirculation encompassing the entire of the bulge WSRs are maintained at a relatively high level throughout the distal end. The loss of defined recirculation in the ventral section of the aneurysm produced a WSR that peaked at the maximum velocity of the vortex and dropped rapidly with the onset of chaos in the flow.

The sweeping flow dominating the left hand sector of the model produced uniformly high WSRs, which first peak as the flow impinges on the wall, and drop as the flow decelerates as it extends distally, however acceleration is seen as the flow exits the aneurysm that is apparent in Figure 4-50a, d and f which show a leap in WSR shortly before the vessel outlet. It is at this point that recorded WSRs are a their peak of $300\text{-}350s^{-1}$. However, WSS values of this magnitude were measured in the non-torsional model. Perhaps more importantly the change in wall shear stress experienced at the vessel wall fluctuates from $\sim 75s^{-1}$ to $\sim 325s^{-1}$. This tripling of value within 0.25d is something not seen in the non-torsional model. In this manner the ventral section of the AAA is also subject to the greatest change in WSR. In these experiments it can be seen that the ventral section of the model experienced consistently mediocre WSRs. Peaking at $\sim 150s^{-1}$ and falling at the distal end of the bulge. At 4.3d the recorded WSR was $<70s^{-1}$. However, in the adjacent quadrant a WSR approaching $350s^{-1}$ was recorded.

4.6.3 INTRODUCTION TO PULSATILE WSR RESULTS

Due to difficulties of presentation, the axis labelling of graphs in Figure 4-57 have been omitted and are better highlighted below in Figure 4-52.

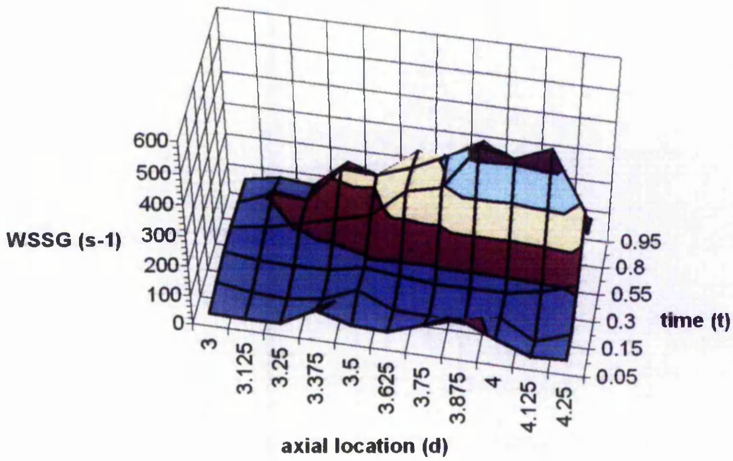

Figure 4-52 Sample graph of WSR showing axis and scaling

The x-axis shows the axial location of the measurement, measured from the inlet and then distally in diameters (d). Full aneurysmal length was 4.4d. Measurements were only taken in the distal sector of the aneurysm in regular intervals until the outlet was reached. The y-axis shows the time frame in which the measurements were taken. Each angle bin represented $1/20^{th}$ of the cycle. For the purposes of this experiment the angle bins were then normalised where t=0.7s. Angle bins utilised were 18, 54, 108, 198, 288 and 342 (where the full time frame was 360). Normalised these times were 0.05, 0.15, 0.3, 0.55, 0.8 and 0.95t. In the graphical representation used, the development of WSRs can be viewed along the x-axis in order to ascertain the WSR along the AAA wall at a point in time. Along the y-axis is clearly shown the WSR dynamic over the pulsatile cycle for a local point on the aneurysmal wall. WSR is represented on the z-axis in s^{-1}.

4.6.4 PULSATILE INLET WALL SHEAR RATE MEASUREMENTS.

For purposes of comparison, WSR measurements were taken proximally in relation to the inlet of the AAA. This would equate to WSRs found within the healthy aorta and have value for comparison relative to those measured within the distal region of the aneurysm.

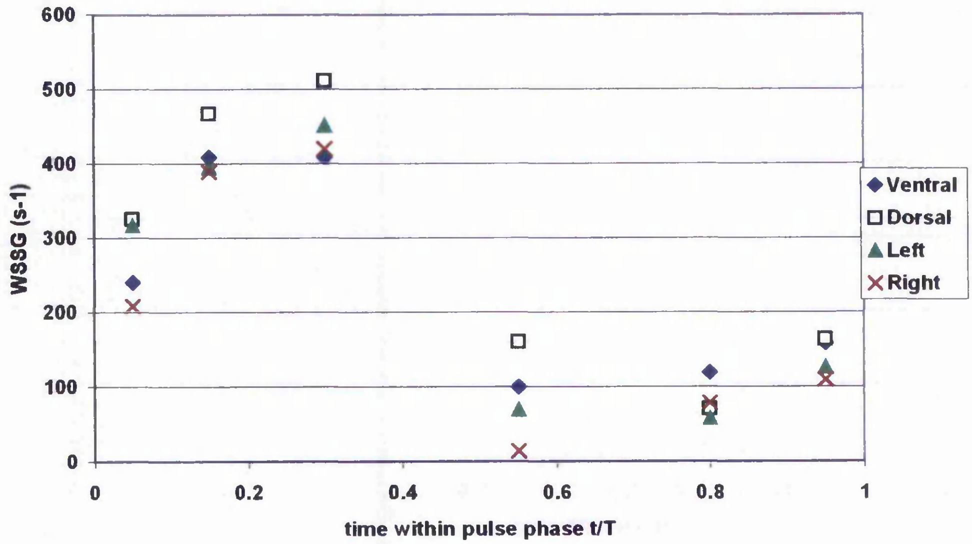

Figure 4-53 Magnitude of Aortic WSR proximal to Aneurysmal Bulge

Figure 4-53 shows the calculated WSRs throughout the pulsatile cycle at four points around the wall of the vessel. All areas of measurement show an identical trend in results. However, those taken on the right hand side of the vessel show consistently lower values of wall shear stress. This is consistent with the full field cross-sectional measurements showing lower inlet velocities on the right hand side of the artery in *section 4.3.1.*

4.6.5 PULSATILE FLOW, NON-TORSIONAL INLET

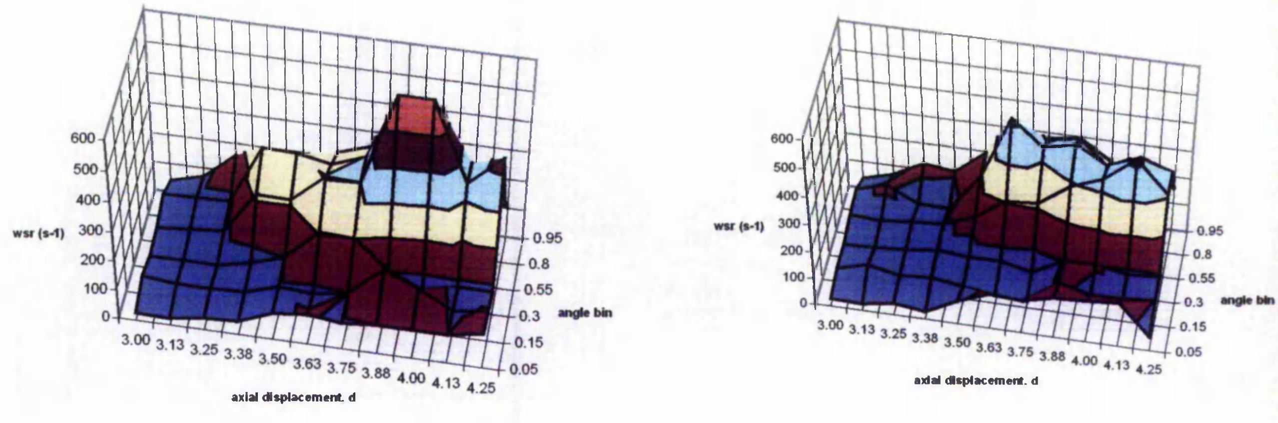

a b

Figure 4-54 Graphs showing distal WSR in the vertical plane (-z and +z respectively)

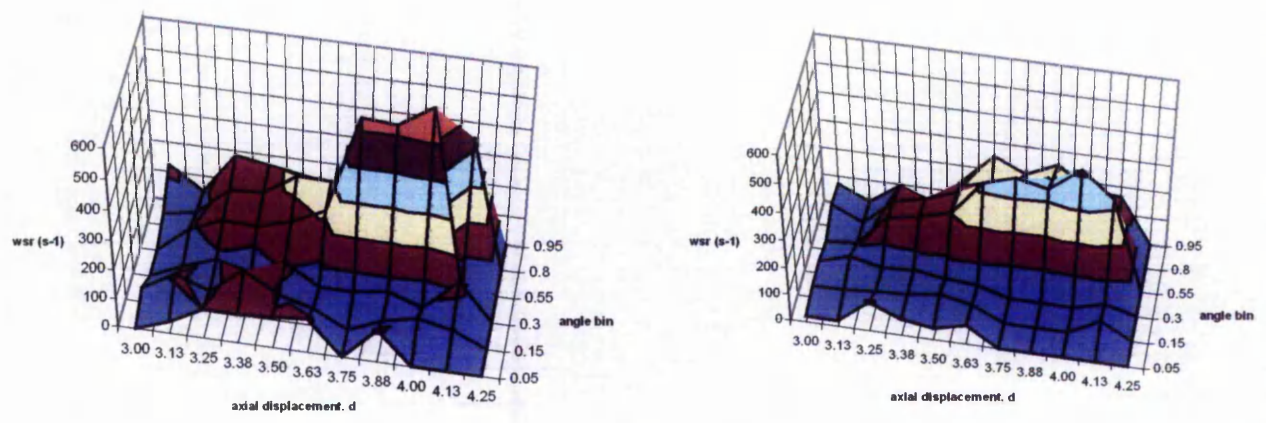

a b

Figure 4-55 Graphs showing distal WSR in the horizontal plane (-x and +x)

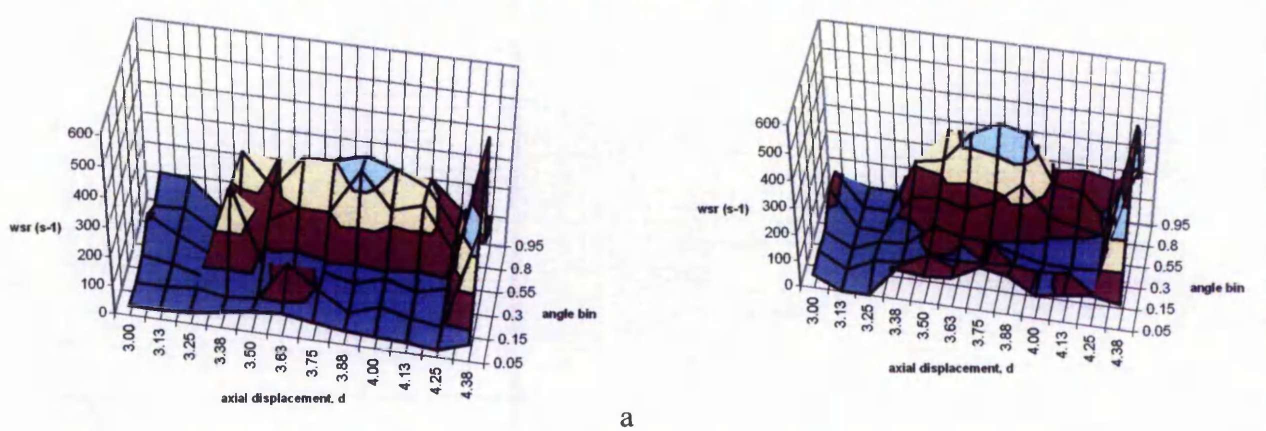

a b

Figure 4-56 Graphs showing distal WSRs in diagonal planes -x +z and –x-z

4.6.6 PULSATILE FLOW, TORSIONAL INLET

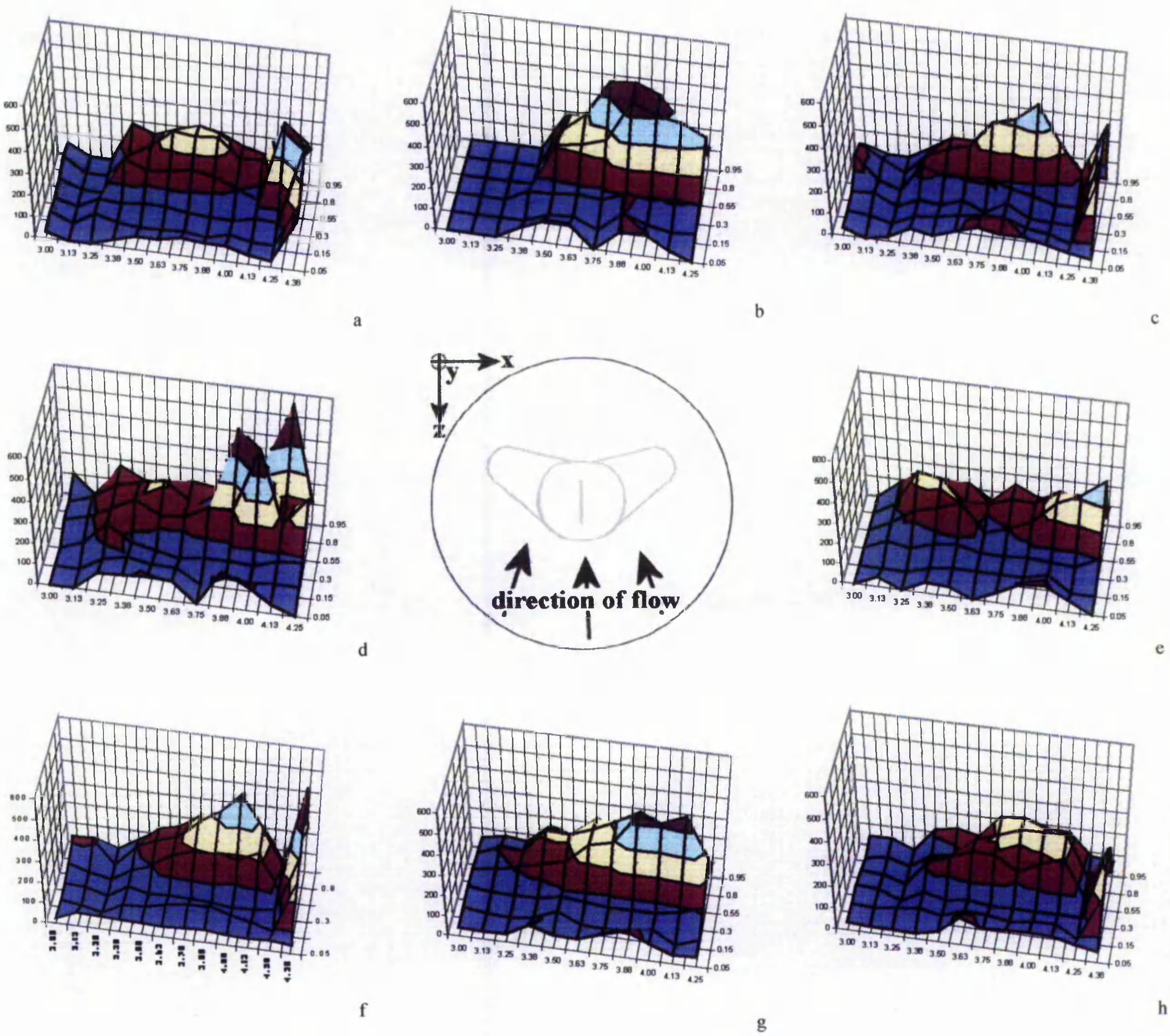

Figure 4-57 Distal WSS graphs due to pulsatile torsional inlet

As in Section 4.6.3 the graphs are arranged in the following manner. The WSRs depicted in Figure 4-57 are represented as modulus values calculated from the near-wall velocity profiles. The scaling and labelling of these graphs has been explained in 4.6.3. The graphs are placed in an array about the central diagram as to represent the position in which the measurements were taken:

a -x –z diagonally left on the ventral wall b on the ventral wall of the model

c +x –z diagonally right on the ventral wall

d on the left hand wall of the vessel

e on the right hand wall of the vessel

f -x +z diagonally left on the dorsal wall

g on the dorsal side of the model

h +x +z diagonally right dorsal wall

4.6.7 Discussion of Distal WSR Results

The non-torsional inlet results (Figure 4-54, Figure 4-55 and Figure 4-56) show a variation in peak WSRs measured between 450-550s^{-1}. Regions of high WSR were seen in each graph between 3.2d and 4.2d. Universally throughout the graphs a rapid decrease in WSR was seen as one approaches the outlet. Rapid increases in WSR in Figure 4-56 at the distal end of the AAA can be attributed to the exit of fluid from the model. Centralisation of WSR was seen in each graph at 3.88d. However, a variation in the WSR measured in Figure 4-55 can be attributed to a variation in the flow field seen in Figure 4-32. During late systole it was demonstrated that this flow exhibited asymmetry and recirculating vortices were offset from one another by as much as 0.5d. This was due to experimental error in the non-torsional inlet boundary conditions. However, it demonstrates the variation and sensitivity of measured WSRs with respect to inlet boundary conditions.

The distal WSRs measured using the pulsatile-torsional inlet boundary conditions showed a distribution of WSR throughout the aneurysmal model. In correspondence with the steady flow results, WSRs were relatively lower on the right side of the model, although this decrease was skewed towards the right-dorsal quadrant. Where peak WSRs were measured below $250s^{-1}$ the plateaux of the graphs were broad (Figure 4-57a and h). In regions demonstrating greater WSRs the peaks were marked and steep. Peak WSRs were measured predominantly in the dorsal-left quadrant of the AAA and in the central-ventral region. Maximum WSRs measured were between $400\text{-}500s^{-1}$. Rapid increases in WSR due to acceleration of the flow near the outlet were seen in all diagonal profiles as they extended further towards the outlet. The greatest WSR due to this acceleration was measured in the left-dorsal quadrant of the model. Excluding this distal increase in WSR each WSR peak decreased towards the proximal end of the bulge with the exception of the central-right WSR profile which produced consistently lower WSR values until a gradual increase towards the outlet inline with WSR expected at the exit.

WSRs seen in the distal section of the AAA were seen to vary and hit peaks 20% higher than those seen in a healthy vessel. The calculated maximum WSR at the inlet was between approximately 400 and $500s^{-1}$. Importantly though the wall of the entrance vessel undergoes regular and moderate WSRs at systolic parts of the pulsatile cycle. In the distal region of the AAA, however, are contained areas that exhibit no WSRs over $100s^{-1}$ at any point throughout the cycle.

CONCLUSIONS AND FURTHER WORK

5.1 Full Field steady flow

The results presented in sections 4.4.2 and 4.5.2 clearly demonstrate the change in the flow field due to introduction of torsionality in the inlet boundary conditions. The major considerations concerning this are the expansion of the jet core, the impingement of the inlet velocity core upon the distal wall and the dynamic changes in the presence and appearance of recirculation vortices.

In the horizontal plane the jet is both expanded due to inlet torsionality and made to impinge upon the left wall of the aneurysmal bulge. This omits any possibility of flow stagnation in this region under any but extreme circumstances. In the model studied there was a small region of flow recirculation located proximally on this side of the aneurysm. However, it was considered that the curvature of the aneurysm used in these studies was of a magnitude representing a maximal case of aneurysmal bulge. In geometry of a smaller dimensional ratio (D/L) it is likely that the flow skewed to the left of the aneurysm would remain attached to the wall. Due to this sweeping flow on the left of the aneurysm powerful flow recirculation completely dominated the flow field on the right of the model.

In the vertical plane, comparing torsional to non-torsional inlet conditions, velocity core expansion was more complete although there was a dorsally skewed trend in the flow. Once again in the dorsal quadrant of the model a single powerful vortex was created that left little room for proximal regions of uncertain and stagnated flow. In the ventral region an area of stagnation was seen. Once again in a model of decrease bulge diameter the expanded jet core would impinge upon the wall at a greater velocity and more pronounced recirculation would occur. However, whilst it cannot be concluded that the presence of torsionality in this model eliminates zones of flow stagnation, it has been clearly showed that the nature of inlet torsionality describes larger, more sweeping vortices, which will reduce the occurrence of low wall shear, associated with clotting plaque build-up.

Furthermore in a more complex geometry it would be suitable to study an inlet jet that is directed dorsally into the aneurysm, naturally impinging upon the distal wall. In an impinging-jet, wall shear is considered detrimentally higher than that seen due to wall recirculation. Seen in the non-torsional flow model, core velocities were maintained to within 95% of their inlet values that would undoubtedly cause unreasonable stresses to the distal wall. Inlet torsion induced an expansion of the velocity core to approximately twice its original non-torsional cross-section and as such distal core velocities were seen to drop to between 40% and 60% of the inlet maximum (vertical and horizontal planes respectively). Such dramatic deceleration would have beneficial effects upon the stresses due to jet impingement. However, deceleration of bulk flow and re-acceleration at the outlet in any closed pressure driven flow system causes a loss of pressure. Therefore, in either experimental or numerical studies of aneurysmal flow systems it is recommended that inlet torsionality be accounted for in a physiologically representative model.

5.2 Full Field Pulsatile Flow

Effects of inlet torsion upon the pulsatile flow-field are less marked. This was due to the inlet boundary conditions applied. Due to the very nature of the inlet pulsatility, torsional characteristics of the flow were seen to be not as developed in comparison with steady flow inlet conditions. Maximum rotational velocities measured in the steady flow studies were 0.25 of the axial inlet velocity and considerable flow rotation was seen. In the pulsatile case maximum inlet rotation was 0.07 and 0.04 of the inlet velocity in vertical and horizontal profiles respectively, less than a third of the rotational velocity seen comparative to the steady flow inlet. However, it is worth noting that during diastole, in both planes of rotation, the transverse velocities measured were clearly disordered. This was most markedly seen in the vertical plane, which exhibited the greatest torsion. During this deceleration velocity values were measured at 0.15 of the inlet maximum, twice that of the maximum rotation seen at peak systole.

Also due to the time-dependency of the flow, axial velocity profiles did not develop in the same way that is seen or occur in steady flow models. In both planes horizontal and vertical planes the inlet profiles throughout the pulsatile cycle were blunt and plug-shaped, more so than the semi-developed profile used in these studies involving steady-flow. Previous literature of both experimental and numerical investigations has been studied and in the majority of cases fully developed Poiseuille flow is used to represent inlet boundary conditions. From the inlet graphs shown it is clear that the torsional aspect of the flow presents a broader, flatter lead velocity profile than seen in the non-torsional inlet model. During flow deceleration little skewness was seen in the boundary profile with the exception of early diastole in the horizontal plane where the velocity around the outside of the aortic arch was seen to decelerate more rapidly that on the inside of the curvature. Although effects of torsion on the inlet are minimal in comparison with the steady flow case, this lends credence to the use of a blunted, non-developed inlet boundary in both experimental and numerical models, even if torsionality if omitted.

Due to this lack of developed inlet profile and limited rotation, the aneurysmal flow field was not dramatically affected as seen in the steady flow modelling. The flow field maintained a symmetrical appearance throughout the pulsatile cycle. However, the expansion of the jet core produced a more marked increase in its cross-sectional area and as such the forward sweeping velocities encompassed a greater section of the aneurysmal bulge than those seen in the non-torsional model. This dynamic expansion also created proximally located zones of recirculation in the horizontal plane during peak systole (Figure 4-45). Although this can be seen in the non-torsional model to some degree, the maturing of this vortex is far great in the torsional model. This proximal region is notoriously prone to low shear and flow stagnation that can induce clotting and thrombus formation. In an aneurysmal geometry such as this, the recirculation due to inlet torsionality would beneficially inhibit such a stagnant region from forming. Further observations seen in the torsional flow field are the more distally located vortices. Whereas in the vertical plane of the non-torsional model the centres of recirculation in both ventral and dorsal quadrants of the aneurysm are almost located centrally within the model, these are displaced distally in the experiments including inlet torsion, which once again affects both the flow field and WSRs induced by near wall velocities.

5.3 Steady Flow Distal Wall Shear Stress Gradients

Due to the gross changes in the flow field it is clear that in steady-flow studies the omission of inlet torsionality greatly misrepresents the distribution friction forces upon the wall. It is also apparent that although forward sweeping velocities are accountable for moderate wall shear stresses, the greatest WSRs were measured during flow reversal due to flow recirculation.

The magnitude of WSRs measured was affected by inlet torsionality. Although it would be expected that approximate gradients of $300s^{-1}$ be distributed around the aneurysmal bulge, there was a maximal WSR measured in the torsional model of $270s^{-1}$ in the dorsal section of the aneurysm. Wall shear around the remainder of the model was less than this value. This could be due to a loss of energy in the flow due to deceleration in the model. However, one could hypothesise that there is a WSR maximum in the left-dorsal region of the aneurysm that is unmeasured in these experiments. Therefore it is inconclusive as to whether the maximal WSR induced on the wall is lessened by inlet torsionality. If this is the case, however, it is only by ~10% of that seen in the non-torsional model.

5.4 Pulsatile Flow Distal Wall Shear Stress Gradients

Although it has been noted that gross changes in the flow-field were not apparent due to inlet torsionality in the pulsatile experiments, trends were seen analogous to those of the steady flow in that points of high WSR were measured in the left-dorsal region of the aneurysm. Maximal WSR values measured in the model were decreased due to the inclusion of torsionality by 30% or more in certain distal locations and WSRs measured elsewhere in the aneurysm were considerably lower than those measured in the model omitting inlet torsion.

As has been noted in previous literature maximal WSR values have increase by 100% due to the pulsatility of the flow further showing that in the calculation of forces acting upon the vessel wall, the limitations of time-independent flow consistently underestimate these wall shear gradients.

Due to the consistently moderate WSRs measured proximally in the aneurysmal model, even during peak systole, it is concluded that vortices of recirculation are the predominant cause of wall shear and that as such the effect of inlet torsion upon the distribution of such vortices should not be discounted in near wall measurements.

5.5 Concluding Remarks

Taking into account these observations it is clear that in the study of both full-field flow and detailed wall shear stress analysis, inlet torsionality has been demonstrated an effect upon distal flow regimes.

This is especially relevant during the study of exercise conditions and high flow rates within the vascular system. However, it is considered that the case for inclusion of inlet torsionality is decreased in circumstances of low flow rates. This is due to the limited development of flow rotation in the flow parameters used in these experiments.

Also it is uncertain at this time whether the elastic nature of the wall would decrease the effects of expression of flow torsionality so far into the abdominal aorta. However, the literature shows rotational flow has been demonstrated in the abdominal aorta through *in vivo* measurements. However, the degree to which this rotation occurred was undocumented.

Through the course of these experiments is has been apparent that WSRs are highly susceptible to variations in flow recirculations and associated near-wall flow-rates. Variation was seen in the non-torsional experiments involving both pulsatile and steady-flow for which experimental error alone could not account.

It is assumed that future researchers conducting experiments in this field would consider the inclusion of inlet torsion on the merits of such work conducted here. In the study of steady flow the effects of inlet torsion cannot be discounted as the resultant swirl imparted to the flow is at a maximum. Most especially in flows exhibiting high Reynolds number, the torsionality has sufficient scope in which to fully develop as the frequency and flow rate is sufficiently great enough to allow the torsion of arch flow to be maintained until the descending aorta.

For pulsatile flow, because the effects are less pronounced it may be possible to omit flow torsion for basal flow rates exhibiting low Reynolds number, however, in flows such as those studied here flow torsion had measurable consequences to both flow fields and wall shear forces. Also in exercise haemodynamics, the contraction of the left ventricle takes place over a longer time frame, further inducing the effects of curvature upon the flow. From this it one can conclude that in a highly detailed studies of aneurysmal haemodynamics it would be unwise to discount inlet torsionality due to the presence of the three-dimensional curvature of the aortic arch.

5.6 Recommendations for Further Work

The future of work investigating aneurysmal haemodynamics in the abdominal aorta is the pursuit of more accurate and representative modelling of the geometry. Although the actual geometry of occurring AAA's is infinitely varied, there are considerations omitted from this and other studies documented in literature.

The effect upon distal flow regions of the renal arteries has been concluded as being minimal by some researchers, however; the presence of branching arteries in the aortic arch has been documented as having distally relevant effects. As such these, and the mass flow lost through these junctions should be included in further studies of the aortic arch.

Certain properties of the aorta were omitted due to factors discussed earlier in this thesis. The tapering and elasticity of the aorta were excluded, however, in near wall flow analyses it would be prudent to include this information. However, as this time there is a paucity of accurate and representative data for elastic wall properties in an AAA. This is partially due to the unpredictable occurrence and effects of atherosclerotic lesion in the aneurysmal bulge.

The effects of atheroma in the aneurysm are required for a more detailed study of aneurysmal haemodynamics. A build up of this substrate would affect both the volume of the aneurysm and the flow regimes occurring within. However, the cataloguing of such effects is, at this time, rarely discussed in either numerical or experimental studies.

Although it is difficult to assume a stylised geometry for the study of aneurysm a predominant feature seen in many fusiform aneurysms is a non-centralised inlet, which is seen to impinge upon the dorsal wall of the geometry. As studies become more detailed, such inlet conditions should be included. It is also worthy to consider aneurysms of asymmetric design. More representative of those examined *in vivo*. However, the variation of such is limitless and difficulty has been shown in designing a representative geometry of this disease that shows such random characteristics.

With regard to the inlet boundary conditions, it would be worthy to study the effects of torsionality with laminar flow and lower Reynolds numbers. The parameters chosen in this study were used to exemplify the manifestation of inlet torsionality. Further work in this particular field of study should inlet lower, basal flow rates using resting cardiac profiles. Conclusive evidence of flow rotation should also be demonstrated in the human abdominal aortic to greater or lesser degrees through *in vivo* experimentation. Such a study should include a variety of flow conditions such as resting and a range of higher flow rates induced by exercise.

APPENDIX A - REFERENCES

Literature

Asbury, C. L., Ruberti, J. W., Bluth, E. I. and Peattie, R. A., 1995. Experimental Investigation of Steady Flow in Rigid Models of Abdominal Aortic Aneurysms, *Annals of Biomedical Engineering*, **23**, 23-39.

Back, L. H. and Crawford, D. W., 1992. Wall Shear Stress Estimates in Coronary Artery Constrictions, *ASME Journal of Biomechanical Engineering*, **114,** 515-520.

Baldwin, J. T., Deutsch, S. and Petrie, H. L., 1993. Determination of Principal Reynolds Stresses in Pulsatile Flows After Elliptical Filtering of Discrete Velocity Measurements, *ASME Journal of Biomechanical Engineering*, **115**, 396-403.

Beattie, D., Xu, C., Vito, R., Glagov, S. and Whang, M. C., 1998. Mechanical Analysis of Heterogeneous, Atherosclerotic Human Aorta, *ASME Journal of Biomechanical Engineering*, **120**, 602-607.

Biophotonics International, 1998. Laser imager used to visualise blood flow, *A Laurin Publication*, **5**(2), 56-57.

Black, M. M., Hose, D. R. and Lawford, P.V., 1995. The origin and significance of secondary flows in the aortic arch. *Journal of Medical Engineering and Technology.* **19** (6), 192-197.

Caro, C.G., Doorly, D.J., Tarnawski, M., Scott, K.T., Long, Q. and Dumoulin, C.L., 1996. Non-planar curvature and branching of arteries and non-planar-type flow. Proc. R. Soc. Lond. A 452:185-197

Cavalcanti, S., Bolelli, P. and Belarinelli, E., 1992. Pressure Drops Through Arterial Stenosis Models in Steady Flow Condition, *ASME Journal of Biomechanical Engineering*, **114**, 416-418.

Chandran, K. B., 1993. Flow Dynamics on the Human Aorta, *ASME Journal of Biomechanical Engineering*, **115**, 611-616.

Chong, C. K., Rowe, C. S., Sivanesan, S., Rattray, A., Black, R. A, Shortland, A. P. and How, T.V, 1999. Computer aided design and fabrication of models for in vitro studies of vascular fluid dynamics, *Preceedings of the Institute of Mechanical Engineers,* **213**(H), 1-4.

Daisuke Mori and Takami Yamaguchi (2001). Computational Mechanical analysis of blood flow in the human aortic arch with complex 3-d configuration- a combined effect of the torsion of the aorta and its branches, *ASME Bioengineering Conference*, **BED-Vol. 50.**

Darlin, R. C., 1970. Ruptured Arteriosclerotic Abdominal Aortic Aneurysms; a pathologic and clinical study, *The American Journal of Surgery*, **119**, 397-401.

Davies, P.F., DePaola, N., and Polacek, D.C., 1998. Hemodynamic Forces and Vascular Cell Communication. *Atherosclerosis XI*, 943-948.

Dean, W.R., 1927. Note on the motion of fluid in a curved pipe. Phil. Mag. **4**: 208-223.

Egelhoff, C. J., Bugwig. R. S., Elger, D. F., Khraishi, T. A. and Johansen, K. H., 1999. Model studies of flow in abdominal aortic aneurysms during resting and exercise conditions. *Journal of Biomechanics*, ***32***, 1319-1329.

Elger, D. F., Blackketter, D. M., Budwig. R. S., and Johansen, K. H., 1996. The Influence of Shape on the Stresses in Model Abdominal Aortic Aneurysms, *ASME Journal of Biomechanical Engineering*, **118**, 326-332.

Fatemi, R. S. and Rittgers, S. E., 1994. Derivation of Shear Rates From Near-Wall LDV Measurements Under Steady and Pulsatile Flow Conditions, *ASME Journal of Biomechanical Engineering*, **116**, 361-368.

Fjioka, H. and Tanishita, K., 2001. Numerical Analysis of Blood Flow in the Non-Planar Aortic Arch Model. *ASME Bioengineering Conference*, **BED-Vol. 50.**

Fujioka, H. and Tanishita, K., 2001. Numerical analysis of blood flow in the non-planar aortic arch model, *ASME Bioengineering Conference*, **BED-Vol. 50**.

Fukushima, T., Matsusawa, T. and Homma, T., 1989. Visualisations and Finite Element Analysis of Pulsatile flow in Models of the Abdominal Aortic Aneurysm, *Biorheology*, **26**, 109-130.

Goodson, R. A. H., 2001. Analysis of Growth and Rupture of Fusiform Abdominal Aneurysms, Ph.D. Thesis. Department of Mechanical and Manufacturing Engineering, The Nottingham Trent University.

Government White Paper, Feb 1998. *Saving Lives: Our Healthier Nation*, **Cm 4386.**

Gow, B. S. and Hadfield, C. D, 1979. The Elasticity of Canine and Human Coronary Arteries with Reference to Postmortem Changes, *Circulation Research*, **45**(5), 588-594.

Grigioni, M., Daniele, C., D'Avenio, G. and Pontrelli, G., 2002. The Role of Wall Shear Stress in Unsteady Vascular Dynamics. *Progress in Biomedical Research*, **7** (3), 204-211.

Grimshaw, G. M., 1994. *The Natural History of the Abdominal Aortic Diagnosed by Mass Screening*. PhD Thesis, The University of Birmingham.

Hayashi, K, 1993. Experimental Approached on Measuring the Mechanical Properties and Constitutive Laws of Arterial Walls, *ASME Journal of Biomechanical Engineering*, **115**, 481-488.

Hayashi, K., Yanai, Y. and Naiki, T., 1996. A 3D-LDV Study of the Relation Between Wall Shear Stress and Intimal Thickness in a Human Aortic Bifurcation, *ASME Journal of Biomechanical Engineering*, **118**, 273-279.

Hoskins, P. R., 1997. Blood flow visualisation, velocity and volume flow measurements using ultrasound, *Presentation made at the Institute of Mechanical Engineering, Fluid Mechanics in Medicine* Seminar, **S572**: 12th December 1997.

How, T. V., Carpenter, T. K., Rowe, C. S. and Harris, R. L., 1997. Local Haemodynamics of Arterial Bypass Grafts," *Presentation made at the Institute of Mechanical Engineering, Fluid Mechanics in Medicine* Seminar, **S572,** 12th December 1997.

Ishikawa, Guimaraes, Oshima and Yamane, 1998. Effect of non-Newtonian property of blood on flow through a stenosed tube, *Fluid Dynamics Research,* **22,** 251-264.

Kamiya, A. and Togawa, T., 1980. Adaptive regulation of wall shear stress to flow change in the canine artery. *American Journal of Physiology*. **239:** H14-H21

Khraushi, T. A., Elger, D. F., Budwig. R. S. and Johansen, K. H., 1997. The effect of branch arteries and Reynolds number on the wall stresses of abdominal aortic aneurysm (AAA) models, *1997 ASME Fluids Engineering Division Summer Meeting, June 22-26.* **FEDSM97-3432.**

Kilner, P. J., Young, G. Z., Mohaiddin, R. H., Firmin, D. N. and Longmore, D. B., 1993. Helical and retrograde secondary flow patterns in the aortic arch studied by three-dimensional magnetic resonance velocity mapping, *Circulation*, **88**, 5(1). 2235-2247.

Kim, Young H., Walker, P. G., Fontaine, A. A., Panchal, S., Ensley, S., Oshinski, J., Sharma, S., Ha, S., Lucas, C. L. and Yoganathan, A. P., 1995. Haemodynamics of the Fontan Connection: An In-Vitro Study, *ASME Journal of Biomechanical Engineering*, **117**, 423-428.

Kurada, S., Rankin, G. W. and Sridhar, K., 1994. Flow Visualisation Using Photochromic Dyes: A Review, *Optics and Lasers in Engineering*, **20**, 177-192.

Kurada. S., Rankin, G. W. and Sridhar. K., 1997. A New Particle Image Velocimetry Technique for Three-dimensional Flows, *Optics and Lasers in Engineering*, **28**, 343-376.

Lãnne, T., Sandgren, T. and Sonesson, B., 1998. A Dynamic View on the Diameter of Abdominal Aortic Aneurysm. *European Journal of Vascular Endovascular Surgery*, **15**(4). 308-312.

Lee, C. S. and Tarbell, J. M., 1997. Wall Shear Rate Distribution in an Abdominal Aortic Bifurcation Model; Effects of Vessel Compliance and Phase Angle Between Pressure And Flow waveforms, *ASME Journal of Biomechanical Engineering*, **119**, 333-342.

Liepsch, D. W., 1986. Flow in Tubes and Arteries - A Comparison, *Biorheology*, **23**, 395-433.

MacSweeney, S. T. R., Powell, J. T. and Greenhalgh, R. M., 1994. Pathogenesis of Abdominal Aortic Aneurysm, *British Journal of Surgery*, **81**(7), 935-941.

Matsumoto, T., Naiki, T. and Hayashi, K., 1994. Flow Visualisation Analysis of Pulsatile Flow in Elastic Straight Tubes, *Biorheology*, **31**(4), 365-381.

Moore, J. E. Jr. and Ku, D. U., 1994. Pulsatile Velocity Measurements in a Model of the Human Abdominal Aorta Under Simulated Exercise and Postprandial Conditions, *Journal of Biomedical Engineering*, **116**, 107-111.

Naiki, T., Kawaguchi, M. and Karino, T., 1997. Development of a Valveless Pulsatile Flow Blood Pump, *Transactions of the Japanese Society of Mechanical Engineers*, **C 63**, 680-685 (in Japanese).

Naiki, T., Takemura, S. and Hayashi, K., 1994. Effect of Wall Elasticity on Pulsatile Flow in Aortic Bifurcation (Flow Visualization Study in Bifurcation Models), *Transactions of the Japanese Society of Mechanical Engineers*, **60**, 3623-3629. (in Japanese)

Naiki, T., Yanai, Y. and Hayashi, K., 1995. Evaluation of High Polymer Solution as Blood Analogue Fluid, *Journal of Japanese Society of Biorheology*, **9**, 84-89, (in Japanese).

Naruse, T and Tanishita, K., 1996. Large Curvature Effect on Pulsatile Entrance Flow in a Curved Tube: Model Experiment Simulating Blood Flow in an Aortic Arch, *ASME Journal of Biomechanical Engineering*, **118**, 180-186.

Nerem, R. M., 1992. Vascular Fluid Mechanics, the Arterial Wall, and Atherosclerosis, *ASME Journal of Biomechanical Engineering*, **114**, 274-282.

Obied, A. N., Barnett, N. J., Dougherty, G. and Ward, G., 1990. A Critical Review of Laser Doppler Flowmetry, *Journal of Medical Engineering & Technology*, **14**(5), 178-181.

Perktold, K., 1987, On the Paths of Fluid Particles in an Axisymettrical Aneurysms, *Journal of Biomechanics*, **20**(3), 311-317.

Perktold, K., Gruber, K., Kenner, T. and Florian, H., 1984. Calculation of pulsatile flow and particle paths in an aneurysm model, *Basic Research in Cardiolology*, **79**, 253-261.

Perktold, K., Peter, R. and Resch, M., 1989. Pulsatile Non-Newtonian Blood Flow Simulation Through a Bifurcation with an Aneurysm, *Biorheology*, **26**, 1011-1030.

Phelps, J.E., and DePaola, N., 2000. Spatial Variation in Endothelial Barrier Function in Disturbed Flows In Vitro. *American Jounal of Physiology: Heart and Circulatory Physiology*, **278,** H469-H476.

Rowe, C. S., 1999. Improving the Local Haemodynamics of Bypass Graft Anastomoses, Ph.D. Thesis. Department of Clinical Engineering, The University of Liverpool.

Sabbah, H. N. and Stein, P. D., 1982. Effect of Aortic Stenosis on Coronary Flow Dynamics: Studies in an In-Vitro Pulse Duplicating System, *Journal of Biomechanical Engineering*, **104**, 221-225.

Shahcheraghi, N., Dwyer, H. A., Cheer, A. Y., Baraket, A, I. and Rutaganira, T., 2001. Unsteady and three-dimensional simulation of blood flow in the human aortic arch. *ASME Bioengineering Conference*, **BED-Vol. 50.**

Shi, Z. D., Winoto, S. H. and Lee, T. S., 1997. Experimental Investigation of Pulsatile Flows in Tubes, *ASME Journal of Biomechanical Engineering*, **119**, 213-216.

Siebes, M., Campbell, C. S. and D'Argenio, D. Z., 1996. Fluid Dynamics of a Partially Collapsible Stenosis in a Flow Model of the Coronary Circulation, *ASME Journal of Biomechanical Engineering*, **118**, 489-497.

Smedby, Ö., Fuchs, L. and Tillmark, N., 1991. Separated Flow Demonstrated by Digitised Cineangiography Compared With LDV, *ASME Journal of Biomechanical Engineering*, **113**, 336-341.

Steiger, H. J., Poll, A., Liepsch, D. and Reulen, H. J., 1987. Basic Flow Structure in Saccular Aneurysms: A Flow Visualisation Study, *Heart and Vessels*, **3**, 55-65.

Sung, H. W., Hsu, T. L., Hsu, C. H. and Hsu, J. C., 1998. Pulmonary artery haemodynamics with varying degrees of vavular stenosis: an in vitro study, *Journal of Biomechanics*, **31**(12), 1153-1161.

Taylor, T. W. and Yamaguchi, 1994. Three-Dimensional Simulation of Blood Flow in an Abdominal Aortic Aneurysm- Steady and Unsteady Flow Cases, *Journal of Biomechanical Engineering*, **116**, 89-97.

Tu, C. and Deville, M., 1996. Pulsatile Flow of Non-Newtonian Fluids Through Arterial Stenoses, *Journal of Biomechanics*, **29**, 889-908.

van Dreumel, S. C. and Kuiken, G. D. C., 1989. Steady Flow Through a Double Converging-Diverging Tube Model for Mild Coronary Stenoses, *ASME Journal of Bioengineering*, **111**, 212-221.

von Segesser, L., Jeanjacquot, A., Meyer. P. and Buchs, J. B., 1984. Arthropump with Peristaltic Effect and Pulsatile Flow, *Journal of Biomechanical Engineering*, **6**, 146-150.

Wille, S., 1981. Pulsatile Pressure and flow in an arterial aneurysm simulated in a mathematical model, *Journal of Biomedical Engineering*, **3**, 152-158.

Yearwood, T. L., 1989. Experimental Fluid Dynamics of Aortic Stenosis in a Model of the Human Aorta, *Clinical Physics Physiological Measurements*, **10**(1), 11-24.

Yeleswarapu, K. K., Kameneva, M. V., Rajagopal, K. R., and Antaki, J. F., 1998. The Flow of Blood In Tubes: Theory and Experiment, *Mechanics Research Communications*, **25**(3), 257-262.

Yu, S. C. M., 2000. Steady and pulsatile flow studies of Abdominal Aortic Aneurysm models using Particle Image Velocimetry. *International Journal of Heat and Fluid Flow*, **21**, 74-83.

Zabielsky, L. and Mestel, J., 1998. Steady flow in a helically symmetric pipe. *Journal of Fluid Mechanics*. **370**: 297-320

Zabielsky, L. and Mestel, J., 1998. Unsteady blood flow in a helically symmetric pipe. *Journal of Fluid Mechanics*. **370**: 321-345

Bibliography

Labs, K. H., Jäger, K. A., Fitzgerald, D. E. Woodcock J. P. Neuerburg-Heusler D. (editors) (1992). *Diagnostic Vascular Ultrasound*, Edward Arnold.

Nichols, W. W. and O'Rourke, M. F., (editors)(1991). *McDonald's Blood Flow in Arteries: Theoretic, Experimental and Clinical Principles*, (Third Edition), Edward Arnold.

Caro, C. G., Pedley, T. J., Schroter, R. C. and Seed, W. A. (1978). *The Mechanics of Ciculation*, Oxford University Press.

Dawson, T.; H., (1991). *Engineering Design of the Cardiovascular System*. Biophysics and Bioengineering Series. Prentice-Hall.

Articles

Knight, J. (1999). Cunning Plumbing. Article published in *New Scientist*, 6 February 1999

Correspondence

Technical specifications for design of the aortic arch kindly provided by the Dr. R. Hose, *Department of Medical Physics and Clinical Engineering, University of Sheffield* (private communication, 2002).

Companies

Sylgard 184 supplied by:

RW Greef.

(R.W Silicones & Lubricants Greef)
Timmis Road
Lye
Stourbridge
West Midlands,
DY9 7BJ
ENGLAND

Tel: +44 (0) 1384 897969
Fax: +44 (0) 1384 897960

http://www.rwgreeff.co.uk

MCP 58 casting product supplied by:

Mining &Chemical Products Ltd

1-4 Nielson Road
Finedon Road Industrial Estate
Wellingborough
Northamptonshire
NN8 4PE
ENGLAND

Tel: +44 (0) 1933 225766
Fax: +44 (0) 1933 227814

http://www.mcp-group.com/alloys/

'Minical' air release valve supplied by:

RS Components Ltd

Birchington Road
Corby, Northants
NN17 9RS
ENGLAND
Tel: +44 (0) 1536 444222

http://www.rswww.com

Stock number 313-7032

ThermoJet 3D Printer:

3D Systems

26081 Avenue Hall
Valencia, CA 91355

U.S. Toll Free Number:
(888) 337-9786
U.S. 3D Corporate Phone Number:
(661) 295-5600
U.S. FAX Number:
(661) 294-8406

http://www.3dsystems.com/

APPENDIX B - 'ANGLE BIN' DATA PARSING

PERL scripting written in house by Mr. Mike Haber: Technician, Department Mechanical and Manufacturing Engineering, The Nottingham Trent University.

Data output from each BSA was exported into a folder with sequential file headings representing data collected at each grid point. The files were subsequently parsed for relevant angle bin data and the output from each data file appended to a single data array. Two variants on this programme were utilised. One for each of the data sets obtained from each BSA. Output files were labelled as originating from BSA1 or BSA2 where appropriate.

ActivePerl-5.6.1.631-MSWin32-x86 was installed on the windows platform in order for the script to be successfully executed.

```
#!/usr/bin/perl -w

#Program for Matt Dalton to read in data from test files, parse some output
and then write the relevant output to another file
#by Mike Haber Nov2002.
#The main program is very short.It loops for every input file. It calls
readXYZ() to read the x,y and z values off the first
#line of the input file. it then calls writeData() which using the
@angleBinReads array to read only the lines of data we want
#and then extracts the Vel-mean and Vel-rms columns, using the @lineValues
array.


open(WRITEFILE,">output.txt")||die "Sorry could not open file for writing";
        #change output file here
open(LOGFILE,">log.txt")||die "Sorry could not open file for writing";
@angleBinReads=("18.00","54.00","108.00","198.00","288.00","342.00");
        #contains the angles we want to read from input
writeHeader(@angleBinReads);
#loop through the files until you run out
$f="001";                                                    #as a string this
increments correctly
print LOGFILE 'date /T';                                     #'date' in *nix,
'date \T' in windows.
while(open(READFILE,"pulsatile default2##$f.txt")){          #||die "Sorry
could not open file";
        print LOGFILE "reading file $f\n";
        @xyzValues=readXYZ();                                #calls function
that reads the x,y,and z values
        writeData(@angleBinReads);
        close(READFILE);
        $f++;
}
close(WRITEFILE);
close(LOGFILE);
```

```
#function to write the ~~relavent~~ data to the output according to the
@angleBinReads
#Assumes the relavent data is the Vel-Mean and Vel-RMS columns. Angle Bin is
column [1], Vel-Mean is col[2],
#and Vel-rms is col[3].
sub writeData{
	#we only want to write the Vel data for the angleBins we specified so
loop thought the angleBinReads array
	#and write the relavent columns to the output.
	$i=0;							#for @ngleBinReads[]
	$firstline=<READFILE>;						##we dont need
this, it contains the headers
	print "read first line.\n";
	print	WRITEFILE	"$xyzValues[0]\t$xyzValues[1]\t$xyzValues[2]\t";
	#write x,y,z positions once per file
	while($angleBinReads[$i]){
		print"Were matching on $angleBinReads[$i] \n";
		for($j=0;$j<20;$j++){					#read 20 lines
only
			$_=<READFILE>;
			@lineValues=split(/\s+/,$_);			#splits line on
whilespace, in this case, tabs
			print "lineValues[1] is $lineValues[1]\n";
			if($angleBinReads[$i] eq $lineValues[1]){
				print "$angleBinReads[$i] equals $lineValues[1]
in file $f\n";
				print							WRITEFILE
"$lineValues[2]\t$lineValues[3]\t";
				print "writing $lineValues[2]\t$lineValues[3]\t
for file $f $angleBinReads[$i]\n";
				$i++;
				last;
			}
		}

	}
	print WRITEFILE "\n";						#once per input
file
}


#function to write the header for the output file to denote columns for
x,y,z and anglebins
sub writeHeader{
	print WRITEFILE "XPos\tYPos\tZPos\t";
	#we don't know how many anglebins we have so loop and write intil
we're done
	$i=0;
	while($angleBinReads[$i]){
		print								WRITEFILE
substr($angleBinReads[$i],0,3)."V\t".substr($angleBinReads[$i],0,3)."RMS\t";
		$i++;
	}
	print WRITEFILE "\n";
}

#function to read the x,y and z values from the first line of each of the
input files and return them in an array
sub readXYZ{
	$firstLine=<READFILE>;
	$xFromIndex=index($firstLine,"POSX=")+5;
	$yFromIndex=index($firstLine,"POSY=")+5;
	$zFromIndex=index($firstLine,"POSZ=")+5;

	$xToIndex=index($firstLine,"mm");
	$yToIndex=index($firstLine,"mm",$xToIndex+2);
	$zToIndex=index($firstLine,"mm",$yToIndex+2);
	print "xto $xToIndex yto $yToIndex zto $zToIndex";

	#output the results to test
	$xyzValues[0]=substr($firstLine,$xFromIndex,$xToIndex-$xFromIndex);
	$xyzValues[1]=substr($firstLine,$yFromIndex,$yToIndex-$yFromIndex);
	$xyzValues[2]=substr($firstLine,$zFromIndex,$zToIndex-$zFromIndex);
	return @xyzValues;
}
```

APPENDIX C – CASTING OF THE ANEURYSMAL MODEL

CASTING PROCEDURE

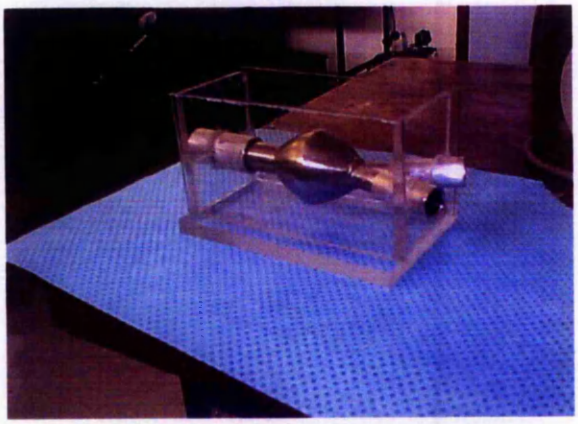

The metal core was placed inside a Perspex box of plain face

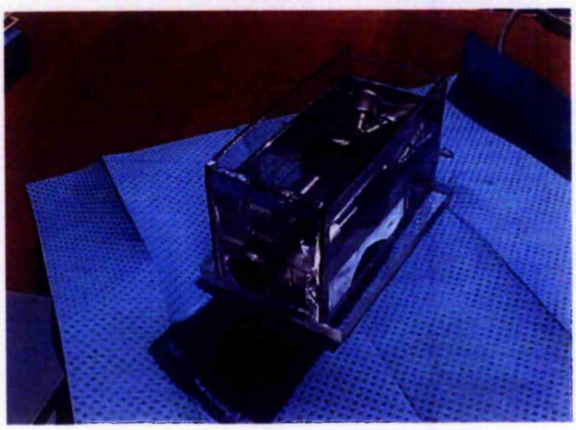

Silicone elastomer was mixed and de-aerated before being poured into the box to be cured at 25°C for 12 hours

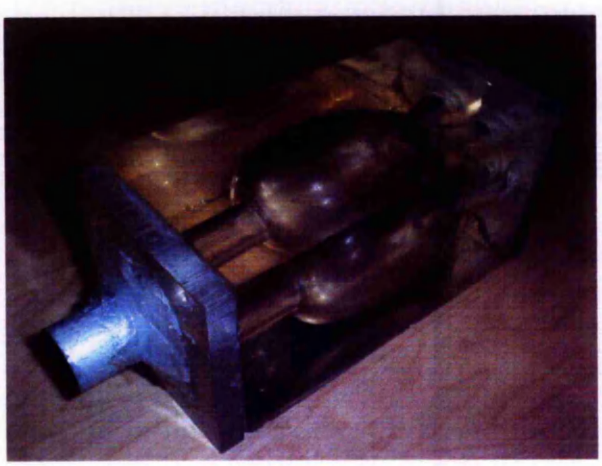

After removal from the casting box the metal pipefittings were reattached with silicone sealant. End brackets were added to increase the robust nature of the model and to provide a non-compressible edge against which the model could be located in the rig

APPENDIX D – MODEL SPECIFICATION

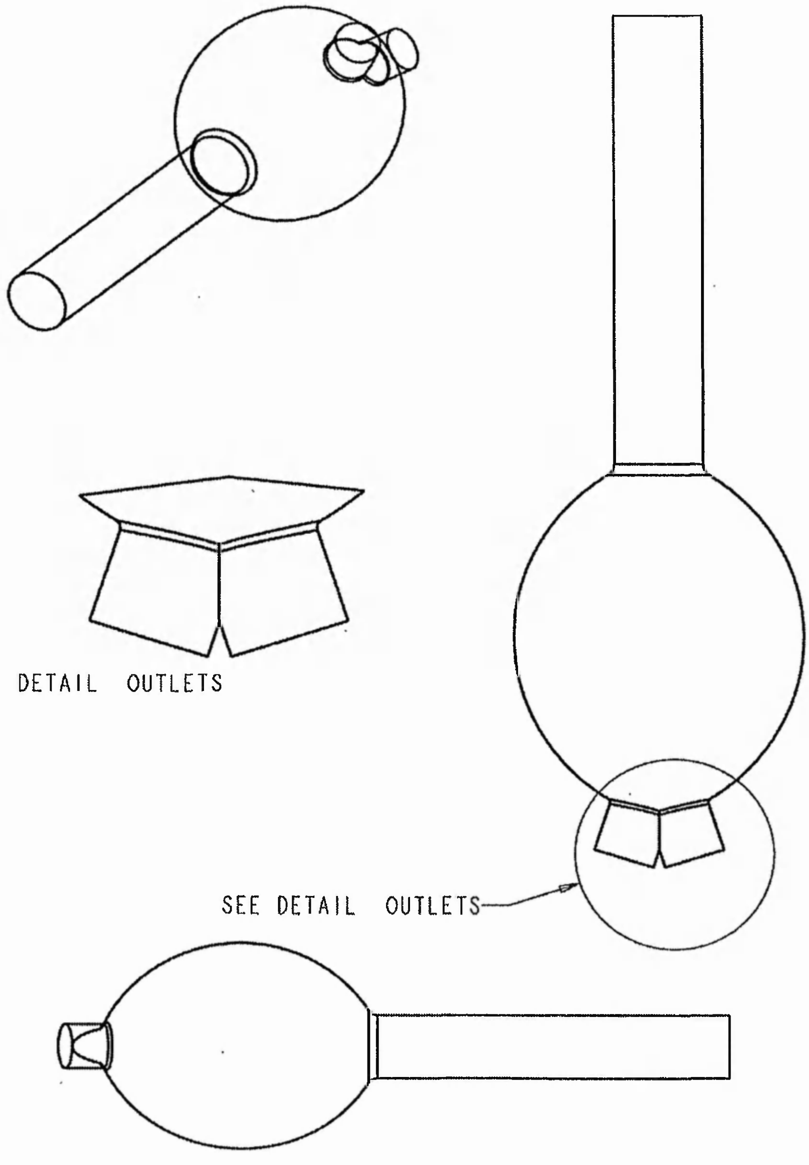

Diagrammatic views of the internal dimensions of the aneurysm model

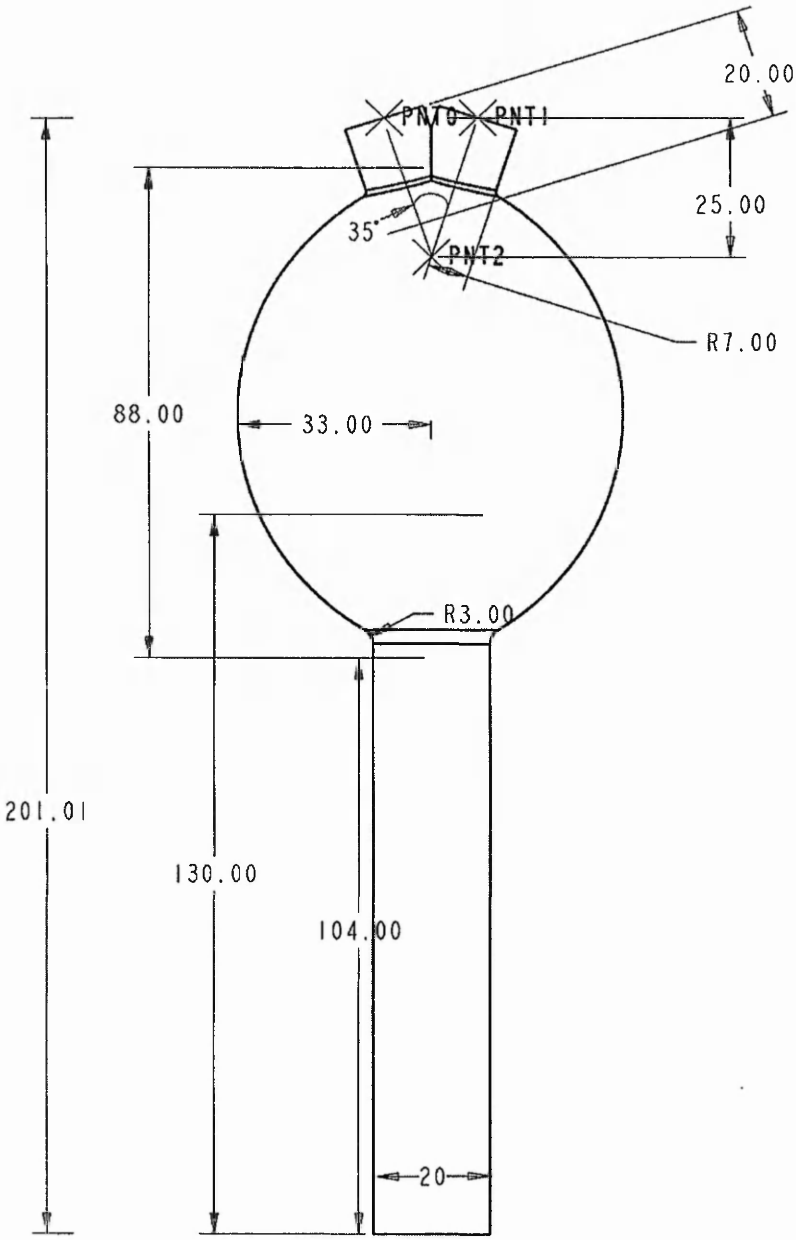

Dimensions attributed to the aneurysm model.

It is worth noting that the exact model used was hand made and as such did not conform to these exact specifications. However, this it the best parametric representation of the model

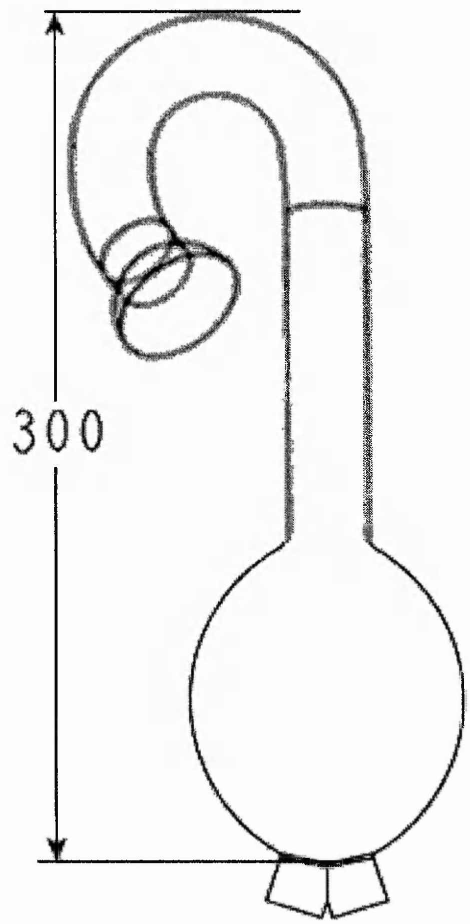

The full length of the model from apex of the aortic arch to the aortic bifurcation was designed to be 300mm, to simulate the average male physiology on a scale of 1:1